Reactive transport and long-term redox evolution at the catchment scale.

Dissertation

der Mathematisch-Naturwissenschaftlichen Fakultät

der Eberhard Karls Universität Tübingen

zur Erlangung des Grades eines

Doktors der Naturwissenschaften

(Dr. rer. nat.)

vorgelegt von

Evgenii Kortunov

aus Krasnoarmejsk, Russland

Tübingen

2018

Gedruckt mit Genehmigung der Mathematisch-Naturwissenschaftlichen Fakultät der Eberhard Karls Universität Tübingen.

Tag der mündlichen Qualifikation:	11.07.2018
Dekan:	Prof. Dr. Wolfgang Rosenstiel
1. Berichterstatter:	Prof. Dr. Peter Grathwohl
2. Berichterstatter:	Dr. Chuanhe Lu

Abstract

Diffusive groundwater pollution caused by agricultural and atmospheric inputs is a pressing issue in environmental management worldwide. Various researchers have studied nitrate contamination since the substantial increase of nitrogen fertilization in agriculture starting in the second half of the 20th century. This study addresses large scale reactive solute transport in typical landscapes and aquifers exemplified by geological analogues of southwestern Germany.

Firstly, fate of nitrate and other solutes was studied in a typical hilly landscape in a transect crossing two river valleys (Ammer and Neckar rivers) in Southern Germany. The numerical model compromises a 2-D cross-section accounting for geology, water-rock interaction, intra-aqueous reactions, and groundwater hydraulics. Results show that the groundwater divide significantly deviates from the surface water divide promoting inter-valley groundwater flow. Reactive transport modelling of redox-sensitive solutes (e.g. agricultural nitrate, natural sulfate and dissolved organic carbon) with MIN3P indicates that in the floodplains of both rivers, organic rich Holocene sediments allow reduction of agricultural nitrate. However, nitrate applied in the hillslopes of Ammer valley underlain by a fractured oxidized Triassic mudrock is transported towards the high yield sand and gravel aquifer in the neighboring Neckar valley. Therefore, nitrate in the Neckar valley groundwater may come to a large extent from the hillslopes of the neighboring valley and not from the agriculture sources in the valley itself. The study demonstrates cross catchment transport of groundwater pollutants, which occurs if water levels between adjacent valleys differ significantly. The more detailed reactive transport model of Ammer river floodplain shows that agriculture nitrate is reduced rapidly in the Ammer floodplain sediments. However, there is a potential for geogenic production of ammonium in sediment layers high in organic carbon and peat, which might be a major source of nitrate in the drains. Part of the nitrate in drains and creeks in the Ammer valley thus could be of geogenic origin. Such findings are relevant for regional land and water quality management.

Secondly, a reactive transport model was developed for a fractured pyrite bearing limestone aquifer. The flow was assumed to pass through a connected system of fractures and karstified features providing the continuous exposure of water parcels to the limestone surface with subsequent reactive diffusive transport of solutes in the rock matrix. A series of scenarios was developed to understand the pathways of pollutant turnover (especially nitrate) if the activity of biota is suppressed in the limestone matrix due to small pore sizes. A sequence of

abiotic and biotic steps has to be considered in pyrite oxidation in the matrix to provide a realistic source of Fe^{2+}. Results showed that pyrite in the matrix alone cannot significantly affect the nitrate transport. Only the simultaneous presence of siderite in the limestone (and/or pyrite exposed directly on the fracture wall) may explain observed patterns of denitrification.

Overall, this dissertation demonstrates the importance of individual and comprehensive investigation of complex hydrogeological systems such as adjacent valleys during the process of decision making in land use management. This dissertation also demonstrates the relevance of reactive transport modelling to identify potential reaction pathways of groundwater pollutants in large scale flow in fractured aquifers. This is a prerequisite to understand and predict long-term fate and transport of pollutants in groundwater.

Zusammenfassung

Die diffuse Grundwasserverschmutzung durch landwirtschaftliche und atmosphärische Einträge ist weltweit ein drängendes Thema im Umweltmanagement. Verschiedene Forscher haben die Nitratbelastung seit der erheblichen Zunahme der Stickstoffdüngung in der Landwirtschaft ab der zweiten Hälfte des 20. Jahrhunderts untersucht. Diese Studie befasst sich mit dem großräumigen reaktiven Stofftransport in häufig anzutreffenden Landschaften und Aquifern am Beispiel von realen Analoga im Südwesten Deutschlands.

Zunächst wurden Nitrat und andere gelöste Stoffe in einer typischen Hügellandschaft in einem Transekt über zwei Fluss-Täler (Ammer und Neckar) in Süddeutschland untersucht. Das numerische Modell umfasst einen 2-D-Querschnitt, der die Geologie, die Wasser-Gestein-Wechselwirkung, Reaktionen im Grundwasser und die Grundwasserhydraulik berücksichtigt. Die Ergebnisse zeigen, dass die Grundwasserscheide signifikant von der Oberflächenwasserscheide abweicht und damit Grundwasser ins benachbarte Tal exportiert werden kann. Die reaktive Transportmodellierung von redox-sensiblen gelösten Stoffen (z.B. Nitrat aus der Landwirtschaft, geogenes Sulfat und DOC) mit MIN3P zeigt, dass in den Auen beider Flüsse kohlenstoffreiche holozäne Sedimente die Reduktion von Nitrat ermöglichen. Nitrat, das an den Hängen des Ammertals aufgebracht wird, die von geklüfteten, oxidierten Trias-Tonsteinen unterlagert werden, wird nicht reduziert und in Richtung des ergiebigen Sand- und Kies-Aquifers im benachbarten Neckartal transportiert. Daher könnte ein beträchtlicher Teil des Nitrats im Grundwasser des Neckartals aus dem benachbarten Ammertal stammen. Die Studie demonstriert damit, dass Grundwasserschadstoffe von einem Tal ins benachbarte exportiert werden können, wenn sich die Wasserstände zwischen benachbarten Tälern unterscheiden. Das detailliertere reaktive Transportmodell der Ammeraue zeigt, dass das landwirtschaftliche Nitrat in den Sedimenten der Ammeraue zwar rasch reduziert wird, aber geogenes Ammonium aus kohlenstoffreichen Schichten und aus Torf in den Drainagen und Bächen oxidieret wird und eine Quelle für Nitrat darstellen könnte. Diese Erkenntnisse sind für das regionale Land- und Wasserqualitätsmanagement relevant.

Weiterhin wurde ein großskaliges reaktives Transportmodell für einen pyrithaltigen und geklüfteten Kalkstein-Aquifer entwickelt. Die Grundwasserströmung erfolgt in einem Kluftnetzwerk und Verkarstungen und gelöste Stoffe unterliegen einem reaktiven-diffusiven Transport in der Kalksteinmatrix. Eine Serie von Szenarien wurde getestet, um den Schadstoffumsatz (insbesondere von Nitrat) nachzubilden, insbesondere wenn eine mikrobielle Aktivität in der Kalksteinmatrix aufgrund zu kleiner Poren unterbleibt. Eine Folge

von abiotischen und biotischen Schritten muss bei der Pyritoxidation in der Matrix berücksichtigt werden, um genügen Fe^{2+} für die Nitratreduktion freizusetzen. Die Ergebnisse zeigen jedoch, dass reicht dies nicht ausreicht, um den Nitrattransport signifikant zu beeinflussen. Erst die Annahme, dass parallel zum Pyrit auch Siderit in der Kalksteinmatrix vorkommt, erlaubt es die beobachteten Muster der Denitrifikation zu erklären. Alternativ könnte auf Kluftflächen vorkommender Pyrit im anaeroben Bereich des Aquifers zur Denitrifizierung beitragen.

Insgesamt zeigt diese Dissertation die Bedeutung einer individuellen und umfassenden Untersuchung komplexer hydrogeologischer Systeme wie z.B. benachbarter Flusstäler für Entscheidungsprozesse im der Landnutzung. Weiterhin wird aufgezeigt, dass eine reaktive Transportmodellierung zur Aufklärung der Reaktionswege von Grundwasserschadstoffen in großskaligen Kluftaquifern notwendig ist. Die ist Voraussetzung zum Verständnis und zur Vorhersage des Langzeitverhaltens von Schadstoffen im Grundwasser.

Acknowledgements

I would like to thank several individuals, who, in some ways helped me to complete this PhD dissertation. First of all I would like to thank Prof. Dr. Peter Grathwohl, for providing me the opportunity to work on this dissertation within the (International) Research Training group. He shared a lot of interesting ideas and observations, helped me by directing of my research and provided continuous me with support until the end.

I also want to express my appreciation to Dr. Chuanhe Lu, who helped me a great deal with writing every part of this dissertation. I want to thank Dr. Uli Maier, who introduced me to the code MIN3P which I used for reactive transport modelling. For hosting me during my research stay at Carleton University in 2016 as well as for his scientific guidance, I would like to thank Prof. Dr. Richard T. Amos. Furthermore, I express my gratitude to Prof. Dr. Uli Mayer, who helped me with MIN3P during his visit to Tuebingen. I appreciate Prof. Dr. Olaf A. Cirpka, who is the heart of the (I)RTG program and who organized incredible seminars and workshops for our education. He also never declined to discuss my modelling results and provide me with some research ideas. I would like to thank Prof. Dr. Andreas Kappler, who also shared his ideas with me, and helped me to understand some aspects of redox systems behavior. Dr. Herman Rugner, Dr. Karsten Osenbrück, Dr Marc Schwientek, Dr. Fernando Mazo D'Affonseca and Natalia Jakus helped me in various ways during my research. I am indebted to administration (Monika Jekelius and Dr. Wolfgank Bott) of Center for Applied geoscience and Welcome Center of University of Tubingen (Kirsten Sonnenschein) for helping me to survive all the bureaucracies and deal with numerous visa issues. I would also like to appreciate my former supervisor Prof. Dr. Alexey Lekhov (who made me the hydrogeologist I am today), Prof. Dr. Sergey Pozdniakov (who helped me to find this job) and Prof. Dr. Sergey Grinevsky (who encouraged me a lot) from Moscow State University. A learned much from all of them and not only during classes.

I want to thank all my friends and colleagues from my research training and Hydrogeochemistry groups, as well as officemates in K17: Zhongwen, Munir, Karim, Diane, Bijendra, Chang, Matthias (and Denise), Reynold (and Junko), Marvin, Emilio, Bo and others. I also want to thank all my friends, spread now all around the world for sharing many happy and not so happy moments. In particular special thanks to Vova, Dasha, Igor, Ivan, Ksenia, Mitia, again Mitia, Tania, Seryoga, Grisha, Vera, members of our downhill skiing crew and a lot of other people I had fun with during last four years. Petr Buravtsev deserves special appreciations for showing all of us that literally nothing is impossible.

Last but not least, I want to thank my entire family, my mother, my father, my grandparents, my sister, her husband and their beautiful children: Kristina, Uliana and Savva, who all were and are the neverending source of positive emotions. Who might have thought that children can be *so* enjoyable? My family always encouraged me, which indeed helped me to finish this dissertation.

This PhD dissertation was funded by the German Research Foundation (DFG) through (I)RTG project which I hereby also acknowledge.

Content

List of Figures

List of Tables

1. INTRODUCTION

1.1. STATE OF THE ART AND MOTIVATION

1.1.1 REACTION TRANSPORT AND TRANSPORT ON CATCHMENT SCALE

In recent years, multicomponent reactive transport models have become an essential instrument in studying and investigating groundwater geochemistry in various aspects. Understanding of the fate of pollutants and the chemical evolution of natural systems which both involve complex processes can be increased using this instrument [*Zhang et al.*, 2012]. The definition of a multicomponent reactive transport model might be quite broad, and the number of considered processes can vary from model to model and depends on the particular application. The conventional approach to simulate reactive transport is to solve numerically several governing partial-differential equations, which account for conservation of momentum, conservation of energy, conservation of solute, solid and fluid mass and constitutive laws [*Steefel et al.*, 2005].

During the last three decades, several ready-to-use reactive transport simulation toolboxes have been developed in this field, for example, PHT3D [*Prommer et al.*, 2003], MIN3P [*Mayer*, 2002] or CrunchFlow [*Steefel and Lasaga*, 1994]. The overview of various reactive transport packages and their capabilities can be found in *Zhang et al.* (2012) or *Steefel et al.* (2015); information on mathematical and numerical formulations used in such codes are also provided. Numerical reactive transport modeling is used for various applications across the different scales. For instance on the pore scale [*Chen et al.*, n.d.; *Rolle et al.*, 2013], laboratory scale [*Amos et al.*, 2004; *Muniruzzaman and Rolle*, 2016], field scale simulations of contaminate plumes [*Prommer et al.*, 2002; *Maier et al.*, 2007; *Cirpka et al.*, 2012], acid mine drainage [*Jurjovec et al.*, 2004; *Molson et al.*, 2012], CO_2 and nuclear waste storage simulations [*Shestakov et al.*, 2002; *Druhan et al.*, 2014; *Bakshevskaia and Pozdniakov*, 2016] or long term geochemical weathering processes [*Maier et al.*, 2013; *Bao et al.*, 2017; *Heidari et al.*, 2017].

For catchment scale simulations, spatially explicit reactive transport models are usually considered time and parameter demanding, therefore more simplified approaches like travel time based [*Howden et al.*, 2011; *Loschko et al.*, 2016], reactive zones based [*Hansen et al.*, 2014] or storage based [*Arnold et al.*, 1998] models are used. Nevertheless, if uncertainty assessment is not the aim of the model and physical hypotheses have to be tested, applying spatially explicit reactive transport models on catchment scale are possible with preliminary conceptual model simplifications [*Zhang et al.*, 2013; *Jang et al.*, 2017].

1.1.2. MODELLING OF REDOX REACTIONS

Electron transfer from one atom to another results in redox reactions (reduction or oxidation). Such reactions employ an essential control on both natural concentrations of redox-sensitive species, for example, O_2, Fe^{2+}, SO_4^{2-}, H_2S, NH_4^+, etc., and the fate of anthropogenic pollutants such as nitrate or heavy metals. Electron transfer between two solutes is typically very slow and usually (but not always) catalyzed by bacteria which accelerates reaction rates [*Appelo and Postma*, 2005]. The order in which oxidation and reduction half-reactions proceed can be predicted from equilibrium thermodynamics. The sequence of important reduction half-reactions starts by O_2 reduction, followed by denitrification, Mn(4) oxide reduction, Fe(3) reduction, sulfate reduction and finally CH_4 fermentation. For oxidation half-reactions, the sequence starts with oxidation of organic material, oxidation of sulfide into sulfate, Fe(2) oxidation and finally nitrification [*Stumm and Morgan*, 1996]. The common classification of redox zonation includes oxic and anoxic zones, with later divided into post-oxic, sulfidic and methanogenic subzones [*Robert A. Berner*, 1981].

These half-reactions comprise homogeneous intra-aqueous or heterogeneous full reactions. For instance, O_2 reduction (Eq. 1.1), denitrification (Eq. 1.2), sulfate reduction by CH_2O (DOC) (Eq. 1.3) or nitrification (Eq. 1.4) happen in aqueous phase. Kinetics for these type of reactions are conventionally described by the Michaelis–Menten model (no consideration of biomass dynamics such as growth and decay) or the Monod model (biomass is dynamic) [*Barry et al.*, 2002; *Brun and Engesgaard*, 2002; *MacQuarrie and Mayer*, 2005]

$$CH_2O + O_2\,(aq) \rightarrow CO_2\,(aq) + H_2O \qquad (1.1)$$

$$CH_2O + 4/5NO_3^- + 4/5H^+ \rightarrow CO_2\,(aq) + 2/5N_2\,(aq) + 2/5H_2O \qquad (1.2)$$

$$CH_2O + 1/2SO_4^{2-} + 1/2H^+ \rightleftarrows CO_2\,(aq) + 1/2HS^- \qquad (1.3)$$

$$NH_4^+ + 2O_2\,(aq) \rightarrow NO_3^- + H_2O + 2H^+ \qquad (1.4)$$

Oxidation of pyrite by oxygen (Eq. 1.5) or by nitrate (Eq. 1.6) are heterogeneous reactions and take place on the boundary between phases. The pyrite oxidation kinetics is usually described by the model proposed by *Williamson and Rimstidt* [1994] or by the shrinking core considering the inhibition of the reaction by precipitation of byproducts which leads to coating [*Wunderly et al.*, 1996; *Mayer*, 2002].

$$FeS_2\,(s) + 3.5O_2(aq) + H_2O \rightleftarrows Fe^{2+} + 2SO_4^{2-} + 2H^+ \quad (1.5)$$

$$5FeS_2\,(s) + 14NO_3^- + 4H^+ \rightleftarrows 7N_2 + 5Fe^{2+} + 10SO_4^{2-} + 2H_2O \quad (1.6)$$

Both homogeneous and heterogeneous reactions do not always happen simultaneous and can produce various byproducts in different reaction steps.

1.1.3. NITROGEN SPECIES TURNOVER AND NITRATE TRANSPORT

Diffuse groundwater pollution caused by agriculture is a pressing issue in environmental management worldwide. Most important is nitrate contamination because of the substantial increase of fertilizer use in agriculture in the second half of the 20th century [*Puckett et al.*, 2011]. Research on nitrate contamination and reactive transport has a long legacy. The related processes and reactions in groundwater are widely studied and described [*Böhlke*, 2002]. The two most important overall reactions in N-cycling are denitrification and nitrification. Denitrification overall compromises a transfer of five electrons per N-atom and the pathway consists of several steps:

$$NO_3^-{}_{(aq)} \rightarrow NO_{2(aq)} \rightarrow NO_{2(\text{enzyme complex})} \rightarrow N_2O_{(gas)} \rightarrow N_{2(gas)}$$

Intermediate species, although not stable, can be found in water and may be used as an evidence of denitrification. The reaction is not reversible. Consequently, N_2 cannot directly be oxidized to NO_3^- without N_2 fixation and nitrification steps .[*Appelo and Postma*, 2005].

In their comprehensive overview, *Rivett et al.* [2008] describe how redox reactions decrease nitrate concentration strongly in aquifers depending on the availability of reactive electron donors such as organic compounds. Dozens of studies investigated the factors controlling the nitrogen cycle using field data and numerical simulations [e.g. *Böhlke et al.*, 2002; *Howden et al.*, 2011; *Welch et al.*, 2011; *Heppell et al.*, 2014; *Refsgaard et al.*, 2014; *Best et al.*, 2015]. Groundwater dating together with dissolved nitrogen measurements allow estimating denitrification rates under different conditions [*Tesoriero and Puckett*, 2011a]. However, the lack of uncertainty analyses in most of these previous studies, the wide range of denitrification rates and geochemical heterogeneity makes it difficult to assess the influence of denitrification on groundwater quality when local geochemical information is absent. Comparison of results on denitrification from different aquifers is challenging since rates depend on many factors, e.g., groundwater recharge, N input at the land surface, soil properties [Liao et al., 2012]. *Dragon* [2012] studied the autotrophic denitrification in the

regional flow system and discussed the importance of vulnerable areas. *Zhang et al.* [2013] simulated catchment scale transient sulfide driven denitrification in a 2-D reactive transport model. Despite the many studies, there is still a lack of mechanistic studies which elucidate the turnover processes of nitrogen species at landscape scale [*Liao et al.*, 2012]. Complexity and heterogeneity of geological settings make it difficult to predict nitrate transport. It is also important to consider the non-reactive areas which serve as a transit zones for nitrate [*Best et al.*, 2015] and increase overall groundwater vulnerability. *Lasagna et al.* [2016] underlined that important physical processes (dilution and mixing) and biological processes (redox reactions) are often neglected in the studies on groundwater vulnerability.

1.1.4 REACTIVE TRANSPORT IN FRACTURED MEDIA

Reactive transport of nitrate or other solutes becomes even more complicated when fractured and karstified media are concerned due to the enormous heterogeneity and complexity of water-rock interactions [*US EPA*, n.d.]. Transport involves preferential water flow in the fractures and solutes diffuse from the fractures into the matrix [*Ortoleva et al.*, 1986]

Since the 1980s many issues were addressed in the field of reactive transport through fractured media and many tools and models were developed [*Neuman*, 2005]. Analytical solutions were first developed to quantify the effect of the matrix diffusion during advective transport of radionuclides in single fractures for potential nuclear waste repositories [*Neretnieks*, 1980; *Tang et al.*, 1981; *Grisak and Pickens*, 1981a]. Later such solutions were expanded to include systems of fractures, [*Sudicky and Frind*, 1982] or radioactive decay chains [*Sudicky and Frind*, 1984]. In more recent years, analytical and semi-analytical models were developed which can include various additional features such as stagnant flow zones and layered systems [*Mahmoudzadeh et al.*, 2013], multiple radioactive decay products [*Shahkarami et al.*, 2015; *Mahmoudzadeh et al.*, 2016] and chemical reactions [*Andersen and Evje*, 2016] including different reaction rates in fracture and in matrix [*Zhu et al.*, 2016] or source decay and sorption [*West et al.*, 2004]. A series of semi-analytical solutions was developed by *Huang and Goltz* [2015] for transport in shales.

Antonellini et al. [2017] fitted oxygen diffusion fronts and alteration halos in low-permeability sandstones matrixes which are frequently accompanied with fractures [*Eichhubl et al.*, 2009] with an analytical solution to describe redox transport in fractured media. However, numerical models provide the possibility to explore a broader range of processes and parameters affecting transport in realistic fractured media accounting for complex redox

reactions including various electron donors and acceptors, non-first order kinetics or variable microbial activity in the rock matrix and fracture. *MacQuarrie et al.* (2010) categorize possible conceptual models in three groups:

- Equivalent porous medium models for the fracture and/or fracture zone
- Discrete fracture network models with reactive infill or coatings and no interaction with the adjacent rock matrix
- Fracture–matrix models in which the fracture and/or matrix may contain reactive minerals

Several numerical studies were conducted in the field of oxygen transport in fractured media. *Sidborn and Neretnieks* (2007, 2008) simulated redox evolution in granites using various conceptual models and fitted some of the results with analytical solutions. They showed that the reduction capacity of the fractures (e.g., reduced mineral coating) is essential in the short term while matrix diffusion of oxygen is a limiting factor in a long term. In contrast, *Spiessl et al.* (2008) used a single fracture-matrix system and showed that kinetics controls oxygen transport in the presence of reducing minerals in the fracture while matrix diffusion was not relevant.

Discrete fracture networks were utilized for transport simulations in crystalline rocks by several recent studies [*Abdelghani et al.*, 2015]. *Molson et al.* (2012) for instance developed a 2-D oxygen transport model, which includes "multi-component advective-dispersive transport, equilibrium geochemical speciation, and water-rock pH-buffering reactions within a discrete fracture network and found that the model outcomes differ from the equivalent porous media models". They emphasize the need to implement kinetic reactions for more realistic geochemical behavior. *Trinchero et al.* (2017) used a deterministic 3-D discrete fracture network model based on extensive field and laboratory studies "for the modeling of flow, transport and geochemical processes in crystalline fractured rocks and to simulate the ingress of oxygen in an initially anoxic fractured media". They showed that this model allows predicting reactive transport more realistically. They also agreed with previous studies on long-term quasi steady state conditions for oxygen transport are attained after five years. However, no matrix diffusion was considered in this study, and even with this simplification, the computational power of a supercomputer had to be applied. Many authors conclude that computational requirements for such modeling approaches are still too high, especially if uncertainty analyses are concerned.

All these modeling studies were conducted for the transport in crystalline rocks, where fractures and thus flow paths can be traced relatively simply. Moreover, most of them

considered dissolved oxygen as the only electron acceptor. While denitrification and sulphate reduction were observed in fractured sedimentary aquifers [*Pauwels et al.*, 2010; *Vidal-Gavilan et al.*, 2013; *Opazo et al.*, 2016], still less is known about the redox evolution and pollutant transport in the limestone aquifers albeit pyrite might be considered as the most important donor mineral [*Opazo et al.*, 2016] and major matrix minerals, e.g., carbonates are relevant as well. Limestone aquifers are different from the crystalline ones in several ways, especially the permeability structure and thus flow paths are complex and usually not understood.

Reactions pathways involved in pollutant attenuation and the relevant geochemical framework are also not well represented. The importance of the abiotic oxidation of Fe^{2+} bearing minerals for redox evolution in fractured systems was elucidated by *Sidborn* (2007). However, abiotic oxidation of such minerals by NO_3^- is considered impossible [*Appelo and Postma*, 2005]. Thus, mechanisms of oxygen reduction and especially abiotic denitrification involving pyrite remain unclear. Other Fe^{2+} bearing minerals also can play a role. Siderite, for example, may act as an electron donor, although its solubility is low. However, oxidation of pyrite results in pH drop, which may increase the solubility of siderite and facilitate the release of Fe^{2+}. The simultaneous presence of pyrite and siderite is considered impossible from the thermodynamic point of view [*Appelo and Postma*, 2005], but nevertheless they occur together in nature [*Ellwood et al.*, 1988; *Haese et al.*, 1997].

1.2. STRUCTURE OF THE DISSERTATION AND SCOPE OF THE STUDY

This doctoral thesis consists of seven chapters, and the following subjects are presented:

In **Chapter 2** modeling approaches, the MIN3P code used for modeling and the geochemical systems are described. The necessary geological information is provided for a typical southwestern (SW) Germany setting which represents the geological framework in which all studied processes occur.

Chapter 3 describes the 2-D flow model developed for a representative SW Germany hilly Triassic landscape. The model is based on the cross-section between Neckar and Ammer valley through Spitzberg hill located near Tuebingen and is used to test the sensibility of the position of the groundwater divide between these two valleys. The groundwater divide position is hypothesized to be shifted relative to the topographical water divide creating the water and solute export from one valley to the other. The possibility to constrain the

groundwater divide position was tested and effective parameters (hydraulic conductivities, groundwater recharge, etc.) were calibrated in order to match with observations (water levels, location of springs).

In **Chapter 4** the model was extended to simulate and investigate the chemical evolution and reactive transport of the contaminants. The focus of the investigation was concentrated on the importance of diffuse agricultural input of nitrate in the Ammer valley on the water quality in the Neckar valley since flow model predicted groundwater flow in this direction. Even though nitrate was the target of this study, other oxidants like O_2 and SO_4^- were also included in the geochemical system since the redox system is interlinked. The most important parameters and features concerning such intervalley transport were interrogated.

In **Chapter 5** redox hydrogeochemistry of the Ammer floodplain was studied to understand nitrogen species turnover in such hotspot. The 2-D fully coupled reactive transport crop-model was developed based on the previous larger model, and the possible geogenic sources of nitrate in the river and drains were investigated.

In **Chapter 6** long-term geochemical evolution and catchment scale nitrate transport is examined in a fractured limestone aquifer based on the Upper Muschelkalk formation. The "one fracture with adjusted matrix" modelling approach was applied, which was not used before for this type of the aquifer and scale. Moreover, the Upper Muschelkalk limestones are prominent for small pore sizes, which supposedly exclude microbial communities and several scenarios were tested to explain natural denitrification in the aquifer.

In **Chapter 7** overall conclusions and a future outlook are given.

ith this following objectives and questions are addressed in this work:

1. Where are possible locations of subsurface water divide between two adjacent valleys (Neckar river and Ammer river) and where does the nitrate in the Neckar valley aquifer originate and what is its possible amount? What Parameters and processes control the fate of nitrate especially when it enters valleys floodplain?
2. What is the source of the nitrate observed in the Ammer valley floodplain drains, considering the fact that the sediments are highly reduced? Can agriculture nitrate be transported through this reduced zone or is it natural ammonium oxidized in the surface water? Are there any other significant reactions except the redox reactions affecting the system?

3. What parameters and processes affect the long-term redox evolution and nitrate transport in the limestone fracture aquifer? Is the system diffusion or kinetics controlled?
4. Is it possible to provide sufficient reduction potential in the fractures when microbial growth in the matrix is suppressed? Is a sequence of abiotic and biotic steps necessary for pyrite oxidation in the matrix and ferric iron oxidation after diffusive transport in the fracture or are other sources of electron donors relevant, e.g. pyrite crystals on the fracture walls or accessory siderite in the rock matrix?

2. METHODS AND MATERIALS

2.1 INTRODUCTION

The numerical code MIN3P was used for all simulations performed in this thesis. The mathematical model consists of sets of governing equations. Richards's equation describes groundwater flow under variably saturated conditions when another set describes multicomponent advective-dispersive transport in the aqueous phase and diffusive transport in the gas phase. The reaction network is described by a partial-equilibrium approach, where geochemical reactions are assumed equilibrium if they are fast compared to transport processes and kinetically limited when reactions are characterized by timescales longer than the transport timescales. The model allows to consider fractional order and Monod-type rate expressions and the utilization of parallel reaction pathways. Consequently, it allows simulating biogeochemical kinetic and equilibrium processes and advective-dispersive transport in one, two, or three dimensions. Heterogeneous reactions can be described as surface- or transport-controlled reactions and may be reversible or irreversible [*Steefel and MacQuarrie*, 1996; *Mayer*, 2002]. For particle tracking, PTRANS code [*Maier and Bürger*, 2013] was applied which utilizes Pollock's method for rectangular grid cells [*Pollock*, 1988]. For water ages, zero order decay tracer injection was modeled, and no external code was used [*Goode*, 1996].

Additionally, the accessory micro-scale minerals were identified by scanning electron microscopy **(**LEO 1450VP) and energy dispersive X-ray spectroscopy (EDX) in samples from the Upper Muschelkalk rock formation which is relevant for the last chapter (see Appendix I).

2.2. SUBSURFACE FLOW AND REACTIVE TRANSPORT MODELING

In numerical code MIN3P [*Mayer*, 2002] the Richards equation is used as a governing equation for the variably saturated water flow [*Bear*, 1972; *Mayer*, 2002] (see Eq. 2.1). It is associated with the Mualem—van Genuchten approach for the relations of hydraulic potentials, water saturation and unsaturated hydraulic conductivity:

$$S_{aq}S_s\frac{\partial h}{\partial t} + \phi\frac{\partial S_{aq}}{\partial t} - \nabla\cdot(k_{ra}K\nabla h) - Q_a = 0 \qquad (2.1)$$

Where S_{aq} is the aqueous phase saturation (–), S_s the specific storage coefficient (m^{-1}), h the hydraulic potential (m), ϕ the porosity (–), t time (s), K the tensor of hydraulic conductivity ($m\ s^{-1}$), k_{ra} the relative permeability (–) and Q_a source/sink-term (s^{-1}). This

equation is solved through a finite volume approach using the van Genuchten–Mualem constitutive relationships [*Mualem*, 1976; *van Genuchten*, 1980; *Wösten and van Genuchten*, 1988]:

$$k_{ra} = S_{ea}^{l}\left[1-\left(1-S_{ea}^{l/m}\right)^{m}\right]^{2} \quad (2.2)$$

$$S_w = S_{ra} + \frac{1-S_w}{[1+|\alpha p_a|^n]^m} \quad (2.3)$$

$$m = 1 - {}^{1}/_{n} \quad (2.4)$$

$$S_{ea} = \frac{S_{aq}-S_{ra}}{1-S_{ra}} = \frac{\theta_{aq}-\theta_{ra}}{\theta_{sa}-\theta_{ra}} \quad (2.5)$$

where S_{ea} (–) is the effective aqueous saturation, its exponent l (–) as parameter of pore connectivity, S_{ra} (–) the residual saturation, p_a matrix potential (m) (i.e. pressure head $p_a = h - z$ under fully saturated conditions, with z as elevation relative to reference level), m (–), α (m^{-1}) and n (–) the empirical parameters of the van Genuchten formulzation, θ_{aq} is the actual aqueous volumetric water content, θ_{ra} the residual and θ_{sa} the volumetric water content at saturation for the soil (–).

The governing equation for advective-dispersive aqueous phase variably saturated porous media is:

$$\frac{\partial}{\partial t}\left(S_{aq}\phi C_a\right) + \nabla\cdot(\boldsymbol{q}C_a) - \nabla\cdot(\boldsymbol{D}\ \ \nabla C_a) - Q = 0 \quad (2.6)$$

where C_a denotes the solute concentration (kg m^{-3}), $\boldsymbol{q}$ the Darcy flux-vector (m s^{-1}), Q the source/sink term from geochemical reactions (kg $m^{-3}s^{-1}$), and $\boldsymbol{D}$ the hydrodynamic dispersion tensor (m^2 s^{-1}) given by:

$$\theta_{aq}\boldsymbol{D}\ \ = (\alpha_L-\alpha_T)\frac{\boldsymbol{q}_x\boldsymbol{q}_{y/z}}{|\boldsymbol{q}|} + \alpha_T|\boldsymbol{q}| + D_e \quad (2.7)$$

where D_e the effective diffusion coefficient (m^2 s^{-1}), α_L (m) and α_T (m) the longitudinal and transverse dispersivity respectively.

The effective diffusion coefficient D_e is described:

$$D_e = \frac{D_{aq}\theta_{aq}}{\tau_{aq}} \quad (2.8)$$

Where D_{aq} is a diffusion coefficient in water ($m^2\ s^{-1}$) and $\tau_{aq,}$ is a tortuosity factor(–), expressed based on an empirical function of porosity [*Grathwohl*, 1998]:

$$\tau_{aq} = \theta_{aq}{}^{-1.2}\ ;\ \tau_{aq} > 1 \quad (2.9)$$

Thus, the effective diffusion coefficient D_e is described in the model as

$$D_e = D_{aq}\theta_{aq}{}^{2.2} \quad (2.10)$$

An additional set of mass conservation equations describing the change of mineral quantities over time is needed to complete the system of governing equations:

$$\frac{d\varphi_i}{dt} = V_i^m R_i^m \quad i = 1, N_m \quad (2.11)$$

Where φ_i is the volume fraction of the mineral (m^3 mineral m^{-3} porous medium), V_i^m is the molar volume of the mineral (m^3 mineral mol^{-1}), R_i^m is the overall dissolution rate for the mineral (mol m^{-3} porous medium s^{-1}).

The reaction driven source/sink term *Q* for component *i* is computed from the sum of contributions of reaction rates R_j (kg $m^{-3}s^{-1}$) in the aqueous phase solution:

$$Q_i = \theta_{aq} \sum R_j \nu_{i.j} \quad (2.12)$$

Where $\nu_{i,j}$ is the stoichiometric coefficient of component *i* in reaction *j*.

The overall reaction rate, R_j of surface-controlled mineral dissolution-precipitation used for dissolution-precipitation of calcite, gypsum, siderite, ferrihydrite and goethite is:

$$R_j = -k_{eff,j}\left(1 - \frac{IAP}{K_{eq,j}}\right) \quad (2.13)$$

Where $k_{eff,j}$ and $K_{eq,j}$ refer to the effective rate constant (mol m^{-3} s^{-1}) and the equilibrium constant of reaction *j*, and *IAP* is the ion activity product.

The intra-aqueous redox reactions follow the dual Monod kinetic approach concerning concentrations of electron donor (CH2O) and electron acceptors (O_2 (aq), NO_3^-, SO_4^{2-},

NH_4^+,). Every reaction is turned off by the set of corresponding threshold terms (K_{thr}) to neglect the reaction at very low concentrations. The energy-yielding consequence of redox reactions [*Appelo and Postma*, 2005] is provided by using inhibition terms. The reactions rates R are considered to be kinetically controlled thus no equilibrium constants are needed (see Eq. 1.13, 1.14, 1.15, 1.16). The corresponding rate constants k (mol m^{-3} s^{-1}), Monod terms $K_{1/2}$ (mol m^{-3}), threshold terms K_{thr} (mol m^{-3}), r, and inhibition terms K_{inh} (mol m^{-3}), are specified separately in every chapter.

$$R_{CH2O-O_2} = k_{CH2O-O_2} \cdot \frac{C_{O_2}}{C_{O_2} + K_{1/2O_2}} \cdot \frac{C_{CH2O}}{C_{CH2O} + K_{1/2CH2O}} \cdot \frac{C_{O_2}}{K_{thrO_2} + C_{O_2}} \cdot \frac{C_{CH2O}}{C_{CH2O} + K_{thrCH2O}} \quad (2.14)$$

$$R_{CH2O-NO_3^-} = k_{CH2O-NO_3^-} \cdot \frac{C_{NO_3^-}}{C_{NO_3^-} + K_{1/2NO_3^-}} \cdot \frac{C_{CH2O}}{C_{CH2O} + K_{1/2CH2O}} \cdot \frac{C_{NO_3^-}}{K_{thrNO_3^-} + C_{NO_3^-}} \cdot \frac{C_{CH2O}}{C_{CH2O} + K_{thrCH2O}} \cdot \frac{K_{inhO_2}}{K_{inhO_2} + C_{O_2}} \quad (2.15)$$

$$R_{CH2O-SO_4^{2-}} = k_{CH2O-SO_4^{2-}} \cdot \frac{C_{SO_4^{2-}}}{C_{SO_4^{2-}} + K_{1/2SO_4^{2-}}} \cdot \frac{C_{CH2O}}{C_{CH2O} + K_{1/2CH2O}} \cdot \frac{C_{SO_4^{2-}}}{C_{SO_4^{2-}} + K_{thSrO_4^{2-}}} \cdot \frac{C_{CH2O}}{C_{CH2O} + K_{thrCH2O}} \cdot \frac{K_{inhO_2}}{K_{inhO_2} + C_{O_2}} \cdot \frac{K_{inhNO_3^-}}{K_{inhNO_3^-} + C_{NO_3^-}} \quad (2.16)$$

$$R_{NH_4^+-O_2} = k_{NH_4^+-O_2} \cdot \frac{C_{O_2}}{C_{O_2} + K_{1/2O_2}} \cdot \frac{C_{NH_4^+}}{C_{NH_4^+} + K_{1/2NH_4^+}} \cdot \frac{C_{O_2}}{C_{O_2} + K_{thrO_2}} \cdot \frac{C_{NH_4^+}}{C_{NH_4^+} + K_{thrNH_4^+}} \quad (2.17)$$

The shrinking core model is applied for pyrite oxidation by both NO_3^- and O_2 . The shrinking core model is used when dissolution reactions are controlled by the diffusion flux through an inhibition coating. The radius of the dissolving crystals is supposed to getting smaller during the process with the inhibition coating getting thicker. Specific effective reactions rates for pyrite oxidation by NO_3^- or O_2 go as following:

$$R_{py-O_2(aq)} = -10^3 \cdot S_{py} \cdot D_{py,O_2(aq)} \cdot \frac{r_{py}^p}{(r_{py}^p - r_{py}^r) r_{py}^r} \cdot \frac{C_{O_2}}{v_{py-O_2(aq),O_2(aq)}} \quad (2.18)$$

$$R_{py-NO_3^-} = -10^3 \cdot S_{py} \cdot D_{py,NO_3^-} \cdot \frac{r_{py}^p}{(r_{py}^p - r_{py}^r) r_{py}^r} \cdot \frac{C_{NO_3^-}}{v_{py-NO_3^-,NO_3^-}} \quad (2.19)$$

where $r_{py}{}^p$ (m) and $r_{py}{}^r$ (m) are the initial and unreacted particle radii. S_{py} (m^2 m^{-3}) refers to the reactive surface area scaling factor. $D_{py,x}$ (m^2 s^{-1}) denotes the intra-particle diffusion coefficient of solute in water, and $v_{py-x,x}$ denotes the stoichiometric coefficient of pyrite oxidation by O_2 which is specified separately in every chapter.

Due to various mineral precipitation and dissolution reactions, the porosity of the medium might be altered. In MIN3P, the porosity is updated after each time step based on the minerals mass balance:

$$\phi^{t+\Delta t} = \phi^t - \sum_{i=1}^{N_m} (\varphi_i^{t+\Delta t} - \varphi_i^t) \quad (2.19)$$

where $\phi^{t+\Delta t}$ (–) and ϕ^t (–) are the porosities at times $t+\Delta t$ and t. In accordance, $\varphi_i{}^{t+\Delta t}$ (–) and $\varphi_i{}^t$ (–) refer to the volume fractions of reactive mineral i at times $t+\Delta t$ and t. N_m (–) denotes the total number of reactive minerals.

2.3. STUDY AREA: AMMER AND NECKAR CATCHMENTS

Several models representative for typical landscapes in central Europe were developed in this study. While none of them were intended to represent or predict flow or transport in any real aquifer or system of aquifers, data from real catchments was used to build models realistically. The study area is situated on the west of the Tübingen, SW Germany. In **Chapters 3**, **4** and **5** the lower Ammer valley floodplain, the Spitzberg hill, and the Neckar valley floodplain upstream of Tübingen are considered including the Triassic bedrocks (Fig. 2.1). In **Chapter 6,** the transport through Upper Muschelkalk aquifer in the Ammer catchment is considered (Fig. 2.2).

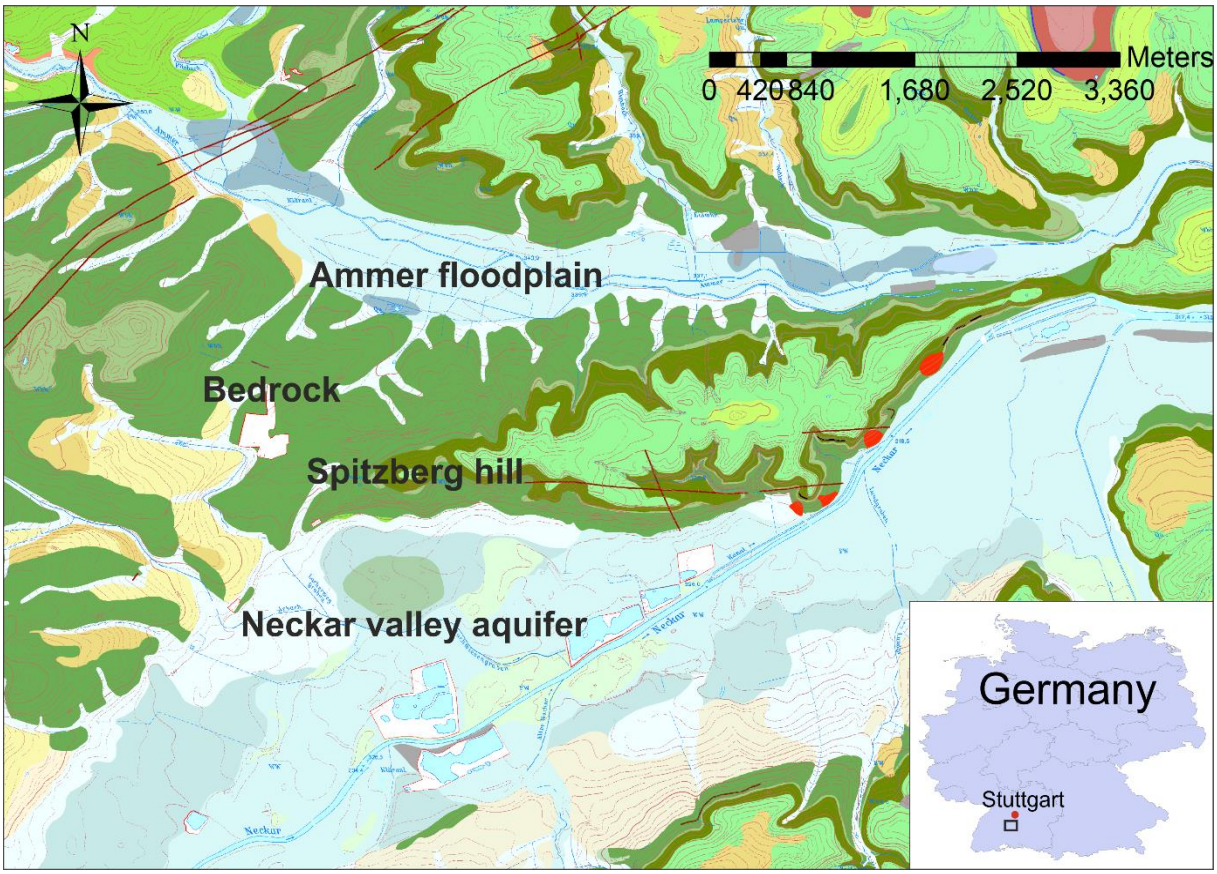

Fig. 2.1. Geological map of the study area for chapters 2, 3 and 4. Green areas represent Triassic mudstones and sandstones, blue areas represent floodplains, and yellow represent Lettenkeuper aquitard; red areas indicate former Gypsum quarries.

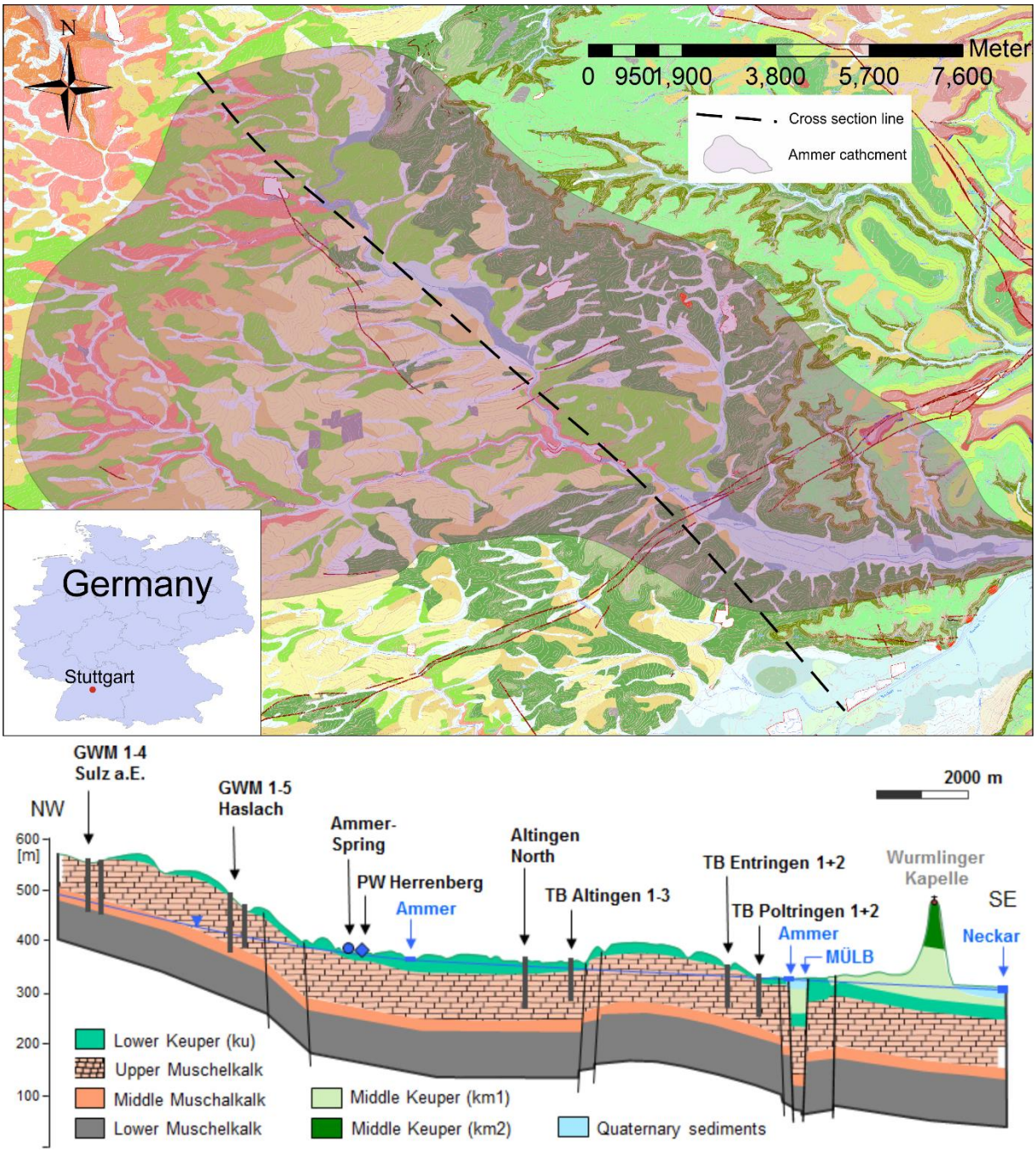

Fig. 2.2. Top: Geological map of the study area used in **chapter 6**. Green areas represent Triassic mudstones and sandstones, blue areas represent floodplains and yellow represent Lettenkeuper aquitard, and red areas represent Upper and Lower Muschelkalk which is mostly overlain by young sediments. Bottom: geological cross-section along the black dash line, adapted by K. Ostenbruck after [*Villinger*, 1982]

The Neckar valley sediments are Quaternary and consist of Pleistocene coarse gravel and sands from the Black Forest area and nearby regions. This material was transported during the last glaciation. The gravel compromises mostly Jurassic and Triassic limestone fragments and sands eroded from the Triassic sandstones [*Kostic and Aigner*, 2007]. It is overlaid by the Holocene fluvial loam consisting of sandy and silty material rich in organic matter [*Maier et al.*, 2013]. The Ammer floodplain between Tübingen and Pfäffingen consists

of alluvial loam, layers of lacustrine freshwater calcareous silts interbedded with peat (Holocene), and coarse sand and gravel at the bottom (Pleistocene) which are separated by a layer of the black plastic clay [*Grathwohl et al.*, 2017]. The River Ammer is divided into the main corridor and the channel. Several drainage ditches run parallel to the river with the typical distance between ditches of around 100 meters.

The surrounding bedrocks including the Spitzberg hill - which is the local topographical water divide - are formed by sediments of the German Triassic. The thickness of Triassic sediments is up to 3000 m in the North German basin, but only 500-1000 m or less in the South German subbasin. The basin was almost landlocked. During times of limited connections with the Tethys ocean, continental clastic sediments and evaporites were deposited. During marine ingressions, carbonates predominate.

The German Triassic is subdivided into three parts based on lithology: the predominantly continental Buntsandstein (Lower Triassic), the marine Muschelkalk (Middle Triassic), and the predominantly continental Keuper (Upper Triassic) [*Aigner and Bachmann*, 1992]. In the research area the layers have in general a 3° inclination to the South-West. The hillslope consists of Keuper deposits. Keuper is the dominant sequence in the area of interest and forms most of the relief of the local landscape. The Muschelkalk-Keuper boundary is characterized by a regional angular unconformity which is overlain by the 30 cm thick layer of prefossilized debris of bones, teeth, etc. of predominantly marine vertebrates and contains a considerable amount of quartz sand. These deposits are followed by the first Keuper subdivision – Lettenkeuper, which includes sandstones and limestones bed as well as dolomites and grey shales [*Aigner and Bachmann*, 1992]. It forms a regional aquitard.

The next sequence is Gipskeuper forming the surface of the landscape and the bed for the quaternary deposits in the study area. In Southwestern Germany, the Gipskeuper formation represents a transition from marginal marine to continental red bed conditions. While the basal Gipskeuper includes 12-20 m of massive evaporite rocks, red, greenish, greyish and varicolored claystone, marlstones, some sandstone and thin dolomitic intervals dominate its upper part. Depending on the type of exposure the sulfates occur either as gypsum or anhydrite [*Aigner and Bachmann*, 1989].

The upper parts of the hills in the study area are formed by Schilfsandstein (sandstones), Liwer and Upper Bunte Mergel (mudstones), Stubensandstein (arkose/sandstones), Knollenmergel (mudstones) and Rhät (sandstones).

The limestones from the Muschelkalk not only form a major regional fractured aquifer system but also play a significant role as a source of materials for fluvial quaternary sediments. The formation is subdivided into Lower Muschelkalk, Middle Muschelkalk and Upper Muschelkalk.

The Lower Muschelkalk consists of fluvial and lacustrine sand- and siltstones, represented by red shales, siltstones and local dolomite bands and gypsum nodules as well as marine limestone and shales.

The Middle Muschelkalk consists of evaporites (halites and anhydrides) that were deposited in the center of the basin.

The Upper Muschelkalk, which is the objective strata in **Chapter 6,** consists of numerous stacked meter-scale stratigraphic cycles. Typically, these have a shale-rich base, followed by calcareous tempestites and calcarenitic layers at the top with bioclasts, ooids, and intraclasts, sometimes dolomitized. Several layers of clay divide the aquifer into zones.

The landscapes of concern are formed by River Neckar and its tributaries. Schwarzwald Mountains limit the area of expansion of such valleys at the west and south-west and divide the Neckar and Rhine catchments. The Swabian Alb, where Triassic sediments are overlain by Jurassic sediments, limits the area of expansion of such valleys to the East and Southeast and separates the landscape from the influence of the Alpine Molasses.

3 GROUNDWATER DIVIDE POSITION BETWEEN NECKAR AND AMMER VALLEY

The groundwater table is commonly assumed to be a subdued replica of the ground surface. The topographic highs therefore are frequently used as groundwater divides especially when the groundwater data are sparse. This assumption however only stands under particular conditions which are frequently not fulfilled [*Schwartz and Zhang*, 2003; *Anderson et al.*, 2015]. When outer non-permeable boundaries of a catchment model are purely derived from the topographical map they might not represent real groundwater divides which would lead to miscalculation in water and solute fluxes and consequently to wrong predictions in groundwater flow and transport.

In chapter 3 of this thesis, very common groundwater system is investigated where due to long established rivers management the natural groundwater table configuration is affected. The result show not only that the topographical water divide cannot be used as a proxy of catchment boundary but also that the possible range of groundwater divide positions can be constrained with very scarce data. In consequence, no catchment model predictions in such landscapes can be considered reliable without extensive study of the groundwater divide positions.

3.1 INTRODUCTION

The groundwater divide is not always aligned with a topographical one [*Freeze and Cherry*, 1979; *Haitjema and Mitchell-Bruker*, 2005; *Gleeson et al.*, 2011]. This, however, is often not considered in catchment scale flow and transport studies. Groundwater divide between two valleys can be significantly shifted with respect to the geographical water divide in cases of substantial water level differences in both valleys. This would cause inter-valley flow of groundwater and therefore inter-valley pollutant transport.

The 2-D flow model was developed for a representative vertical cross-section cutting through the lower Ammer valley, the connecting Spitzberg hill, and the Neckar valley upstream of Tübingen, southwestern Germany. Similar situations can be found in many landscapes in Central Europe that have similar geology, history, and land use. The valleys boundaries are often used as the catchment boundaries for modelling and such assumption should be tested with more simplistic models.

This part of the research aims to answer following questions:

1) How well can the groundwater divide be constrained with limited data?
2) What are the most important parameters controlling the flow in the system and the position of the water divide?
3) Can some of this parameters be estimated without extensive field experiments?

3.2 FLOW MODEL SETUP

The valleys of river Neckar and its tributary, Ammer, are located in the German Triassic Basin comprised of sedimentary rocks. The study area represents a typical South-western Germany landscape. Fig. 3.1 shows the location of the cross-section used for the reactive transport model as well as the supposed subsurface and surface water divides.

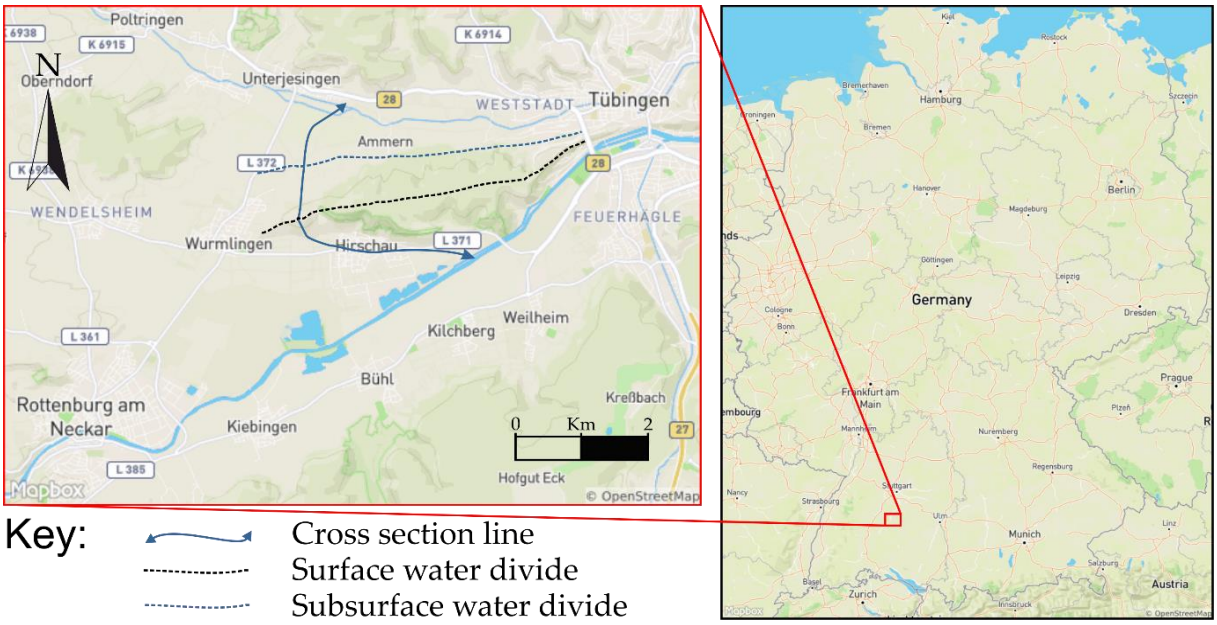

Fig. 3.1. Location of the study area in SW-Germany with supposed location of the subsurface and surface water divides. The blue line with arrows indicates the cross-section used for numerical modeling.

Fig. 3.2. Shows the conceptual model setup for a vertical cross section cutting through the lower Ammer valley, the Spitzberg hill (surface water divide) and the Neckar valley. The geology comprises seven major layers: Stubensandstein (top), Bunte Mergel, Schilfsandstein, and at the bottom, the Gipskeuper (gypsum-bearing) mudstones which form the bedrocks of the valleys. The floodplain sediments of the Neckar valley comprise the typical Pleistocene sand and gravel deposits with a thickness of 6 - 10 meters topped by 2 m Holocene alluvial and diluvial floodplain loam. In the Ammer valley, the only 2 meters thick Pleistocene sand and gravel deposits are overlain by calcareous lakes sediments with peat layers, topped by

Holocene loam. Every major layer was conceptualized as internally homogeneous because of the large scale of the model. Geometry and hydraulic parameters are compiled in Tab. 3.1. For the Ammer floodplain, averaged parameters were used due to the comparably small scale of the layers.

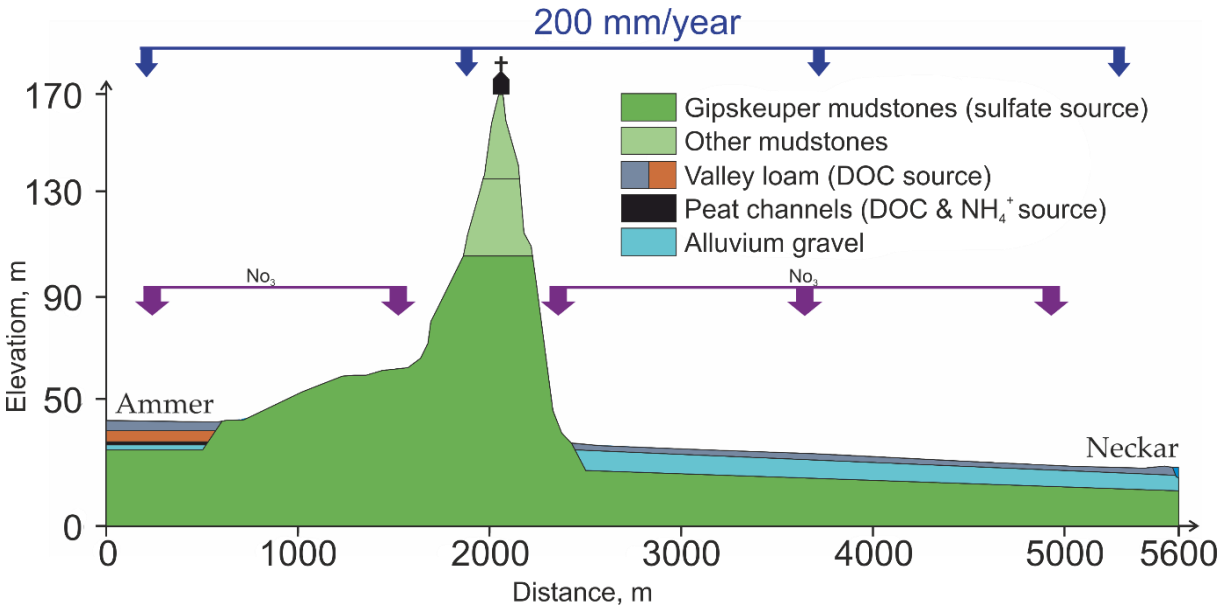

Fig. 3.2. N-E cross-section from Ammer to Neckar river through Wurmlingen Chapel (google elevation model, vertically exaggerated) following the streamline assumed after [*Schollenberger*, 1998] and conceptual model for flow and reactive transport simulations.

3.3 FLOW MODEL

The numerical model was constructed based on the conceptual model with seven homogeneous compartments. The hydraulic conductivity of the Neckar gravel aquifer was fixed to 0.003 m/s based on previously reported data [*Maier et al.*, 2013]. The hydraulic conductivity of other layers was calibrated based on recharge rates and water tables observed. The parameters ranges used for calibration are shown in Table 3.1.

Table 3.1. Hydraulic conductivity ranges and other parameters used for model calibration and flow simulations.

Stratigraphic unit	Hydraulic conductivity (m/s)	Porosity, ϕ [-]	Thickness [m]	Van Genuchten parameters α/N [1/m]
Ammer floodplain (loam and silt)	1×10^{-4} - 1×10^{-8}	0.4	10	0.8/1.2
Neckar valley alluvial loam	1×10^{-6}	0.4	2	0.8/1.2
Neckar valley gravel body	1×10^{-3} [a]	0.2	8	35/5.3 [a]
Gipskeuper mudstones	1×10^{-7} - 9×10^{-5}	0.03-0.4	106-15	4/1.3
Other mudstones	1×10^{-7} - 9×10^{-5}	0.03-0.4	64	4/1.3
Ammer floodplain (gravel)	1×10^{-5}	0.2	2	35/5.3

[a] [*Maier et al.*, 2013]

The simulated cross-section is 5600 meters long and 170 meters high. The numerical mesh grid is uniform, and all the cells have dimension 5×1 meters. A fixed flux (Neumann) boundary was used at the top of research domain with a recharge rate of 200 mm/year (according to *LUBW*, [2011]; *Selle et al.*, [2013]). Fixed hydraulic heads (Dirichlet boundaries) were used for the rivers at the left and right sides because the lateral extension is limited by major rivers. Hydraulic heads of 24 and 36 meters were used for Ammer and Neckar boundaries correspondingly. A no-flow boundary (regional aquitard) was applied to the bottom of the modeling domain. Steady-state flow simulations with different sets of parameters were performed for calibration and sensitivity analysis as well as to determine possible positions of the groundwater divide between the two valleys.

3.4 RESULTS AND DISCUSSION

The model results are most sensitive to the Gipskeuper mudstones compartment conductivity which have to be in a relatively narrow range of 3×10^{-6} - 5×10^{-5} m/s. At lower values the groundwater table would be above ground (resulting in springs in the Ammer valley which are not observed) – at higher values, the Ammer river would drain, and all groundwater from the Ammer valley would flow towards river Neckar. In both extreme cases, the groundwater divide is shifted towards the Ammer river (see Fig.3.3).

More moderate conductivity changes in a range of 7×10^{-6} - 1×10^{-5} m/s (Fig. 3.3b and Fig 3.3c) results in a shift of groundwater divide into the Ammer valley at a narrow location of 850 - 900 m distance from river Ammer. These results did not significantly depend on the

conductivity of the other layers/compartments. Also, tests with different anisotropies did not influence the position of the groundwater divide.

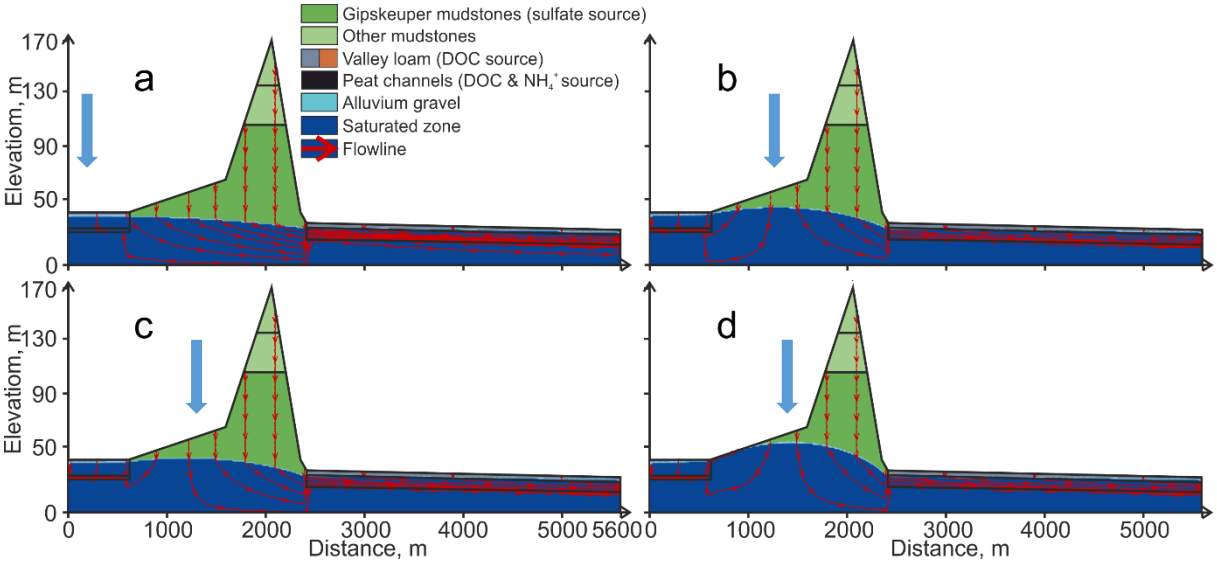

Fig. 3.3. Water tables and groundwater divide as a function of decreasing Gipskeuper hydraulic conductivities: (a) 5×10^{-5}, (b) 1×10^{-5}, (c) 7×10^{-6}, (d) 3×10^{-6} m/s, flow lines in red; with decreasing K groundwater tables rise and the water divide shifts to the right but is stable for K < $1x10^{-5}$ m/s. Blue arrows indicate groundwater divide positions.

The sensitivity of effective Ammer floodplain conductivity was also tested in a large range (K = 1×10^{-4} - 1×10^{-8} m/s) (see Fig. 3.4). The results show that it only affects the water levels in the Ammer floodplain and the shift of the groundwater divide is negligible. To keep the water level in the Ammer floodplain below ground, the effective floodplain conductivity has to be higher than 1×10^{-7} m/s, which is consistent with the silts and calcareous sediments observed.

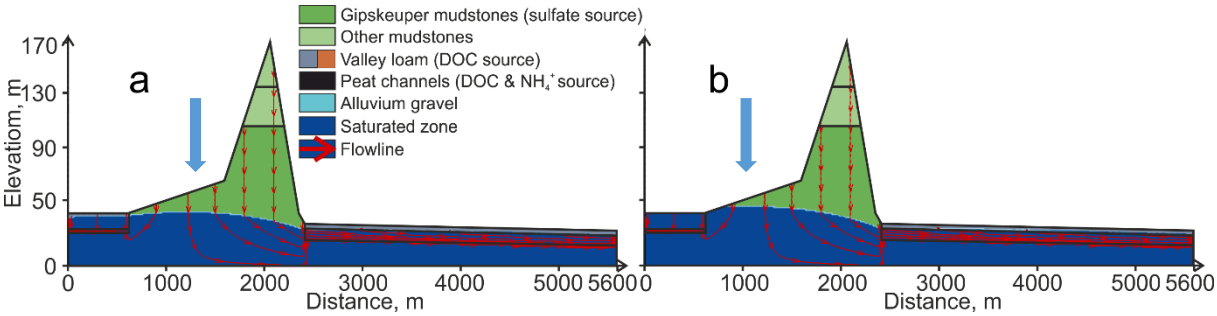

Fig. 3.4. Water saturation distribution (blue – saturated) with Gipskeuper hydraulic conductivity of 1×10^{-5} m/s and Ammer loam conductivities of (a) 1×10^{-4} and (b) 1×10^{-8} m/s. The groundwater divide does not shift significantly, but the water level in the Ammer floodplain rises. Blue arrows indicate groundwater divide positions.

Both groundwater levels and the subsurface water divide position are not sensitive to the conductivity of the Ammer gravel layer, Neckar gravel body or Neckar alluvial loam. While the groundwater table at steady state flow is not affected much by porosity, it still affects the groundwater flow velocity. Moreover, the mudstones are essentially a dual porosity media [*Barenblat et al.*, 1960], where the fracture and the matrix porosity are very different. Advective transport usually dominates in fractures and diffusion does in the matrix. Matrix diffusion may lead to significant retardation if long transport distances are considered [*Tang et al.*, 1981]. To determine the necessity of introducing dual porosity concept in the future transport model, a "low porosity case" scenario (porosity of the Gipskeuper mudstones set to 0.03), where mostly advective flow through the fractures occurs, as the fastest possible scenario was tested. The maximum lifetime expectancy for the particles starting in the mudstones is 17 years and just ten years are spent in the mudstones themselves which is a negligible time for matrix diffusion (Fig. 3.5). Thus, the dual porosity effect on a breakthrough curve is negligible. However, if the matrix porosity is included, part of the contaminant mass would accumulate in the mudstones rock matrix and in case of remediation would back-diffuse into the fractures increasing the remediation time scales. For the particles started on the Ammer side of the water divide at the hillslope, the lifetime expectancy is lower than for ones stated on the floodplain due to the high effective conductivity of the later.

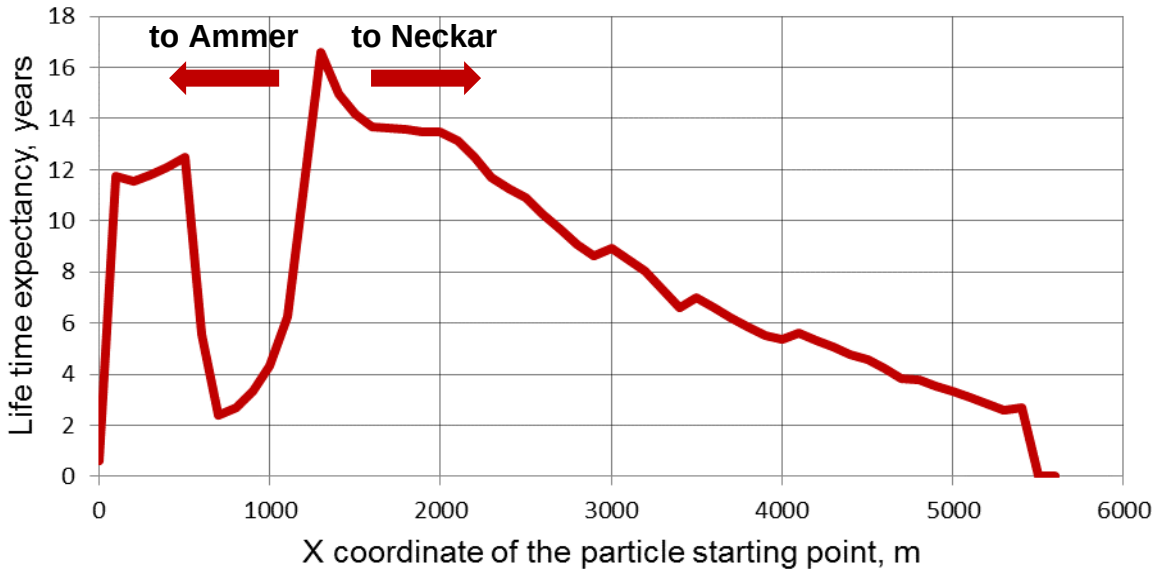

Fig. 3.5. The particles lifetime expectancy dependence on the particle release position for low porosity scenario

3.4.1 LOCATION OF GROUNDWATER DIVIDE AROUND THE WURMLINGEN CHAPEL AREA AND ITS SENSITIVITY

The geological conditions and the high difference between water lever in Neckar and Ammer Rivers determine the shift of the groundwater divide comparing to the topographical one. Thus, a significant fraction of the groundwater recharge generated in the Ammer valley flows towards river Neckar.

Both groundwater levels and the subsurface water divide position are not sensitive to the conductivity of the Ammer gravel layer, Neckar gravel body or Neckar alluvial loam in realistic parameters ranges. However, the Gipkeuper conductivity significantly affects the groundwater divide position. In the range of conductivities of 3×10^{-6} - 5×10^{-5} m/s it moves from nearly being underneath the topographical divide to the Ammer river and all water generated in the Ammer valley flows from into Neckar valley. In the more moderate scenarios (7×10^{-6} - 1×10^{-5} m/s), the water divide tends to be below the hillslope with little oscillations. The position of the groundwater divide can be estimated thus without any extensive data if geology and topography of the system are reasonably well known. Moreover, the effective conductivity of the bedrock, the only sensitive parameter, can be estimated in the case when it is proved that both rivers gain water and no springs are observed on the hillslope. The presence of hillslope springs, however, would provide an even more precise estimation of the water divide and conductivity values.

3.5 CONCLUSIONS

The Neckar-Ammer valley neighboring catchments represent a typical scenario of uplands in humid areas where due to different river water levels and depending on recharge rates the groundwater divide significantly deviates from the surface water divide. Numerical modeling of reactive solute transport shows that despite uncertainties in hydraulic conductivity the shift of groundwater divides depends on water level difference size in the two rivers (often hydraulically controlled by river management), local topography of the hill water divide, hydraulic conductivity of bedrock and groundwater recharge.

Modelling results confirm that under the most realistically calibrated set of parameters, inter-valley groundwater flow becomes essential. The distance between groundwater and topographical water divide is almost half of the size of the Ammer valley and one third of the Neckar valley. In this case, the difference between valleys and catchments boundaries becomes significant, and if not considered the water balances in the catchment

models would never match the reality. The transit of contaminants from one valley into the groundwater of the adjacent valley also would not be recognized.

The position of groundwater divide, as well as hydraulic parameters of bedrock, can be estimated reasonably well based on topography and water levels of the rivers. The effective hydraulic conductivity of other compartments cannot be estimated based on this approach and with this model resolution. More importantly, the heterogeneity of the bedrock also cannot be quantified causing high uncertainty in the transport simulations.

4. LANDSCAPE SCALE REACTIVE TRANSPORT OF NITRATE ACROSS A TOPOGRAPHICAL WATER DIVIDE

As shown in chapter 3, the groundwater divide between the Neckar and Ammer catchments is shifted with respect to the topographical water divide towards the Ammer river. This shift provides the substantial groundwater flow from Ammer valley into the Neckar valley and therefore causes the export of solutes. The chapter 4 explores the importance of considering such inter-valley fluxes since it leads to the formation of contaminates plumes (e.g. the agricultural nitrate) which would be unexpected in case the catchment boundary was derived purely from topography as it is commonly done [*Schwartz and Zhang*, 2003]. Moreover, the behavior of potential solute plumes in the Neckar valley is investigated to provide better insights in relevant processes and features.

4.1 INTRODUCTION

Diffuse groundwater pollution caused by agricultural and atmospheric inputs is a pressing issue in environmental management worldwide [*Refsgaard et al.*, 2014]. The focus of this study is on nitrate, which is applied on the vulnerable areas and transported through oxidized sedimentary bedrocks into the floodplains. Many studies describe nitrate contamination (e.g., [*Böhlke et al.*, 2002; *Howden et al.*, 2011; *Tesoriero and Puckett*, 2011; *Hansen et al.*, 2014; *Heppell et al.*, 2014] and sources of uncertainty and their importance in transport modelling [*Cirpka et al.*, 2012]. However, there is still lack of mechanistic catchment-scale studies, elucidating turnover of nitrogen species on the landscape scale. Processing of nitrate in Quaternary sediments, particularly, is known to be affected by the complexity and heterogeneity of the geologic and geochemical settings [*Best et al.*, 2015]

This part of the study focuses on the sensitivity of reactive nitrate transport on hydrochemical, hydraulic, and geometrical parameters, exemplified by the Neckar-Ammer system in order to answer following questions:

1. Where does the nitrate observed in the Neckar-valley aquifer originate?
2. What is the fate of Nitrate when it enters the sediments of the floodplains?
3. What parameters control the nitrate transport in the Neckar floodplain?

The work is based on an earlier study by *Maier et al.* [2013], who studied the long-term geochemical evolution of seepage and groundwater chemistry in a cross-section of the Neckar valley by 2-D reactive transport modeling, highlighting the importance of the internal architecture of the sediments and their reduction capacity. *Schollenberger* [1998] provided a

detailed description of the groundwater chemistry in the Neckar valley gravel aquifer, describing sulfate and nitrate plumes. This data indicate sulfate and nitrate plumes originating from the Gipskeuper mudstones at the northern margin of the valley (Fig. 4.1). *Selle et al.* [2013] implemented a first groundwater model for the Ammer valley which was extended in the current analysis. In particular, the flow model developed and described in chapter 3 suggests that the Ammer and Neckar valleys should be considered as a connected system. Based on the flow field a multi-component advective-dispersive reactive transport model was designed which considers the most relevant redox-sensitive species (dissolved oxygen, nitrate/ammonium, sulfate/sulfide, ferrous/ferric iron, DOC, and TOC in solids), the carbonate system, and the dominant reactive mineral phases (gypsum, pyrite, calcite).

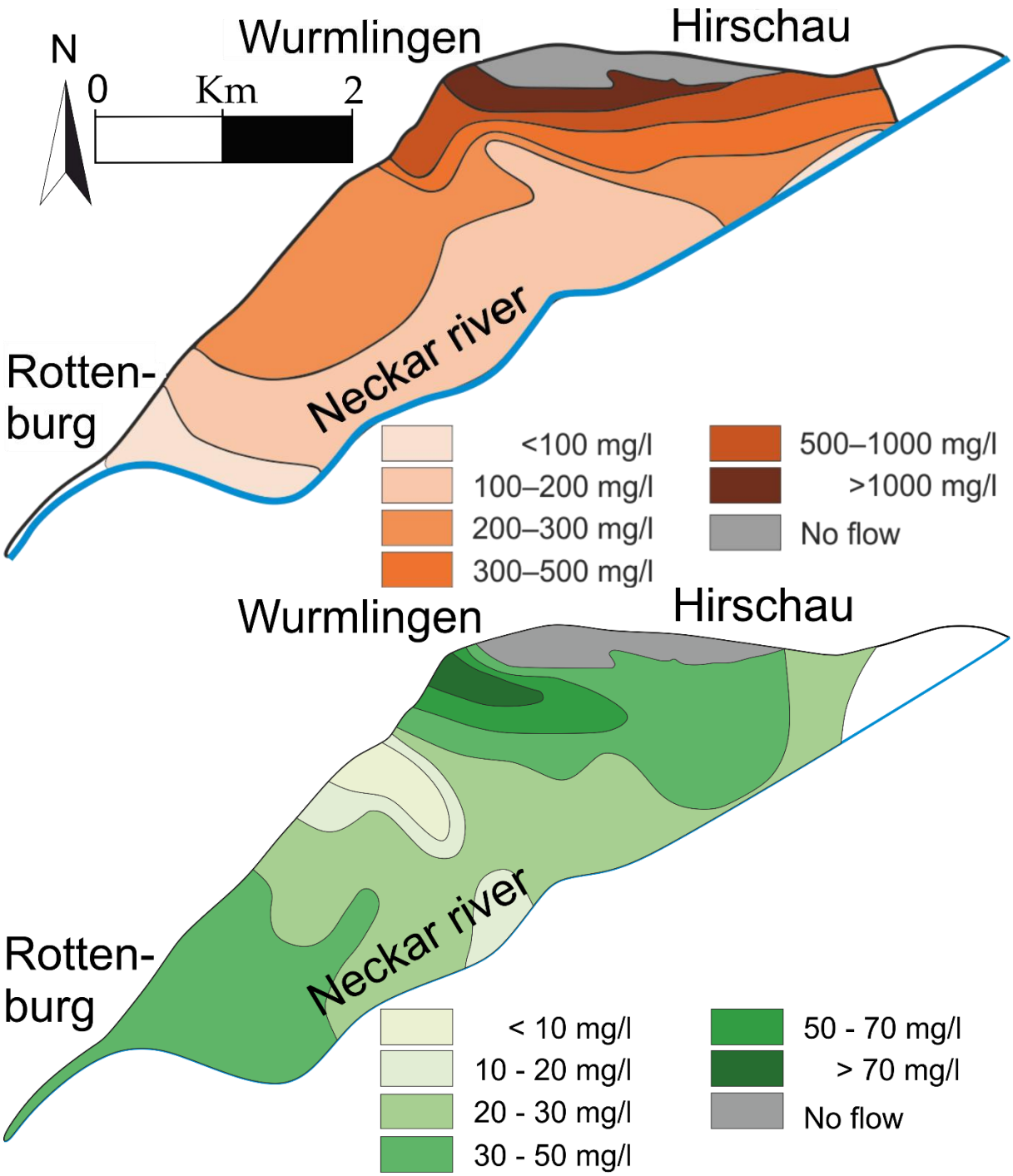

Fig.4.1. Sulphate (top) and nitrate (bottom) concentration distribution in the Neckar valley gravel aquifer (see Fig. 3.1) modified after *Schollenberger* [1998]. Sulphate comes from the Spitzberg hillslope due to high gypsum content in the Triassic mudstones. Nitrate comes from the same direction, possibly from the Ammer valley.

4.2 REACTIVE TRANSPORT MODEL SETUP

Because of the hydraulic head difference in Ammer and Neckar rivers of 12 m, the groundwater divide shifts far into the Ammer catchment and thus the focus of reactive transport modeling is on nitrate transport towards the Neckar valley sand and gravel aquifer. The velocity field from the steady state flow model with parameters obtained in chapter 3

(Table 4.1) was used for reactive transport simulations., the Neckar and Ammer rivers were set as a free exit boundaries (Neumann), and the top of the model was set as a specified concentration boundary (Dirichlet).

Table 4.1. Hydraulic conductivities used for flow model for obtaining the flow field

Stratigraphic unit	Hydraulic conductivity (m/s)	Porosity, ϕ [-]	Thickness (m)	Van Genuchten parameters α/N (1/m)
Ammer floodplain (loam and silt)	1×10^{-6}	0.4	10	0.8/1.2
Neckar valley alluvial loam	1×10^{-6}	0.4	2	0.8/1.2
Neckar valley gravel body	1×10^{-3}	0.2	8	35/5.3 [a]
Gipskeuper mudstones	1×10^{-5}	0.03	106-15	4/1.3
Other mudstones	1×10^{-5}	0.03	64	4/1.3
Ammer floodplain (gravel)	1×10^{-5}	0.2	2	35/5.3

The hydrogeochemistry of the region is governed by the presence of carbonate and sulfate-rich stratigraphic units (calcite and gypsum/anhydrite) and to some extent by redox-sensitive species which may lead to depletion of oxygen; these include organic carbon and thus DOC in top soils and organic-rich layers, such as peat [*Maier et al.*, 2013] (Table 4.2).

Table 4.2. Initial mineral volume fractions used for reactive transport modeling.

Stratigraphic unit	Calcite (vol %)	TOC (vol %)	Gypsum (vol %)
Ammer floodplain (loam and silt)	0	10	0
Ammer floodplain (gravel)	10	0	0
Gipskeuper mudstones	10	0	30
Neckar valley gravel body	10	0	0
Neckar valley alluvium loam	0	1	0

The hydrogeochemical model considers the most relevant redox-sensitive species: dissolved oxygen, nitrate, sulfate, CH_2O (DOC), and TOC in solids as well as the carbonate system, and dominant reactive mineral phases (gypsum, calcite). The geochemical components and reactions considered are shown in Table 4.3.

Gas dissolution/exsolution (O_2/O_2(aq), CO_2/carbonate, H_2S/H_2S(aq) and N_2/N_2(aq)) were set up as equilibrium reactions. For mineral dissolution/precipitation of calcite and gypsum, a quasi-equilibrium approach was followed. CH_2O (DOC) release from organic carbon bearing layers was assumed to be in equilibrium with organic matter yielding a CH_2O concentration in ranges from 1 to 30 mg/l, which is common for soil leachates [*Michalzik et al.*,2001; *Moore et al.*, 2008; *Oosterwoud et al.*, 2010]. Several equilibrium concentrations of CH2O were tested in the model. The intra-aqueous redox reactions follow the dual Monod approach concerning concentrations of electron donor (CH_2O) and electron acceptors (O_2 (aq), NO_3^-, SO_4^{2-}). Every reaction is turned off by the set of corresponding threshold terms (k_{thr}) to neglect the reaction at very low concentration. The energy-yielding consequence of redox reactions [*Appelo and Postma*, 2005] were provided by using inhibition terms. The reactions rates R are considered to be kinetically controlled thus no equilibrium constants are needed. The rate constants k, Monod terms $K_{1/2}$, threshold terms K_{thr}, and inhibition terms K_{inh} are also given in Table 4.3.

Table 4.3. An overview of the geochemical system considered for the reactive transport model

Components		
O_2 (aq), CH_2O (DOC), Carbonate, pH, Ca^{2+}, SO_4^{2-}, HS^-, NO_3^-, N_2 (aq)		
Minerals		
Calcite, Gypsum, Organic carbon (SOM)		
Carbonate species	**log K_{eq}**	
$H_2CO_3 \rightleftarrows H^+ + HCO_3^-$	-6.36	
$HCO_3^- \rightleftarrows H^+ + CO_3^{2-}$	-10.33	
Gases (in equilibrium with aqueous phase)	**log K_{eq}**	
O_2 (g) $\rightleftarrows O_2$ (aq)	-2.89	
CO_2 (g)+ $H_2O \rightleftarrows H_2CO_3$	-18.2	
H_2S (g) $\rightleftarrows H_2S$ (aq)	-7.99	
N_2 (g) $\rightleftarrows N_2$ (aq)	-3.18	
Solid phase (dissolution/precipitation)	**log K_{eq}**	**k*eff* [mol/(L·bulk·s)]**
TOC $\rightarrow$ CH_2O	-3 – -5	1×10^{-6}
$CaCO_3$ (s) $\rightleftarrows Ca^{2+} + CO_3^{2-}$	-8.48	1×10^{-6}
$CaSO_4$ (s) $\rightleftarrows Ca^{2+} + SO_4^{2-}$	-4.58	1×10^{-6}
Intra-aqueous dual Monod kinetic reactions involving DOC		
$CH_2O + O_2$ (aq) $\rightarrow$ CO_2 (aq) + H_2O (For kinetics see Eq. 2.14)	$k_{CH2O\text{-}O2} = 5\times10^{-8}$ mol l^{-1} s^{-1} $K_{1/2O2} = 3.12\times10^{-6}$ mol l^{-1} $K_{1/2CH2O\ 2} = 1\times10^{-4}$ mol l^{-1} $K_{thrO2} = 1\times10^{-10}$ mol l^{-1} $K_{thrCH2O} = 1\times10^{-10}$ mol l^{-1}	
$CH_2O + 4/5NO_3^- + 4/5H^+ \rightarrow CO_2$ (aq) + $2/5N_2$ (aq) + $2/5H_2O$ (For kinetics see Eq. 2.15)	$k_{CH2O\text{-}NO3-} = 1\times10^{-9}$ mol l^{-1} s^{-1} $K_{1/2NO3-} = 8.06\times10^{-6}$ mol l^{-1} $K_{1/2CH2O} = 1\times10^{-4}$ mol l^{-1} $K_{thr\ NO3-} = 1\times10^{-10}$ mol l^{-1} $K_{thrCH2O} = 1\times10^{-10}$ mol l^{-1} $K_{inh\ O2} = 6.25\times10^{-6}$ mol l^{-1}	
$CH_2O + 1/2SO_4^{2-} + 1/2H^+ \rightleftarrows CO_2$ (aq) + $1/2HS^-$ (For kinetics see Eq. 2.16)	$k_{DOC\text{-}SO4-} = 1\times10^{-10}$ mol l^{-1} s^{-1} $K_{1/2\ SO4-} = 1.6\times10^{-3}$ mol l^{-1} $K_{1/2DOC2} = 1\times10^{-4}$ mol l^{-1} $K_{thr\ SO4-} = 1\times10^{-10}$ mol l^{-1} $K_{thrDOC} = 1\times10^{-10}$ mol l^{-1} $K_{inh\ O2} = 3.13\times10^{-5}$ mol l^{-1} $K_{inh\ NO3-} = 1.6\times10^{-5}$ mol l^{-1}	

The initial chemical conditions were calculated to be in equilibrium with the minerals in each layer. A constant concentration of solutes was used for the rainwater applied at the top boundary (Table 4.4). Other major solutes like Na^+ or K^+ etc. were not considered due to their minor effect on the redox reactions. After reaching quasi steady-state conditions, a NO_3^- concentration of 10 mg/l was applied for the complete top boundary or different intervals

along the model (source only in Ammer valley or source along the whole model) with the same concentrations of other solutes.

Table 4.4. Geochemical boundary conditions used for the reactive transport model until the quasi steady state occurs the model.

Component	Natural rainwater composition (mol/l)
O_2 (aq)	0.00026
CH_2O	0
CO_3^{2-}	3.95E-04
Ca^{2+}	0.00001
SO_4^{2-}	0.00001
NO_3^-	0

4.3 RESULTS

Two cases of nitrate input scenarios were tested regarding the geometry of the source: i) the source was located only in the Ammer part of the system **(**Fig. 4.2a**)** ii) homogeneous nitrate input was applied for a whole length of the cross-section **(**Fig. 4.2b and Fig. 4.2d**)**. This was done to show the significance of the Ammer valley nitrate input in the nitrate appearing in the Neckar-valley. Fig. 4.2a shows the nitrate plume which originates only in the Ammer valley and which appears at the bottom of the Neckar valley aquifer. The plume then mixes with DOC bearing soil leakage water from the topsoil, which contributes to degradation of nitrate from the Ammer valley and thus the plume achieves quasi-steady state. In this scenario, all nitrate is being naturally attenuated. The gravel body, therefore, becomes a source of carbonate (Fig. 4.2c). The natural electron acceptors (O_2, SO_4^{2-}) also react with the DOC in seepage water and consequently a redox zonation forms (Fig 4.2e, 4.2f.). Usually, nitrate would be applied on the whole cross-section surface, not only in the Ammer valley. In this scenario, the nitrate plume increases since nitrate is also applied on the hillslopes (vineyards). However, groundwater recharge in the Neckar floodplain has low concentrations of O_2 and NO_3^- and still contains some DOC due to DOC release in the top loam. (Fig. 4.2d). Hillslope water, entering the aquifer from the mudstones is oxidized and mixes with the infiltrating reduced water which downstream leads to a reduction of oxygen, sulfate, and nitrate. Reaction rates depend on vertical transverse dispersivities. This dramatically increases

the importance of the Ammer valley as pollutants source for the Neckar valley groundwater body. The natural attenuation of nitrate is controlled by transverse mixing and may lead to complete reduction far before the river Neckar is reached (Fig 4.2b).

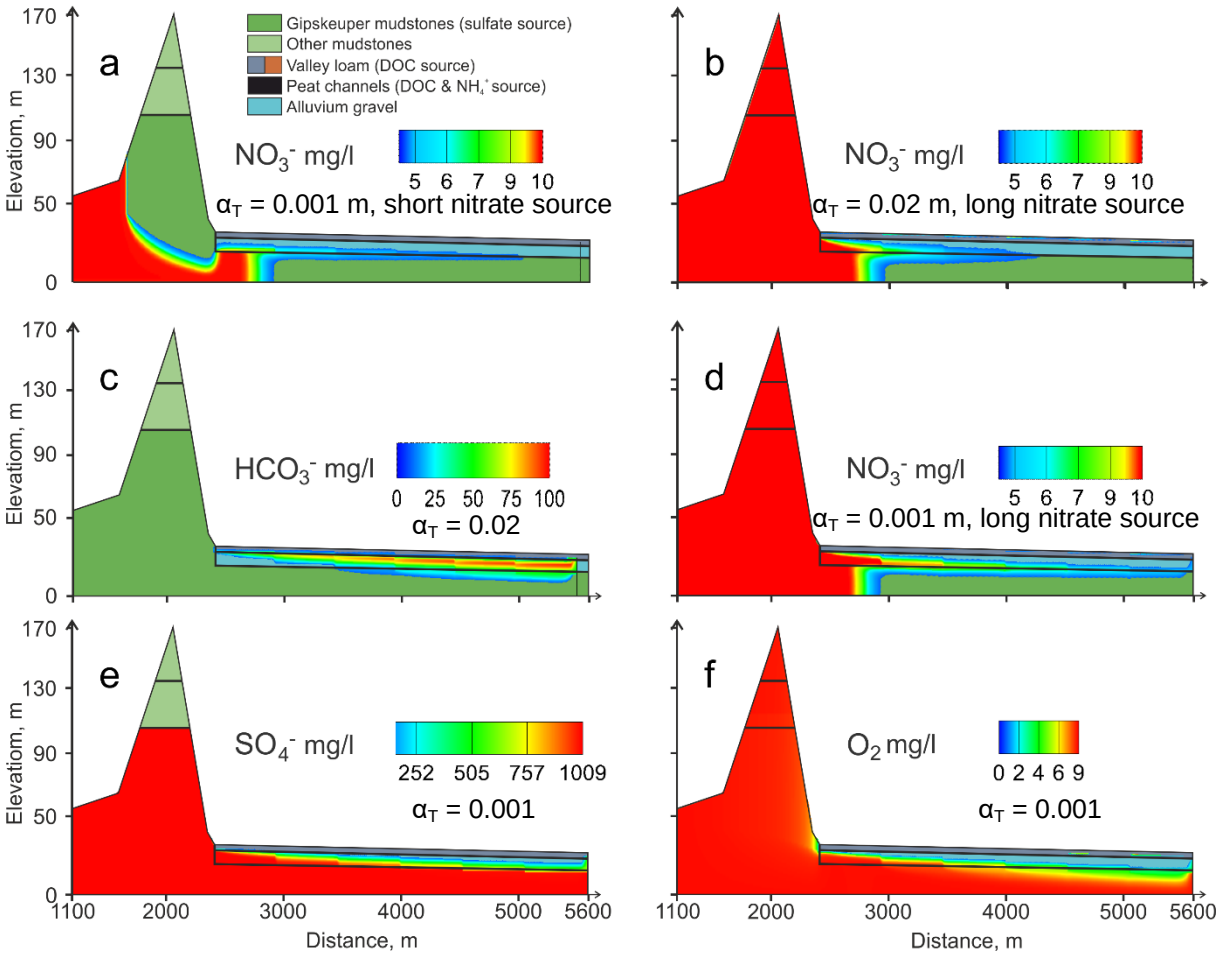

Fig. 4.2. Simulated spatial distribution of chemical species: (a) NO_3^- when only the Ammer valley acts as source, transverse dispersivity = 0.001 m, (b) NO_3^- applied in total area, transverse dispersivity = 0.02 m, (c) HCO_3^- for a transverse dispersivity of 0.02 m, (d) NO_3^- applied in total area, transverse dispersivity = 0.001 m, (e) SO_4^{2-} for a transverse dispersivity of 0.001 m, (f) O_2 for a transverse dispersivity of 0.001 m. In all cases, the nitrate plume reaches the bottom of the Neckar aquifer.

Transverse dispersivities in the Neckar aquifer ranging from 0 m (only numerical dispersion) to 0.02 m were tested. The higher the dispersivity, the more nitrate is consumed downgradient in the aquifer (Fig. 4.3). Close to the entry into the aquifer (at 3000 m.) difference in dispersivities play a minor role. At the end of the plume, almost all oxygen is exhausted by reaction with DOC in both high and low dispersivity cases and NO_3^- is attenuated as well, however, in low dispersivity case the concentration of NO_3^- is still high(see Fig. 4.3). The dispersivity affects the dissolved oxygen and nitrate. However, sulfate

concentrations are not so sensitive due to inhibition of reactions in presence of other electron acceptors and low reaction rate.

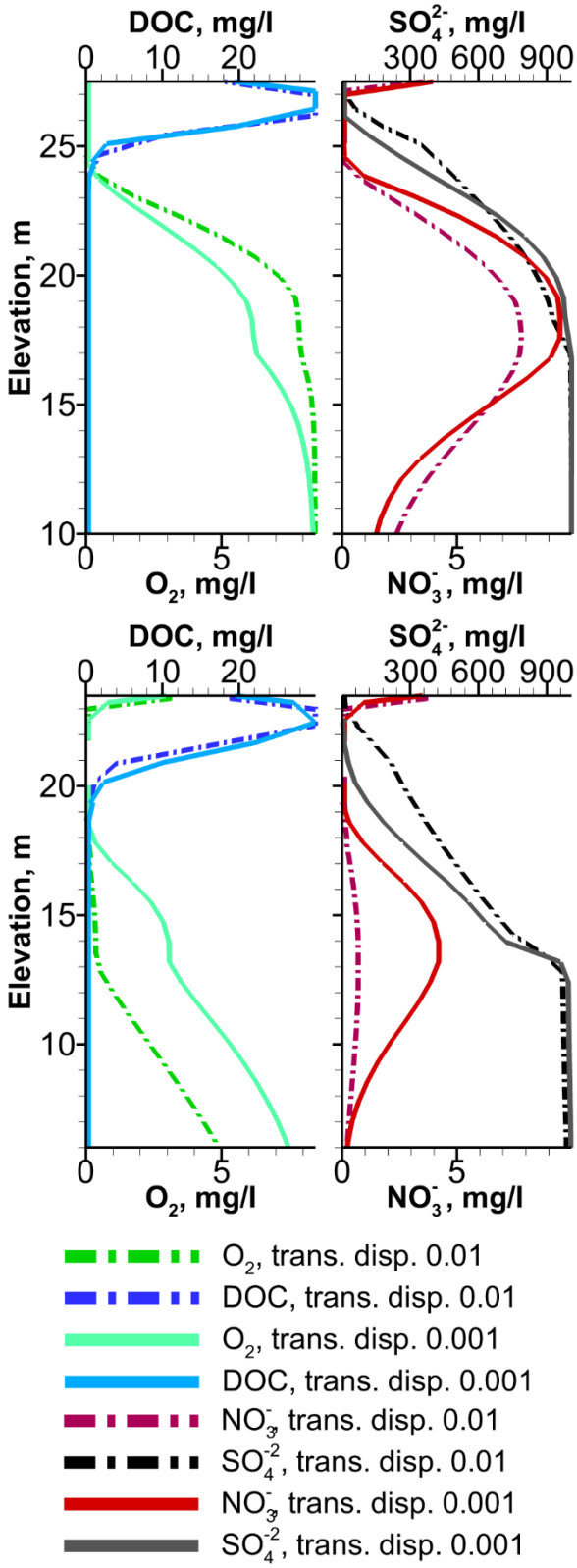

Fig. 4.3. Cross section through the quasi-steady-state Neckar gravel-body plume for the redox-sensitive elements at the beginning of the plume at 3000 m where hillslope water enters the sand and gravel aquifer (top) and near the discharge zone at a distance of 5400 m (bottom); dotted lines: transverse dispersivity = 0.01 m, solid lines; transverse dispersivity = 0.001 m. Infiltration water DOC conetration 30 mg/l.

With lower dispersivity, the change in concentration of DOC significantly affects amount of the nitrate being reduced (see Fig. 4.3 and Fig. 4.4). With higher dispersivity, all nitrate could be attenuated naturally with every seepage water DOC concentration. It is also clear that the model suffers from high numerical dispersion, which is frequently the case for such models due to large-scale and broad model length/thickness ratio. This issue is usual for large-scale models and should be considered in future by using smaller dispersity than the values obtained by the experiments. For this particular aquifer, however the transverse dispersivity was reported to be first centimeters [*Sanchez-León et al.*, 2016] providing complete mixing even without numerical dispersion.

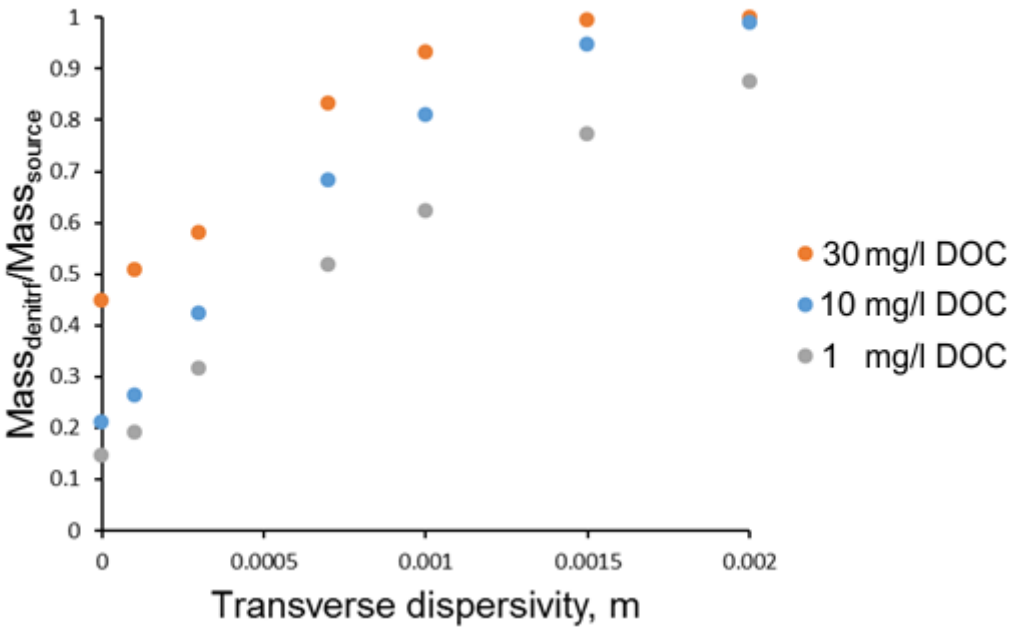

Fig. 4.4. The proportion of total nitrate being attenuated by denitrification versus transverse dispersivity for three different DOC concentrations in the Neckar valley aquifer infiltrating water.

4.4 CONCLUSIONS

For the case studied here, we showed that nitrate in the Neckar sand and gravel aquifer comes to a significant extent from the hillslope including the hillslopes of the neighboring Ammer valley due to the shift of groundwater divide towards the valley. The hillslopes are usually assumed to be more protected to contamination due to large vadose zone [*Aller et al.*, 1987; *Maria*, 2018], which showed to be wrong in the studied landscapes. The hillslopes in both valleys are proved most vulnerable zones in the catchments and sources of contaminates

(e.g. nitrate and sulfate) in the rivers floodplain aquifers. Moreover, the exported plume penetrates the Neckar floodplain from the bottom where it is less protected due to low organic carbon content in the gravel.

In case the Neckar floodplain is not used for agriculture (or protected from nitrate by high organic matter content in the top soil), up to 75% of nitrate would come from the Ammer valley. These results corresponds well with concentration distributions observed by *Schollenberger* [1998]. Denitrification of this nitrate plume is only observed when DOC is provided by seepage water in the Neckar valley and mixed into the gravel body groundwater. Seepage water DOC concentrations and transverse dispersivities in the gravel body control the amount of nitrate consumed and finally the plume length. These parameters should be determined to predict nitrate (and sulfate) transport correctly.

Results of quasi-steady state reactive transport simulations show that zones of different geochemical equilibria exist. The redox zones affect the background geochemistry investigated by *Maier et al.* [2013]. Reactions with oxygen, nitrate, and sulfate change the alkalinity and produce steep vertical redox gradients.

The study underlines the importance of correctly outlined catchment borders and inter-valley flow for water quality management since the nitrate source can only be delineated in case such inter-valley flow is considered.

Nitrate and sulfate contamination has shown to be an issue for such landscapes, but natural attenuation processes can be significant. Nevertheless, a large number of unknown factors such as heterogeneity of geochemical and hydraulic parameters may further influence such systems. Moreover, smaller-scale mechanistic models should be done to explore the importance of such sources of uncertainty more closely.

For this case study, the geographical water divide position is on a hillslope made of oxidized mudstones, which contains excellent fast-transfer zones for oxidized pollutants such as nitrate, increasing the vulnerability of aquifers otherwise protected by organic carbon bearing top loam layers as typical for alluvial flood plains. Nevertheless, it is possible that same landscape is formed in reduced bedrocks. In this case, it is important to study the redox processes in the rock matrix (see chapter 6).

5. REDOX HYDROGEOCHEMISTRY OF AMMER FLOODPLAIN

Although the Ammer floodplain is geologically similar to the Neckar valley, it contains layers with high amounts of organic matter and peat which would reduce agricultural nitrate completely. However, nitrate concentrations in the Ammer river and drainage ditches are still fairly high [*Grathwohl et al.*, 2017]. This can be explained either by direct nitrate input into the or by geogenic production of ammonia by organic matter and subsequent oxidation in the surface drains. These possibilities were investigated in this chapter by reactive transport modelling of Ammer floodplain sediments and surrounding bedrocks.

5.1 INTRODUCTION

Floodplains are common elements in catchments. In temperate climates, they are typically comprised by Pleistocene sands and gravels as well as Holocene peat lenses and loams [*Lang and Nolte*, 1999; *Fuchs et al.*, 2011] and normally considered as hotspots in the biogeochemical cycle due to high organic matter content [*Venterink et al.*, 2003].

The Ammer floodplain is a part of the Ammer catchment located between Pfäffingen and Tübingen. Hillslopes formed of Gipkeuper mudstones confine the floodplain. At the base, it starts with highly conductive base gravel layer, followed by a low-conductive clay layer and a layered system of calcareous sediments and peat. These layers are overlain by alluvium silt and loam. Top sediments are observed to be highly reduced (Fig. 5.1) and the H_2S smell was also observed when coring, indicating sulfate reduction, which is possible only when nitrate and oxygen are already consumed [*Appelo and Postma*, 2005]. The hydraulic connection between the base layer and other layers is still unknown; the general flow direction is along the valley. Relatively high concentrations of nitrate have been observed in the Ammer river (0.5 mmol/l) and drainage channels (0.2 mmol/l). Concentrations of ammonium found in porewater of the floodplain sediments match molality of the nitrate in the ditches (0.2 mmol/l).

Fig. 5.1. Top row: Reduced sediments of the Ammer floodplain, top left – core from the bottom of the drain channel (top left). Bottom row – the walls of the drainage channels after excavation with black reduced loam. Red circles indicate travertine calcite or elemental sulfur precipitation.

The Ammer floodplain contains more organic matter then the Neckar floodplain, which affects the fate of contaminates. A 2-D fully coupled reactive transport model was set up aiming to answer following questions:

1) What is the fate of nitrate when it enters the sediments of the floodplain? Is it reduced in the sediments or finally collected by drainage channels?

2) What is the influence of the spatial distribution or organic carbon within the floodplain sediments on ammonification and denitrification?

3) What is the source of the nitrate observed in the drains? Is it agricultural nitrate or does it come from natural ammonium produced in organic carbon rich layers in the sediments?

4) Are there any other important reactions except the redox reactions affecting nitrate such as sulfate reduction, mineral precipitation, nitrogen gas trapping, etc.?

5.2 FLOW MODEL SETUP

To get a better insight of the typical floodplain geochemistry as well as determine the fate of nitrate and other solutes in the above-discussed flow system, a fully coupled flow and reactive transport model of the Ammer floodplain was developed. It comprises (from bottom to the top): the gypsum-bearing Upper Triassic Gipskeuper mudstones (bedrock), a Pleistocene sand and gravel layer, Holocene organic carbon rich clay and lacustrine calcareous sediments with layers of peat, and alluvial loam on the top (Fig 5.2). Drainage channels, installed for agriculture and the Ammer River serves as the only drain for the floodplain groundwater.

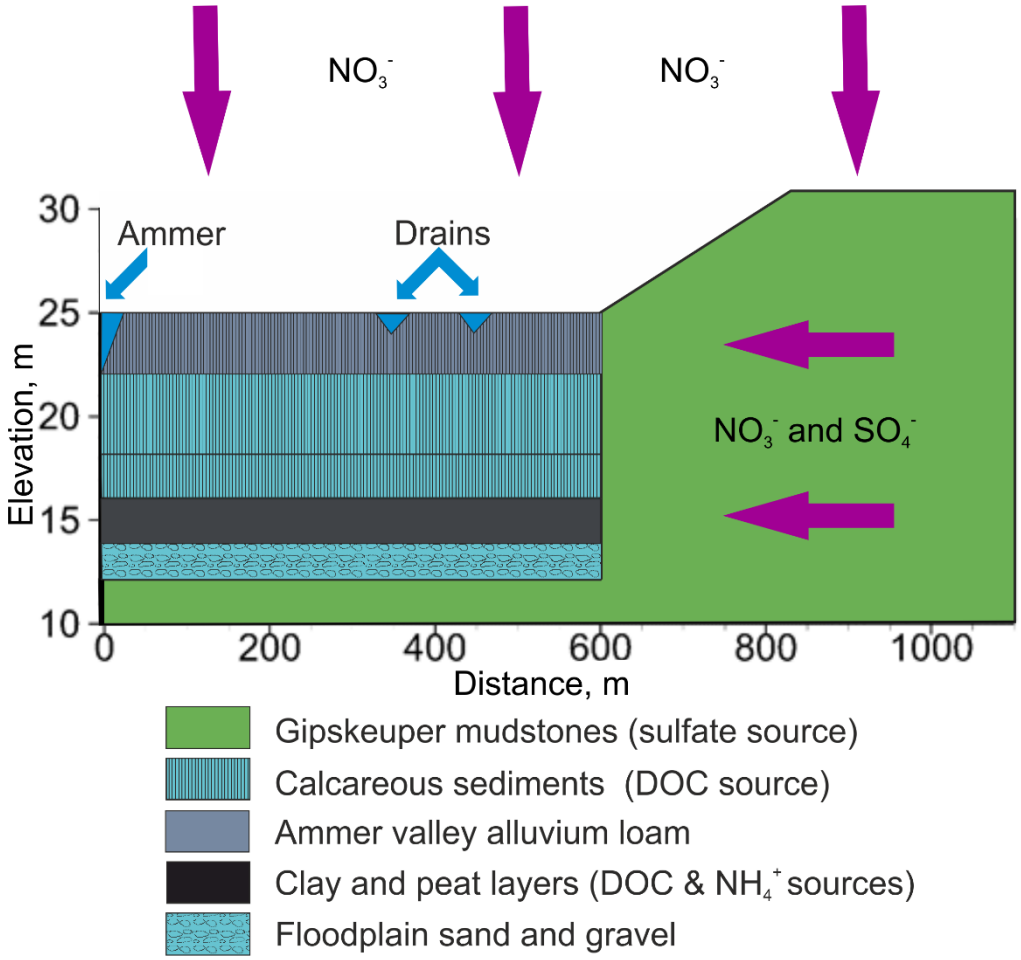

Fig. 5.2.W-E cross-section and conceptual model of the Ammer valley sediments (vertically exaggerated). Nitrate is applied at the top of the model while ammonification happens in the black clay layer.

The numerical model was designed based on the geological settings. Sets of hydraulic parameters were assigned to five homogeneous compartments. Hydraulic parameters were estimated based on grain sizes and observations (Table 5.1). The alluvium loam and gravel layers parameters were adapted from the transport study in the Neckar valley [*Maier et al.*, 2013]. For the Gipskeuper mudstones and calcareous sediments interlayered with peat, effective parameters were adapted from the model specified in **chapter 3** with additional calibration. The geometry of the compartments was adjusted based on information from boreholes used for the construction of a gas pipeline and buildings in the valley.

Table 5.1. Hydraulic parameters assumed for the Ammer, floodplain model.

Stratigraphic unit	Hydraulic conductivity [m/s]	Porosity ϕ [-]	Thickness [m]	Van Genuchten parameters α/N, 1/m
Gipskeuper mudstones	1×10^{-5}	0.03	2-30	4/1.3
Floodplain sand and gravel	1×10^{-3}	0.2	2	35/5.3 [a]
Black clay layer	1×10^{-8}	0.3	3	0.8/1.2
Calcareous sediments	1×10^{-5}	0.4	6	0.8/1.2
Ammer valley alluvium loam	1×10^{-6}	0.3	3	0.8/1.2

[a] [*Maier et al.*, 2013]

The two-dimensional model is 1100 meters long and 36 meters in height. The physical domain was divided into 144 layers and 440 columns resulting in a uniform numerical grid of 25 × 0.25 meters.

On the top of the model, a fixed flow (Neumann) boundary condition was applied. The steady state flow rate (200 mm/year) represents the average annual recharge in the region [*LUBW*, 2011; *Selle et al.*, 2013]. For the Ammer river and the drainage channels, fixed head (Dirichlet) boundaries were used with heads of 22 and 23 meters, respectively. Bottom and the right boundary (water divide) were set impermeable as indicated by the larger scale model presented in chapter 3.

5.3 REACTIVE TRANSPORT MODEL SETUP

The geochemical system used for the reactive transport simulations is shown in Table 5.2 and was generally the same as the one used in the model in chapter 3 with one major exception. Ammonium, which has been reported in the water extracted from the clay layer, was included in the system. Ammonification and nitrification were added as reactive processes as well as organic carbon (SOM with ammonification) in the clay layer which not only releases CH2O (DOC) but also NH_4^+. The ammonification was simplified as irreversible quasi-equilibrium reaction with an equilibrium concentration of NH_4^+ matching the observed data (same way as CH2O release described in chapter 3). The process of nitrification was simulated as an intra-aqueous reaction following the dual Monod kinetics with no inhibition. The reduction of NO_3^- to Ammonium was not considered [*Appelo and Postma*, 2005].

Table 5.2. Geochemical system used in the Ammer floodplain reactive transport model. NH_4^+ and TOC/DOC were adjusted to observed concentrations

Components		
O_2 (aq), CH2O (DOC), Carbonate, pH, Ca^{2+}, SO_4^{2-}, HS^-, NO_3^-, NH_4^+, N_2 (aq)		
Minerals		
Calcite, Gypsum, Organic carbon (SOM), Organic carbon with ammonification		
Carbonate species	**log K_{eq}**	
$H_2CO_3 \rightleftarrows H^+ + HCO_3^-$	-6.36	
$HCO_3^- \rightleftarrows H^+ + CO_3^{2-}$	-10.33	
Gases (in equilibrium with aqueous phase)	**log K_{eq}**	
O_2 (g) $\rightleftarrows O_2$ (aq)	-2.89	
CO_2 (g)+ $H_2O \rightleftarrows H_2CO_3$	-18.2	
H_2S (g) $\rightleftarrows H_2S$ (aq)	-7.99	
N_2 (g) $\rightleftarrows N_2$ (aq)	-3.18	
Solid phase (dissolution/precipitation)	**log K_{eq}**	**k_{eff} [mol/(L·bulk·s)]**
TOC → CH2O	-3.29	1×10^{-6}
TOC → NH_4^+	-2.90	1×10^{-6}
$CaCO_3$ (s) $\rightleftarrows Ca^{2+} + CO_3^{2-}$	-8.48	1×10^{-6}
$CaSO_4$ (s) $\rightleftarrows Ca^{2+} + SO_4^{2-}$	-4.58	1×10^{-6}
Intra-aqueous dual Monod kinetic reactions		
CH2O + O_2 (aq) → CO_2 (aq) + H_2O (For kinetics see Eq. 2.14)	$k_{CH2O\text{-}O2} = 5\times10^{-8}$ mol l^{-1} s^{-1} $K_{1/2O2} = 3.12\times10^{-6}$ *mol* l^{-1} $K_{1/2\ CH2O} = 1\times10^{-4}$ mol l^{-1} $K_{thrO2} = 1\times10^{-10}$ mol l^{-1} $K_{thr\ CH2O} = 1\times10^{-10}$ mol l^{-1}	
CH2O + 4/5NO_3^- + 4/5H^+ → CO_2 (aq) + 2/5N_2 (aq) + 2/5H_2O (For kinetics see Eq. 2.15)	$k_{CH2O\ -NO3-} = 1\times10^{-9}$ mol l^{-1} s^{-1} $K_{1/2NO3-} = 8.06\times10^{-6}$ mol l^{-1} $K_{1/2\ CH2O} = 1\times10^{-4}$ mol l^{-1} $K_{thr\ NO3-} = 1\times10^{-10}$ mol l^{-1} $K_{hr\ CH2O} = 1\times10^{-10}$ mol l^{-1} $K_{inh\ O2} = 6.25\times10^{-6}$ mol l^{-1}	
CH2O +1/2SO_4^{2-} + 1/2H^+ ⇄ CO_2 (aq) + 1/2HS^- (For kinetics see Eq. 2.16)	$k_{CH2O\ -SO4-} = 1\times10^{-10}$ mol l^{-1} s^{-1} $K_{1/2\ SO4-} = 1.6\times10^{-3}$ mol l^{-1} $K_{1/2\ CH2O} = 1\times10^{-4}$ mol l^{-1} $K_{thr\ SO4-} = 1\times10^{-10}$ mol l^{-1} $K_{thr\ CH2O} = 1\times10^{-10}$ mol l^{-1} $K_{inh\ O2} = 3.13\times10^{-5}$ mol l^{-1} $K_{inh\ NO3-} = 1.6\times10^{-5}$ mol l^{-1}	
NH_4^++2O_2 (aq) → NO_3^- + H_2O + 2H^+ (For kinetics see Eq. 2.17)	$k_{NH4+} = 1\times10^{-9}$ mol l^{-1} s^{-1} $K_{1/2O2} = 1\times10^{-5}$ mol l^{-1} $K_{1/2NH4+} = 1\times10^{-5}$ mol l^{-1} $K_{thrO2} = 1\times10^{-6}$ mol l^{-1} $K_{thrNH4+} = 1\times10^{-10}$ mol l^{-1}	

Solid phases were assigned to each compartment as shown in Table 5.3. Again, the presence of carbonate and sulfate-rich stratigraphic units (calcite and gypsum/anhydrite) governs the geochemistry of the model along with the organic-rich layers.

Table 5.3. Initial mineral volume fraction for every compartment of the model. TOC (with ammonification) also releases DOC

Stratigraphic unit	Calcite (vol %)	TOC (vol %)	TOC (with ammonification) (vol %)	Gypsum (vol %)
Gipskeuper mudstones	10	0	0	30
Floodplain sand and gravel	10	0	0	0
Black clay layer	0	0	10	0
Calcareous sediments	90	1	0	0
Ammer valley alluvium loam	0	1	0	0

The initial chemical conditions were assumed to be in equilibrium with the minerals in each layer. Constant (Dirichlet boundary condition) concentration of solutes was used for the rainwater applied at the top boundary as shown in Table 5.4. Other usually significant solutes like Na^+ or K^+ etc. were not considered due to their minor effect on the redox reactions. After reaching steady-state conditions, a NO_3^- concentration of 10 mg/l was applied for the complete top boundary or different intervals along the model (nitrate only in the floodplain or along the whole cross-section).

Table 5.4 Boundary conditions of the transport model resemble the rainwater composition in the area, with redox-conservative species excluded.

Component	Natural rainwater composition (mol/l)
O_2 (aq)	0.00026
DOC	0
CO_3^{2-}	3.95E-04
Ca^{2+}	0.00001
SO_4^{2-}	0.00001
NO_3^-	0

The water divide (left boundary) and the bottom boundaries were again considered impermeable (Cauchy boundary condition), and Ammer river and the drains, in turn, were set as a free exit boundary (Neumann boundary condition).

5.4 RESULTS AND DISCUSSION

The flow paths along with the groundwater water table are shown in Figure 5.3 (top). A significant portion of the water from mudstones goes through the high conductivity gravel layer at the bottom of the floodplain producing a confined aquifer potentially extended along the valley. The flow asymmetry around the drainage channels should be noted. The one that is further from the river has a significantly larger catchment area.

Selected results for reactive transport model presented in Figure 5.3 (bottom) show that neighboring highly reduced and oxidized sediments control the hydrogeochemistry of the system. Oxygen, while present in the bedrock mudstones and gravel layer is entirely reduced once it is in contact with the organic clay layer. Agricultural nitrate is completely contaminates the mudstones. However, the highest NO_3^- concentration is observed in the gravel layer and higher (16 mg/l or 0.25 mmol/l) than the input concentration at the top. Nevertheless, it is also being reduced rapidly once it reaches the reduced sediments. Nitrogen gas (N_2) reaches the drains and the river with a maximum pressure exceeding 1 bar. Ammonium also reaches the drains too and only in contact with sulfate as an electron donor. Redox reactions between these two species are not considered in the present model. However, it can be a point of interest for future research. Sulfate itself also reaches one of the drains but still undergoes reduction on the way through floodplains sediments Calcite precipitates along the flow paths to the drains, adding up to additional 0.5 vol%.

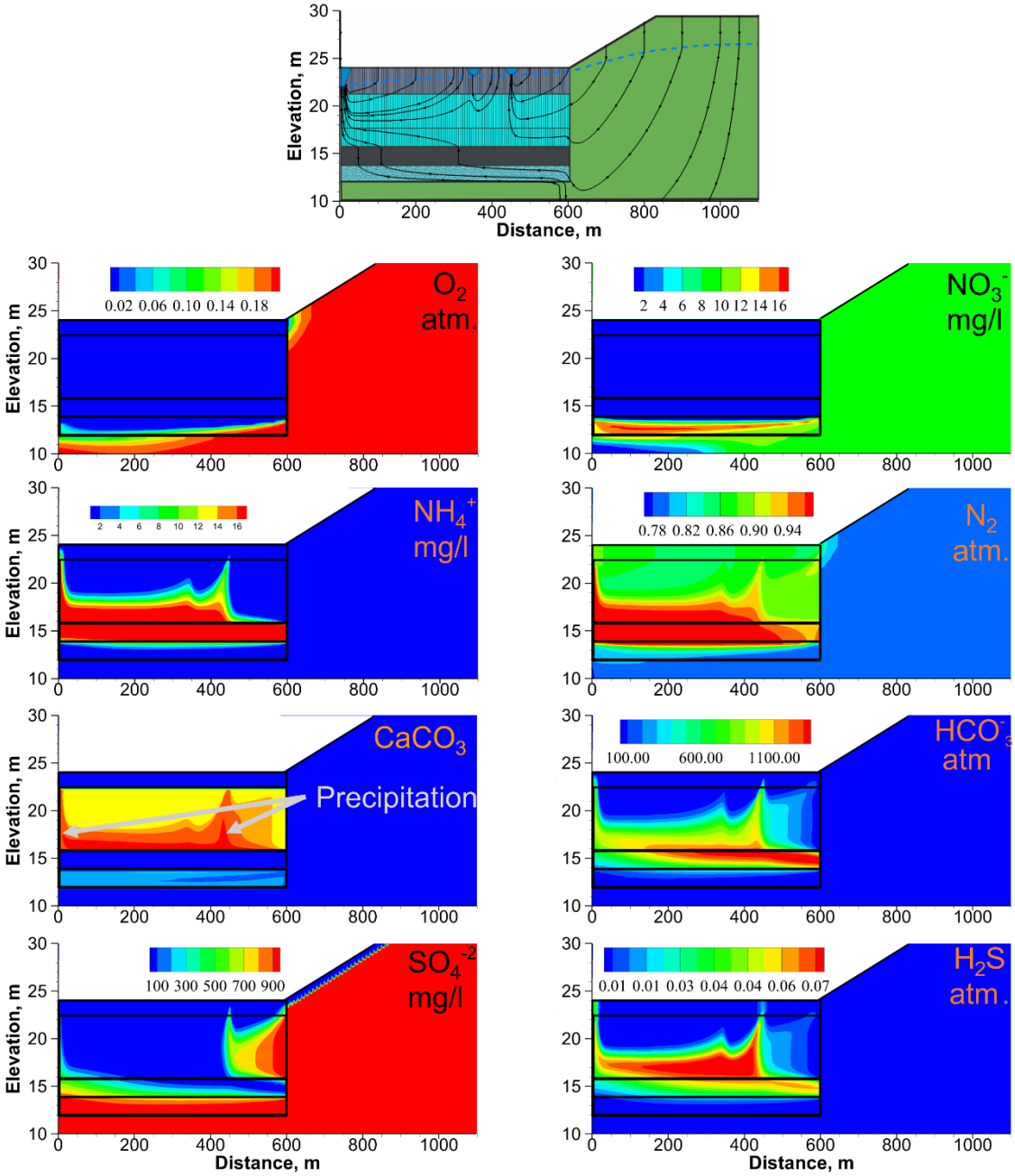

Fig. 5.3. Results for the Ammer, floodplain model. Top: Flow paths and water table; bottom: simulated quasi steady-state spatial distribution of O_2, NO_3^-, NH_4^-, N_2, $CaCO_3$, HCO_3^-, SO_4^{-2} and H_2S along the transect. Electron acceptors are transported along the gravel layer for long distances. Additional nitrate is produced on the boundary between gravel and clay layers, however, is attenuated again in the clay and silt layers. Sulfate reaches the drain closest to the hillslope and partially the river. Calcite precipitates along the flow paths.

5.4.1 REDOX ZONATION AND STEEP REDOX GRADIENTS

Steep redox gradients cause sharp transitions from electron acceptors-rich sediments (bedrock mudstones) to electron donor-rich sediments (floodplain). This transition controls the hydrogeochemistry of the whole floodplain and affects reactive transport through it. Mixing under such conditions is only significant in the gravel and sand layer where mixing allows more nitrate to be generated by ammonia, while in the calcareous sediments the supply

of reagents is regulated by the flux of the electron acceptors and the release of electron donors from sediments.

5.4.2 Possible sources of nitrate in Ammer river and drainage channels

The high concentration of nitrate below the clay layer might be explained by the ammonium production. Mixing with oxic water (the only area where mixing plays an important role) leads to nitrate production. Thus, geogenic NH_4^+ is the additional source of the nitrate in the gravel layer. In contrast, agricultural nitrate is completely attenuated in the reduced parts of the alluvial loam in the floodplain. Thus, agricultural nitrate does not reach the drains and the river. The only option for NO_3^- and O_2 to propagate into the floodplain is after the reduction potential is exhausted at least in some parts of the sediments. This is possible in the presence of the preferred water paths whose existence are unknown. Thus, the nitrate in the drains is predicted to be geogenic: ammonia discharges into the drains and oxidized in the surface water bodies.

5.4.3 Potential conductivity changes due to self-cementation of the Ammer floodplain sediments and degassing

The dissolution of the gypsum from the bedrock produces high concentrations of calcium and sulfate. While the later one mostly is reduced during transport, the former one is not affected by redox reactions directly. On the other hand, sulfate reduction, denitrification and oxygen reduction all produce CO_2 and consume hydrogen ions. Moreover, these processes tend to happen in areas of high flow - thus transport of calcium from the bedrock leads to calcite precipitation. Since the quarternary sediments contain calcareous tuff layers additional calcite precipitation is hard to distinguish, but this would decrease the pore space and thus hydraulic conductivity. Calcite concretions and aggregates of different sizes (up to 1 cm) were observed in drilling cores.

Another process impacting flow is degassing. Nitrogen gas pressure reaches one bar, which is still lower than the expected water pressure below the river. However, more gas release and increased fertilization (higher concentration of NO_3^-) can lead to increasing total gas pressure and finally degasification happens. The bubbles of unknown gas have been observed in the draining ditches. Degassing would restrict water flow and could be accounted for in the long-term.

5.5 CONCLUSIONS

A two-dimensional reactive transport simulation of solutes in the Ammer river floodplain was performed to get an insight into biogeochemical changes and to determine the potential to attenuate nitrate and sulphate. Expected redox gradients in the system are generally steep and controlled by the contrasting mineral composition of the bedrock and floodplain sediments. The high amount and homogeneous distribution of the total organic carbon in the floodplain calcareous sediments make the various flow scenarios (e.g., flow heterogeneity) relatively unimportant for reactive transport since the residence times in the floodplain are high enough for complete denitrification. Nitrate is transported through the Gipskeuper mudstones over long distances. However, it is reduced rapidly in the Ammer floodplain sediments and has no chance to reach any surface drain. Mixing does not play any significant role in the contaminates fate due to all redox reactions occur in areas with notable elector donors release (e.g., in situ). Sulfate propagates further then nitrate and reaches partially some of the drains. In absence of oxygen and nitrate, part of it is oxidized which explains the observed H_2S smell near the surface drains. The gravel base layer acts as a confined aquifer and allows fast transport of contaminants as well as a reactor for electron donors from the black clay layer and electron acceptors from the mudstones. The travel time between this aquifer and the river can vary and probably decreases along the river hence increasing the possibility for nitrate to pass through.

Geogenic production of ammonium in high organic layers and peat likely is a major source of nitrate in the river and the ditches. This does correspond to nitrate concentrations observed in the drains.

As a final point, high pressures of N_2 are observed in the model along with precipitation of calcite on the flow paths. These processes can affect the flow field in larger timescales and should be studied further.

Nitrate and other contaminants, which are degraded under reducing conditions, are readily reduced in floodplain sediments because of the high organic carbon and this decreases the vulnerability of the floodplain water for nitrate contamination in opposite to the hillslopes confining the floodplains.

6. LONG TERM REDOX EVOLUTION OF GROUNDWATER AND NITRATE TRANSPORT IN A FRACTURED LIMESTONE AQUIFER

Hard rocks including igneous, metamorphic, cemented sedimentary and carbonate rocks occupy more than half of the Earth surface. The permeability of such rock formations depends on fractures and therefore they are broadly grouped under the term fractured rocks [*Singhal and Gupta*, 2010]. Carbonate rocks in particular occupy about 12% of the surface worldwide and 35% in Europe [*Bakalowicz*, 2005; *Vías et al.*, 2006]. Accordingly, about 25% of the global population depends on groundwater supply from carbonates, with some countries hitting 50% [*Chen et al.*, 2017]. In the same time 42% of land surface is being used for agriculture purposes in Europe and 57% in Germany in particular [*European Enviromental Agency*, 2017].

While many studies have been done to understand flow and transport in fractured media (see Chapter 1), behaviour of agriculture pollutants in the carbonate aquifers is relatively poorly understood as well as a natural redox evolution of such aquifers, especially on the catchment scale [*Grathwohl et al.*, 2017]. In this part of the thesis, the fate of agricultural nitrate in the fractured Upper Muschelkalk limestone aquifer is explored. While field observations propose strong reduction potentials in the aquifer, the particular pathways of oxygen and nitrate reduction are not clear, since all of the electron donors are immobilised in the rock matrix, where reaction rates are slow due to matrix diffusion or do not occur at all due to absence of biota. In this section various sources for dissolved Fe^{2+}, which can diffuse into the fractures, are discussed and tested in reactive transport models.

6.1 INTRODUCTION

Fully coupled discrete fracture network flow and reactive transport modeling are computationally demanding, and thus a fractured limestone aquifer (Upper Muschelkalk) was conceptualized as a sequence of connected fractures (and karst features), and then a single fracture-matrix model was applied at catchment scale in this study. Moreover, nitrate transport was implemented to study the different possible mechanism and paths of denitrifications.

Water chemistry observations in the Upper Muschelkalk aquifer [*Grathwohl et al.*, 2017] show depletion of the oxygen already at groundwater ages of 3-5 years and incomplete depletion of the nitrates in 20-25 years. The presence of pyrite and siderite along with organic carbon in the limestone matrix (**Appendix I**) suggest high reduction capacity of the aquifer. However, 80 percent of the pores are observed to be around 100 nm and less [*Rügner et al.*,

1999], which is suggested to prohibit microbial growth [*Rivett et al.*, 2008]. Rock samples (Fig. 6.1) display iron hydroxide coatings only on fracture surfaces indicating dissolution and oxidation of iron (and absence of this oxidation in the rock matrix) indicating absence of Fe^{2+} oxidation in the rock matrix.

Therefore, a reactive transport model was developed to simulate long-term redox evolution in the Upper Muschelkalk aquifer including nitrate pollution and attenuation in the last 100 years. Different geochemical scenarios were tested aiming to answer following questions:

1. What parameters and processes affect the long-term redox evolution and nitrate transport in the limestone fracture aquifer? Is the system diffusion or kinetics controlled?
2. Is it possible to provide sufficient reduction potential in the fractures when microbial growth in the matrix is suppressed? Should a sequence of abiotic and biotic steps have to be considered in pyrite oxidation by oxygen in the matrix and ferric iron oxidation after diffusive transport in the fracture or should there be considered other sources of electron donors, e.g. pyrite crystals on the fracture walls or siderite content in the matrix?

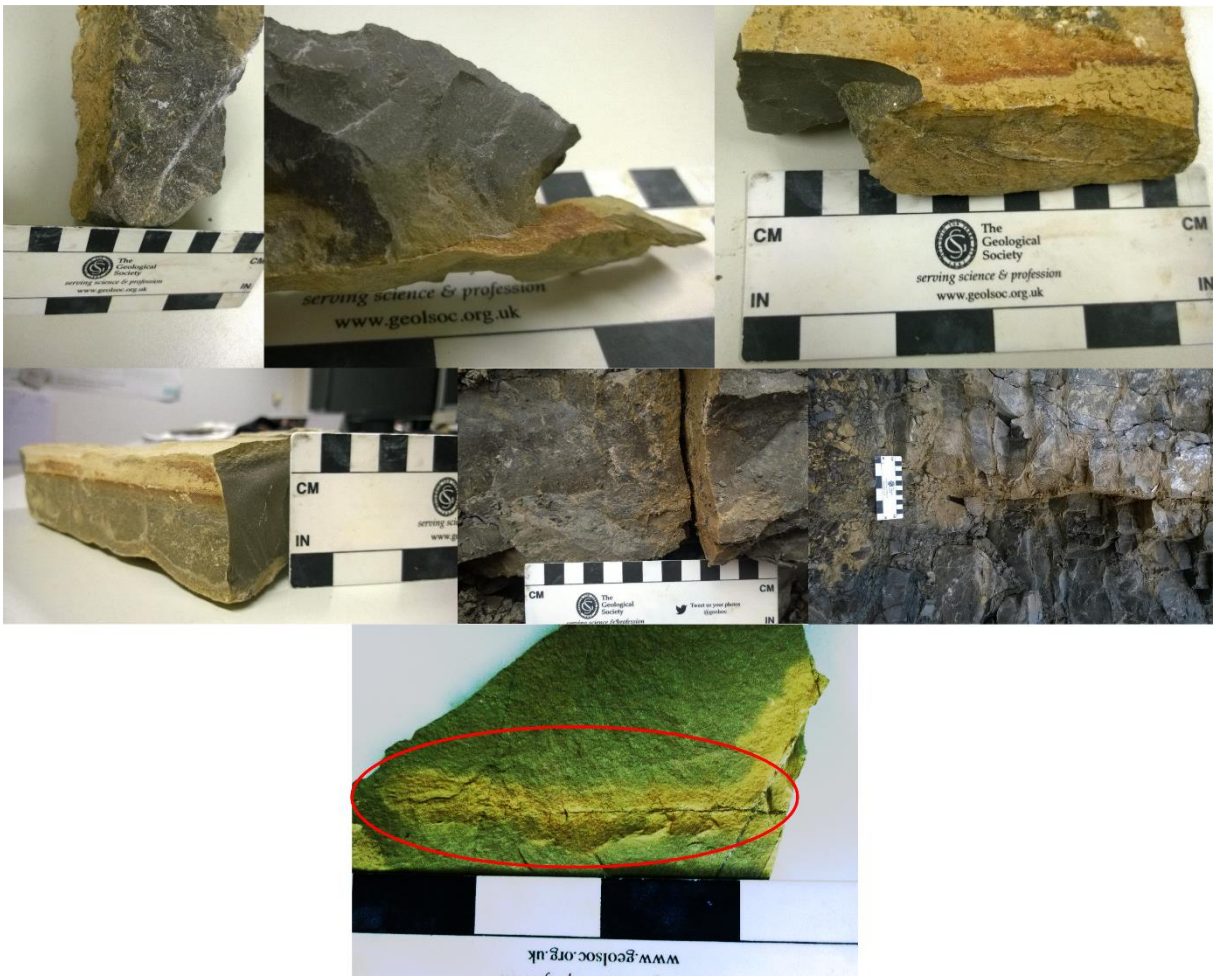

Fig. 6.1. Samples of rock oxidation: Upper Muschelkalk samples. Oxidation is only visible on fracture surfaces. No visible oxidation zones in the rock matrix (top). Example of clearly visible oxidation of the rock matrix proximal to the fracture in Lettenkeuper limestones (bottom).

6.2 CONCEPTUAL MODEL

The Upper Muschelkalk is characterized as a fractured and karstified aquifer. Thus, flow conditions are incredibly complex and to a large extent unknown. Therefore simplified 2-D models were setup to study different scenarios of solute transport in the aquifer based on following assumptions:

1) Hydrologically the aquifer can be split into permeable fractures (or karst features), and impermeable limestone blocks (matrix). Most of the flow happens through preferential flow paths in fractures with advection being the major transport mechanism. The flow in blocks is very slow and can be neglected. Thus reactions in the rock matrix solute depend on slow diffusion;

2) A water parcel passes through several discrete connected fractures and karst features on the way between recharge and discharge zones;

3) The direction of the flow can be vertical, horizontal at any given point following the fracture direction and depend on the local hydraulic gradient;

4) The groundwater age (the time that the parcel spends in the aquifer) of any given water parcel is controlled by flow velocity in these fractures, and local velocity is controlled by the aperture of any single fracture and hydraulic gradient;

5) The limestone mineral composition is homogeneous and isotropic (e.g., we assume that whole aquifer consists of one geological facies). Geochemically it is not essential in which exact fracture the water parcel resides.

6) Any real three-dimensional flow path then can be represented by one-dimensional streamline. Following this streamline, the water parcel will undergo diffusional exchange with the carbonate block across the fracture surface. Solutes can react with minerals in the matrix, minerals exposed on the fracture surface wall or with other dissolved species in the fracture. Consequently, reactive transport may be simulated using a two-plate fracture model in a semi-exposure time way using an average flow velocity in the fracture.

The conceptual model thus is two-dimensional and considers advective-dispersive transport of solutes in the single fracture. The solutes are allowed to interact with the rock matrix only via molecular diffusion. For some scenarios, redox reactions between different sets of electron donors and acceptors are permitted in the matrix and the fracture; for other scenarios, these reactions are only allowed in the fracture (see Section 6.4). The model considers only half fracture and half block due to the symmetry of the system. In all cases, the flow is steady state and fixed along the fracture under fully water saturated conditions.

In the Upper Muschelkalk aquifer, as in any fracured limestone aquifer, it is impossible to delineate the exact pathway that a sampled water parcel takes due to the complexity of the flow network. To allow comparison of model results with the sampled data, the model considers the water residence time in the fracture as a proxy of distance. Residence time represents the time the parcel was exposed to the fracture wall along its streamline, and thus it controls diffusion exchange between fracture and the matrix. Thus, the chemistry of a water parcel in the fracture is controlled by the time the water parcel spent in the fracture.

Mathematically, however, the set of equations was not changed, and the usual advective-dispersive equation (see Eq. 2.5) was being solved, with the distance and average flow velocity in the fracture fitted to match residence time of interest.

For a chemically homogeneous aquifer the model can predict the water chemistry of every given water parcel knowing only its age. There is no need to know exact water flow paths through the aquifer and only one model run is needed for every scenario to predict

solute distributions in the whole aquifer. However, to simulate reactive solute transport in the chemically heterogeneous aquifer (e.g. every layer of the limestone bears different secondary minerals) the model approach should be developed further.

The concentration profiles in fracture and matrix in this case only depend on the travel time along the fracture (exposure time) and not on the distance (although the distance, of course, controls the travel time in reality along with the velocity: $t = d/v$). The travel time along the fracture represents distance along the fracture (streamline) in the conceptual model (Fig. 6.2). For a reference: for an average flow velocity of the water in the fracture of 1 km/year, the resident time scale would correspond to a length scale of kilometers.

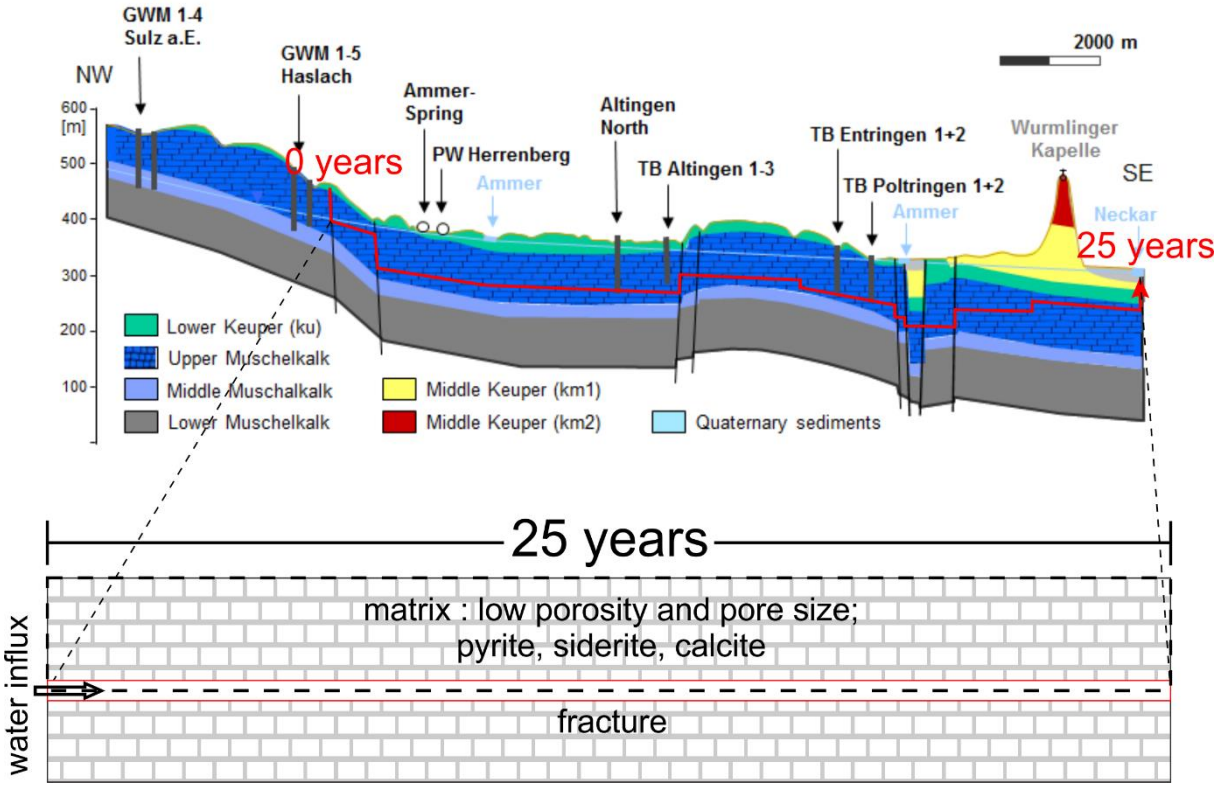

Fig. 6.2. Schematic representation of a streamline through the Muschelkalk formation (top) and conceptual model used for catchment scale transport simulation in a fractured aquifer. The same model can represent the streamline of any given length as long as the travel time is equal. Moreover, one model run can represent every single streamline shorter (in time) then the model. The cross-section through the Ammer valley is adapted by K. Ostenbruck after *Villinger* [1982].

The model simulates the evolution in redox conditions in the aquifer since the last ice age and how nitrate input in the last 100 years changed the system. Thus, the running time of the model is 10100 years in total with the first 10000 years of oxic recharge followed by nitrate addition in the last 100 years. Calcite is the most abundant mineral in the fracture and pyrite is considered as primary electron donor mineral [*Grathwohl et al.*, 2017]; additionally, in some

scenarios, siderite was included since this provided a source for ferrous iron in the rock matrix required by model for reduction of nitrate.

6.3 FLOW AND REACTIVE TRANSPORT MODELS SETUP

The numerical flow and transport models were set up using the MIN3P code [*Mayer*, 2002] all comprising two compartments: "fracture" and “matrix.” The hydraulic conductivity k of the fracture compartment was set to 1 m/s, while the conductivity of the matrix compartment was very low (10^{-14} m/s) leading to negligible flow. The physical domain of the simulated fracture is 10 m long and 0.001 m thick. The matrix block is 0.999 m thick, which makes the whole model one meter thick in total. The numerical mesh grid consists of 200 rows and 28 layers. It is uniform in lateral (fracture) direction (every cell is 0.05 m long). In the vertical (block) direction mesh is nonuniform, and cells thicknesses grow from 0.001 to 0.1 m (there are four layers from the thickness 0.001 m to 0.005 m, five layers from 0.005 m to 0.01 m, nine layers from 0.01 m to 0.1 m and nine layers from 0.1 m to 1.0 m, see Fig. 6.3).

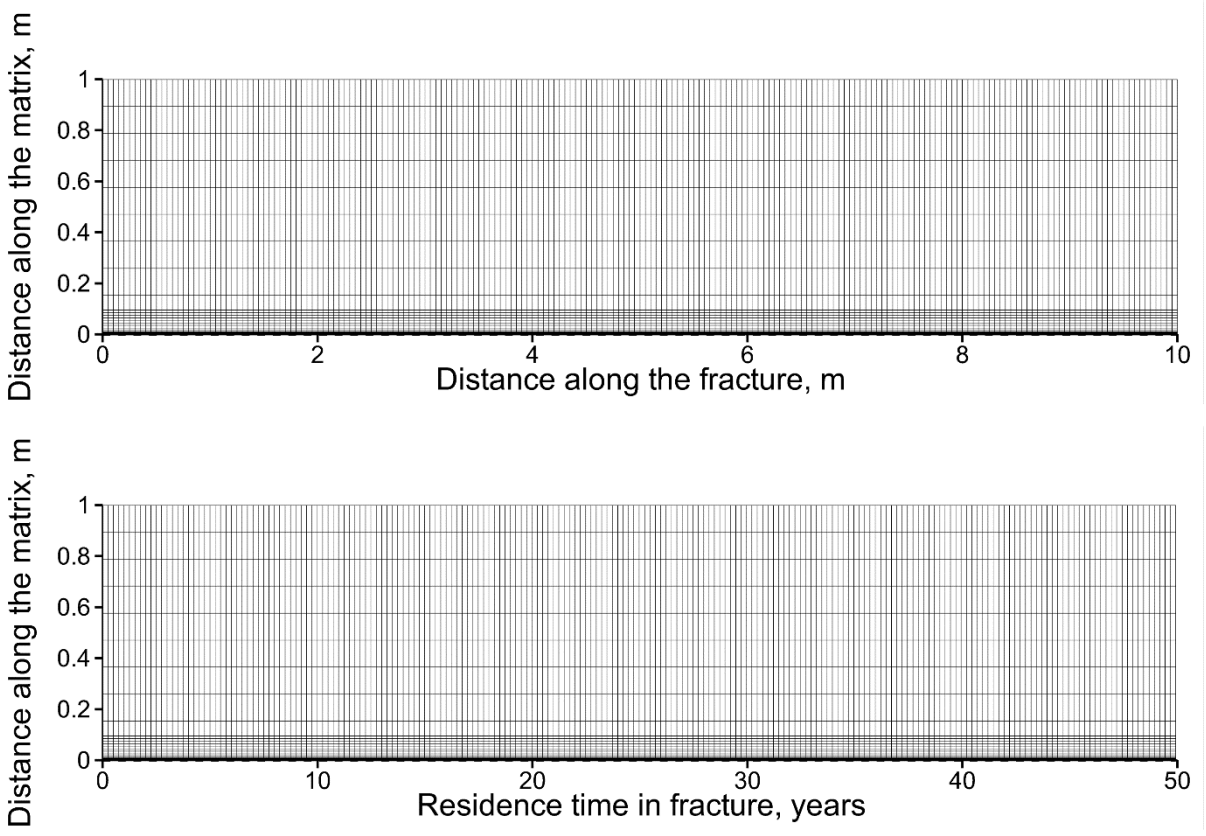

Fig. 6.3 The mesh used for simulations (top) and its representation in the residence time domain when the average velocity in the fracture is 0.25 m/year

The specified flux (Neumann) boundary condition is applied to the left side of the fracture layer with a rate of 1.27×10^{-08} m/s, and fixed hydraulic head (1.002 m) (Dirichlet boundary) was used at the right side of the model to establish steady state flow along the

fracture. Thus, 50 years residence time of water in the total fracture was achieved. In this set up the flow velocity represents the average flow velocity along the flow path which includes the effect of the local hydraulic gradients and heterogeneity in the fracture aperture.

The velocity field produced by the flow model was used in reactive transport simulations to solve the advective-dispersive equation. The parameters ranges assigned to the compartments in different scenarios are summarised in section Table 6.2.

To identify the controlling factors in nitrate reactive transport, the hydrogeochemical model considers the most relevant redox-sensitive species in the aquifer: dissolved oxygen, nitrate, sulfate, pyrite, ferrous iron as well as the carbonate system with dominant reactive mineral phases (siderite, calcite). The geochemical components and reactions considered are shown in Table 6.1.

For dissolution/precipitation of calcite, siderite, ferrihydrite, and goethite, constant reaction rates were assumed. Equilibrium constants and reaction rates for these components are based on the recommended values [*Ball and Nordstrom*, 1991]. Ferrihydrite and goethite represent here the products of Fe^{2+} oxidation by oxygen and nitrate accordingly, which was modeled directly without a Fe^{3+} stage. Moreover, for some scenarios, these reactions were not allowed inside the matrix. Goethite precipitation was inhibited under oxic conditions. The shrinking core model [*Mayer*, 2002] was used for pyrite oxidation kinetics by both, oxygen and nitrate. Pyrite oxidation by nitrate was addressed only in a few scenarios. Parameters for this model such as effective pyrite aggregate radius, particle diffusion coefficient, and reaction rate are unknown, and thus sensitivity for pyrite oxidation kinetics was tested and proved to be not sensitive compared to the low effective matrix diffusion coefficient. The same parameters as in earlier studies were used [*Bao et al.*, 2017] [*Langman et al.*, 2014]. The initial chemical conditions were calculated to be in equilibrium with the minerals in each cell; solutes like Na^+ or K^+ were not considered because of their minor effect on the redox reactions. Constant concentration was used for the left flow boundary to represent the recharge water (**chapter 5**). After first 10000 years, nitrate was applied for 100 years to simulate the start fertilization in agriculture. The concentration of 0.0008 mol/l (50 mg/l) was chosen, which is a threshold nitrate concentration for drinking water in Germany. The right boundary allowed free exit (Neumann boundary condition). The diffusion coefficient in water D_{aq} was set 1.5×10^{-9} m/s in all scenarios for all mobile species.

Table 6.1. An overview of the geochemical system considered for the fracture-matrix reactive transport model; some reactions were allowed only in parts of the physical domain

Components		
O_2 (aq), Carbonate, pH, Ca^{2+}, Fe^{2+}, SO_4^{2-}, NO_3^-, N_2 (aq), Conservative tracer		
Minerals		
Calcite, Pyrite, Siderite, Ferrihydrite, Goethite		
Carbonate species	**log K_{eq}**	
$H_2CO_3 \rightleftarrows H^+ + HCO_3^-$	-6.36	
$HCO_3^- \rightleftarrows H^+ + CO_3^{2-}$	-10.33	
Gases (in equilibrium with aqueous phase)	**log K_{eq}**	
O_2 (g) $\rightleftarrows$ O_2 (aq)	-2.89	
CO_2 (g)+ $H_2O \rightleftarrows H_2CO_3$	-18.2	
N_2 (g) $\rightleftarrows$ N_2 (aq)	-3.18	
Solid phase (dissolution/precipitation)	**log K_{eq}**	***keff* [mol/(L·bulk·s)]**
$CaCO_3$ (s) $\rightleftarrows Ca^{2+} + CO_3^{2-}$	-8.48	1×10^{-6}
$FeCO_3$ (s) $\rightleftarrows Fe^{2+} + CO_3^{2-}$	-10.45	1×10^{-9}
$4Fe(OH)_3$ (s) + $8H^+ \rightleftarrows 4Fe^{2+} + O_2$(aq)+ $10H_2O$	4.37	1×10^{-6}
$10FeOOH$ (s) + N_2(aq) + $18H^+ \rightleftarrows 10Fe^{2+} + 2NO_3^-$+ $14H_2O$*	4.37	1×10^{-6}
Pyrite oxidation by O_2 and NO_3^-		
FeS_2 (s) + $3.5O_2$(aq)+ $H_2O \rightleftarrows Fe^{2+} + 2SO_4^{2-} + 2H^+$ (For kinetics see Eq. 2.18)	S_{py}= 1×10^{-6} mol l^{-1} s^{-1} r_{py}^r = 50µm, r_{py}^r = 49 µm $D_{py,O2}$ = 2.41×10^{-9} m^2 s^{-1}	
$5FeS_2$ (s) + $14NO_3^-$ + $4H^+ \rightleftarrows 7N_2 + 5Fe^{2+} + 10SO_4^{2-}$ + $2H_2O$* (For kinetics see Eq. 2.19)	S_{py}= 1×10^{-6} mol l^{-1} s^{-1} r_{py}^r = 50µm, r_{py}^r = 49 µm $D_{py,NO3}$ = 2.41×10^{-9} m^2 s^{-1}	

*Inhibited in the presence of oxygen.

6.4 TESTED SCENARIOS

A porosity of about 0.01 with more than 90% of pores being smaller than 100 nm was reported for Upper Muschelkalk limestones [*Rügner et al.*, 1999]. Biologically mediated reactions are considered impossible when pore size becomes less than 1 µm [*Rivett et al.*, 2008]. These limestones have an organic content of 0.08 vol% and the pyrite content is 1 % mass or less [*Grathwohl et al.*, 2017]. However, local mineral composition and pore size distribution can differ from these values. Organic matter is assumed as conservative (kerogen). To elucidate the relevant transformation and storage processes which affect nitrate transport in the aquifer five base scenarios were developed. They allow to evaluate

assumptions such as microbially mediated reactions in the matrix or importance of the presence of various electron donors in the limestone matrix or on the fracture wall. (Table 6.2)

Table 6.2. Parameters ranges and processes considered for different scenarios

Scenario №	***1***	***2***	***2.1***	***2.2***	***3***	***3.1***	***4***	***4.1***	***5***	***5.1***	***5.2***
Pyrite oxidation by O_2 in the matrix	yes	yes	yes	yes	no	no	yes	yes	yes	no	yes
Pyrite oxidation by NO_3^- in matrix	yes	no	no	no	no	no	no	no	no	no	no
Pyrite concentration in matrix, vol%	10^{-4}	10^{-4}	10^{-4}	10^{-4}	0	0	10^{-4}	10^{-4}	10^{-4}	10^{-4}	10^{-4}
Fe^{2+} oxidation in matrix	yes	yes	yes	yes	no	yes	yes	yes	yes	yes	yes
Matrix porosity ϕ -	0.01	0.01	0.01-0.3	0.01	0.01	0.01	0.01	0.01	0.01	0.01	0.01
Quasi-equilibrium pyrite oxidation	no	no	no	yes	no	no	no	no	no	no	no
Siderite concentration in matrix, vol%	0	0	0	0	10^{-3}	10^{-3}	10^{-3}	10^{-4}	0	0	10^{-3}
Pyrite concentration on fracture surface, vol%	0	0	0	0	0	0	0	0	5×10^{-3}	5×10^{-3}	5×10^{-3}

Fig. 6.4 illustrates scenario 1 (basic scenatio) with redox reactions matrix and in the fracture to represent the situation where microbes are not excluded by small pore sizes; pyrite here is the only electron donor in the matrix. The electron acceptors in the water propagate through the fracture and diffuse into the rock matrix. In the matrix the usual redox zonation is formed: first a zone which is depleted by electron donors, then a zone where oxygen is being reduced by pyrite and finally a zone where nitrate is being reduced also by pyrite. After both electron donors are exhausted, the matrix remains unchanged.

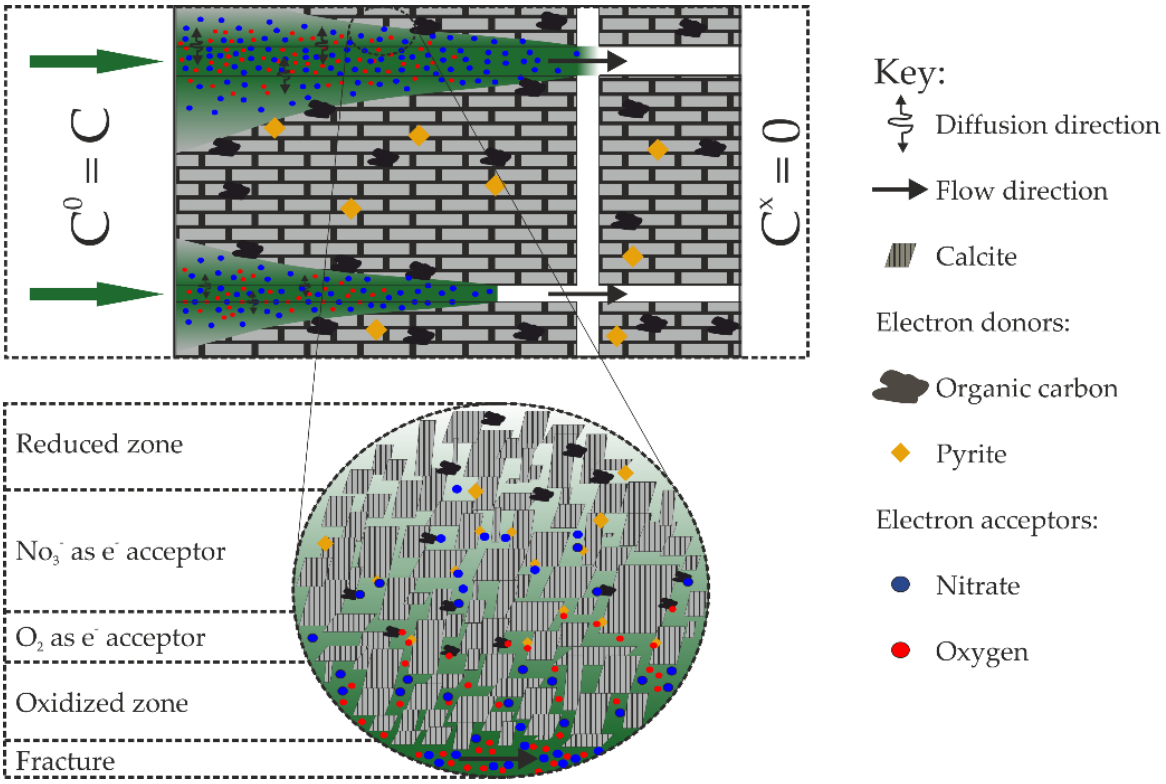

Fig. 6.4. Fracture- and pore-scale conceptual model for scenario 1. Pyrite oxidation in the matrix is allowed by both, oxygen and nitrate. The "usual" redox sequence forms as well as a reactive diffusion front.

In scenario 2 (stepwise pyrite oxydation scenatio) (Fig. 6.5) microbes are not allowed in the matrix and redox reactions in the matrix are restricted to pyrite oxidation only by oxygen. The electron acceptors propagate through the fracture and diffuses in the matrix along it in the same way as in the previous scenario. The difference, however, is that only oxygen is allowed to react with pyrite in the matrix, and nitrate behaves now in the matrix as a conservative solute. Moreover, oxygen is only allowed to oxidise the sulphur in pyrite, and Fe^{2+} can diffuse towards the fracture where oxidation (by both, O_2 and NO_3^-) and precipitation of iron hydroxides occurs. This scenario tests the hypothesis that due to non-biological oxidation of pyrite, enough Fe^{2+} can diffuse and accumulate in the fracture to attenuate nitrate transport. Scenarios 2.1 and 2.2 test the importance of the porosity and reaction rate in this system since these values control Fe^{2+} release. Two additional matrix porosities (0.05 and 0.3) and an instantaneous equilibrium pyrite oxidation reaction were tested. Pyrite is again the only electron donor in the matrix.

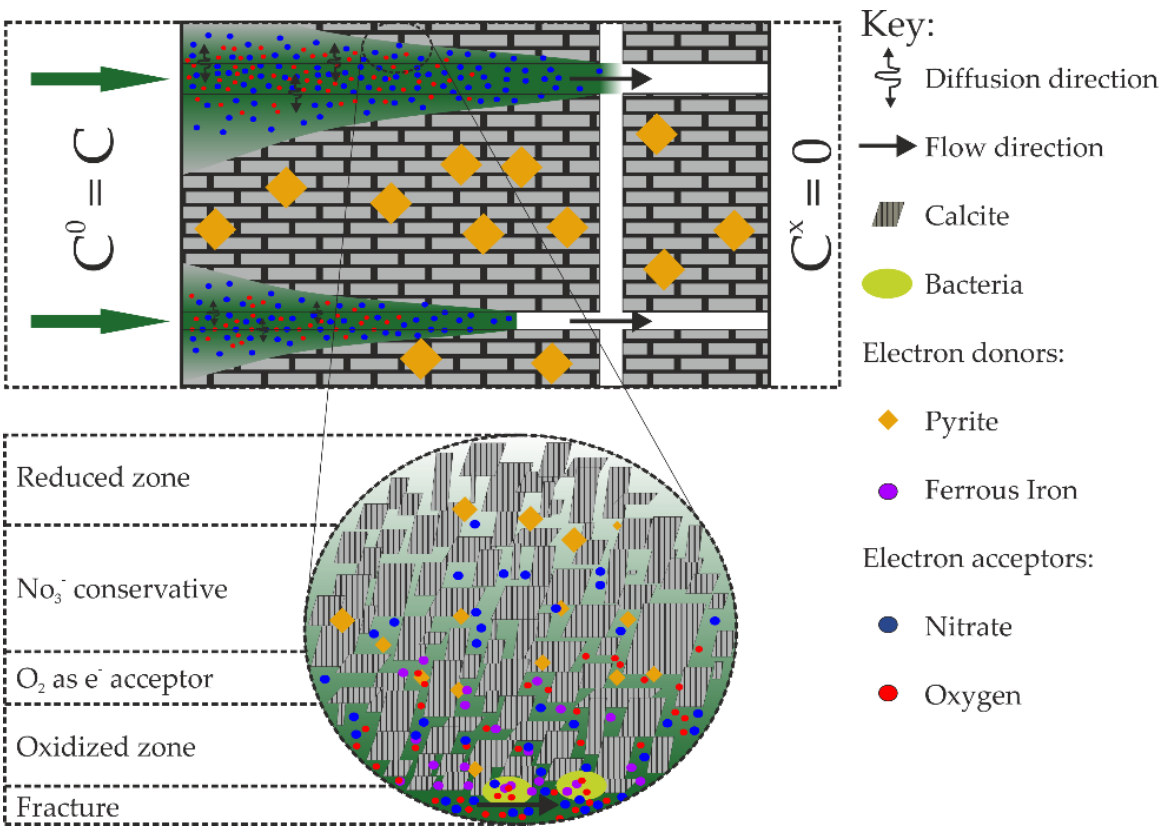

Fig. 6.5. Fracture- and pore-scale conceptual model for scenario 2. The pyrite is only allowed to be consumed by oxygen, while nitrate propagation is only controlled by diffusion. Fe^{2+} diffuse in the fracture from the matrix.

In scenario 3 (siderite scenario) there is no pyrite in the matrix, however a small fraction (0.01 vol%) of siderite is present. This scenatio shows how siderite dissolution at the fracture surface affects redox-sensitive solute transport due to release of Fe^{2+}. In a base scenario, all redox reactions are turned off in the matrix and are only allowed in the fracture. In scenario 3.1 Fe^{2+} oxidation in the matrix is allowed by both oxygen and nitrate.

In scenario 4 (pyrite+siderite scenario), both pyrite and siderite are present in the matrix. Abiotic Pyrite oxidation by oxygen in the matrix was allowed which increases siderite solubility due to the acidification caused by pyrite oxidation. Scenario 4.1 tests the model sensitivity for siderite concentrations.

In scenario 5 (pyrite on the fracture wall scenario), 0.005 vol% of pyrite was added to the fracture to represent pyrite crystals at fracture surfaces. In the base case scenario, pyrite in fracture and matrix is the only electron donor. In scenario 5.1 only pyrite in the fracture was used as an electron donor, and in scenario 5.2 pyrite is present only in the fracture while siderite is present in the matrix. This scenario tests the importance of pyrite in the fracture for oxygen and nitrate reactive transport and how this affects the breakthrough of both solutes at the end of the fracture.

6.5 RESULTS

6.5.1 SCENARIO 1

Fig. 6.6 shows how in ten thousand years oxygen propagates in the fracture and how a wedge-shaped oxidation zone forms in the matrix. Reactions clearly affect O_2 transport compared to the conservative tracer (Fig. 6.6d) in fracture and matrix. Concentrations of dissolved oxygen up to 5×10^{-3} mmol/l propagate approximately 5 years along the fracture after 10 000 years – all water older is practically oxygen free. Moreover, oxygen concentrations appear to be quasi-steady state after about 9000 years because oxygen reaction rates in the matrix are almost equal to the oxygen diffusion influx rates (Fig. 6.7). The O_2 front has only migrated a maximum distance of 2 cm into the rock matrix at the beginning of the fracture. Most of the oxygen gets consumed by pyrite oxidation (93 %) while 7% is consumed by oxidation of other species of ferrous iron.

After fertilization started, nitrate rapidly progresses through the oxic zone and then slows down, finally an anoxic oxidation zone in the limestone block develops. In 100 years nitrate propagates 6 years along the streamline and maximum of 3 cm in the matrix (Fig. 6.6c) before it is reduced. Thus clear oxic and anoxic zones develop along the streamline.

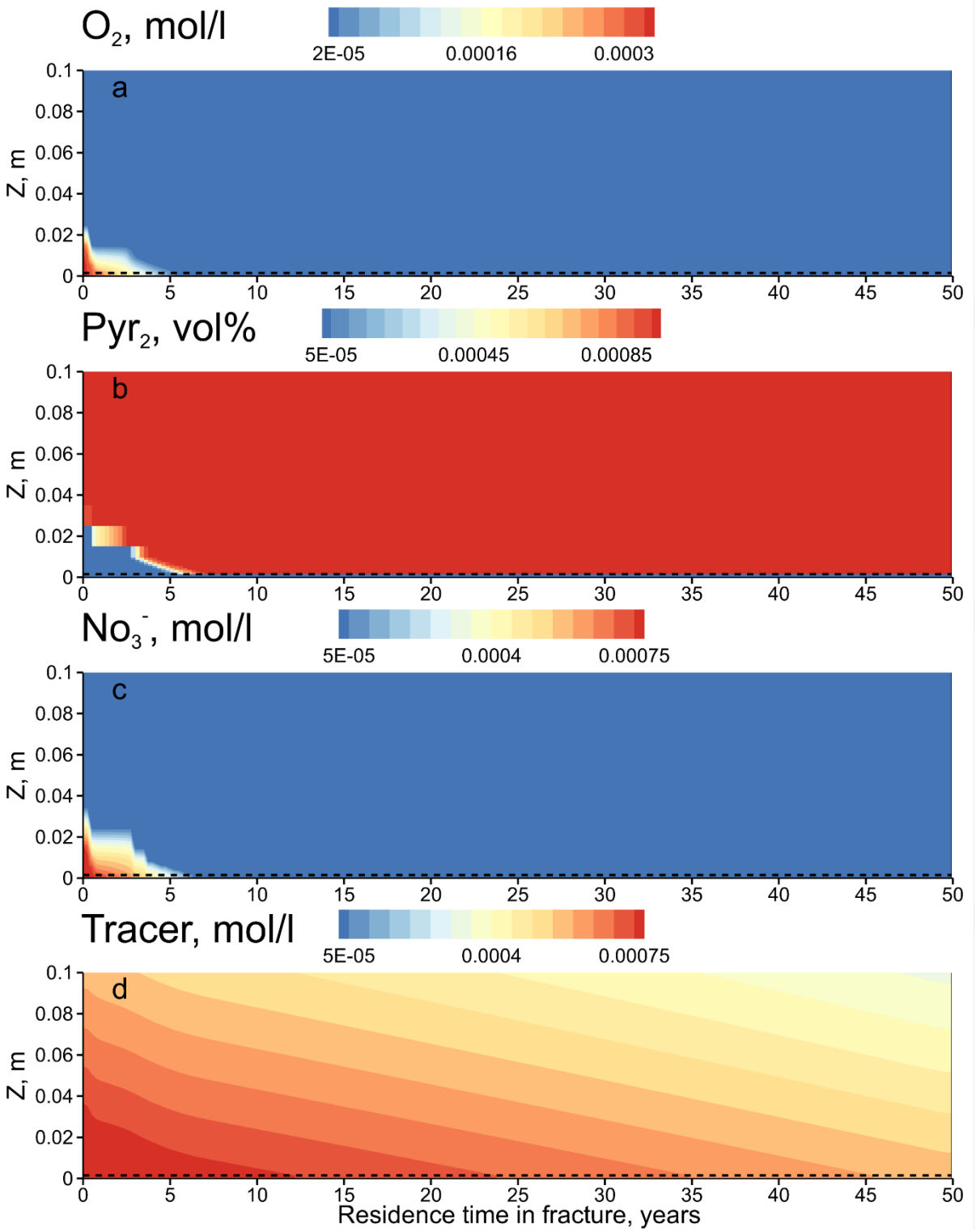

Fig. 6.6. Selected simulation results for scenario 1 (pyrite oxidation in the rock matrix) after 10000 years: a) O_2 distribution in matrix and fracture, b) FeS_2 distribution in the matrix, c) NO_3^- distribution in the matrix and fracture after additional 100 years of fertilization (10100 years), d) conservative tracer after additional 100 years of fertilization (10100 years). The oxygen propagation becomes quasi steady state and patterns of oxygen and nitrate concentration are visibly similar.

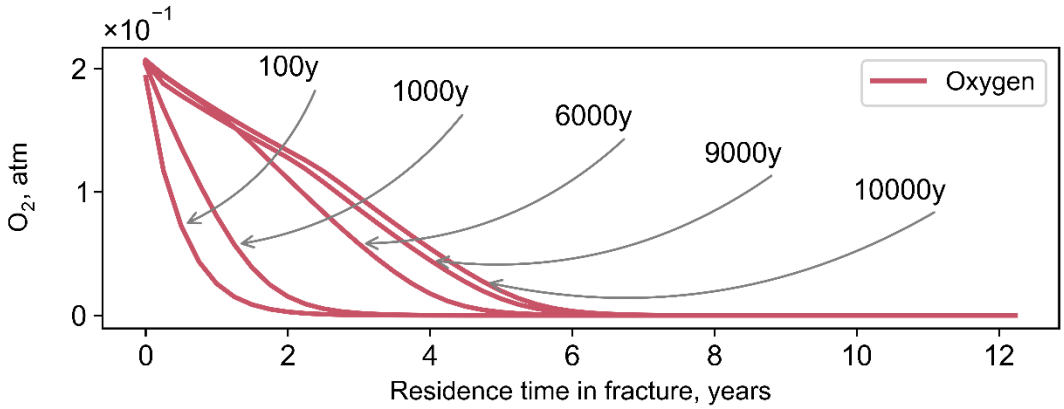

Fig.6.7. Evolution of the O_2 profile along the fracture. The oxygen propagation becomes quasi steady state after 8000-9000 years.

6.5.2 SCENARIO 2

In this scenario, denitrification is not allowed in the matrix. Oxygen follows the same pattern as that in the previous scenario, although it propagates a bit further along the fracture(Fig.6.8a and 6.9c). Nitrate in this case is not consumed by pyrite and ferrous iron oxidation and thus propagates rapidly throughout the oxic and anoxic zones similar as a conservative tracer. Thus the only important retardation process for NO_3^- here is matrix diffusion (Fig. 6.8b, Fig. 6.8c, Fig. 6.9a and 6.9b). Ferrihydrite coatings precipitate in the fracture, but the mineral volume would be too small to affect fracture flow significantly. Goethite concentration is negligible (Fig. 6.9d). Parts of Fe^{2+} mass diffused into the fracture and react there with oxygen and nitrate; only 10% of it appears in the matrix (Fig. 6.8d).

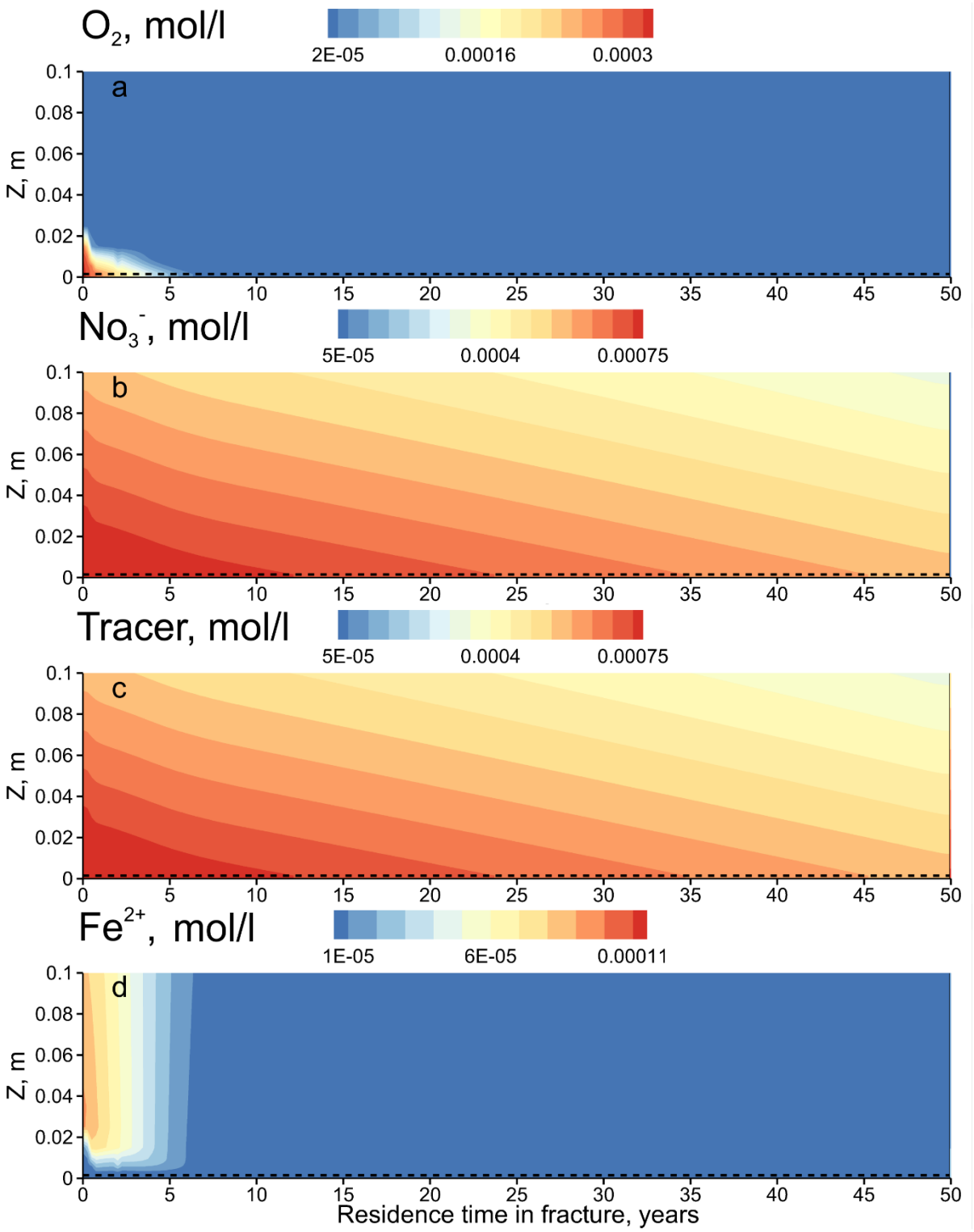

Fig. 6.8. Selected simulation results for scenario 2 (denitrification in the matrix is not allowed) after 10100 years:: a) O_2 distribution in matrix and fracture, b) NO_3^- distribution at a time, c) Conservative tracer distribution at a time 10100 years, d) Ferrous iron distribution at a time 10100 years. The oxygen propagation becomes steady state; nitrate behavior matches the conservative solutes, dissolved iron only appears in the matrix.

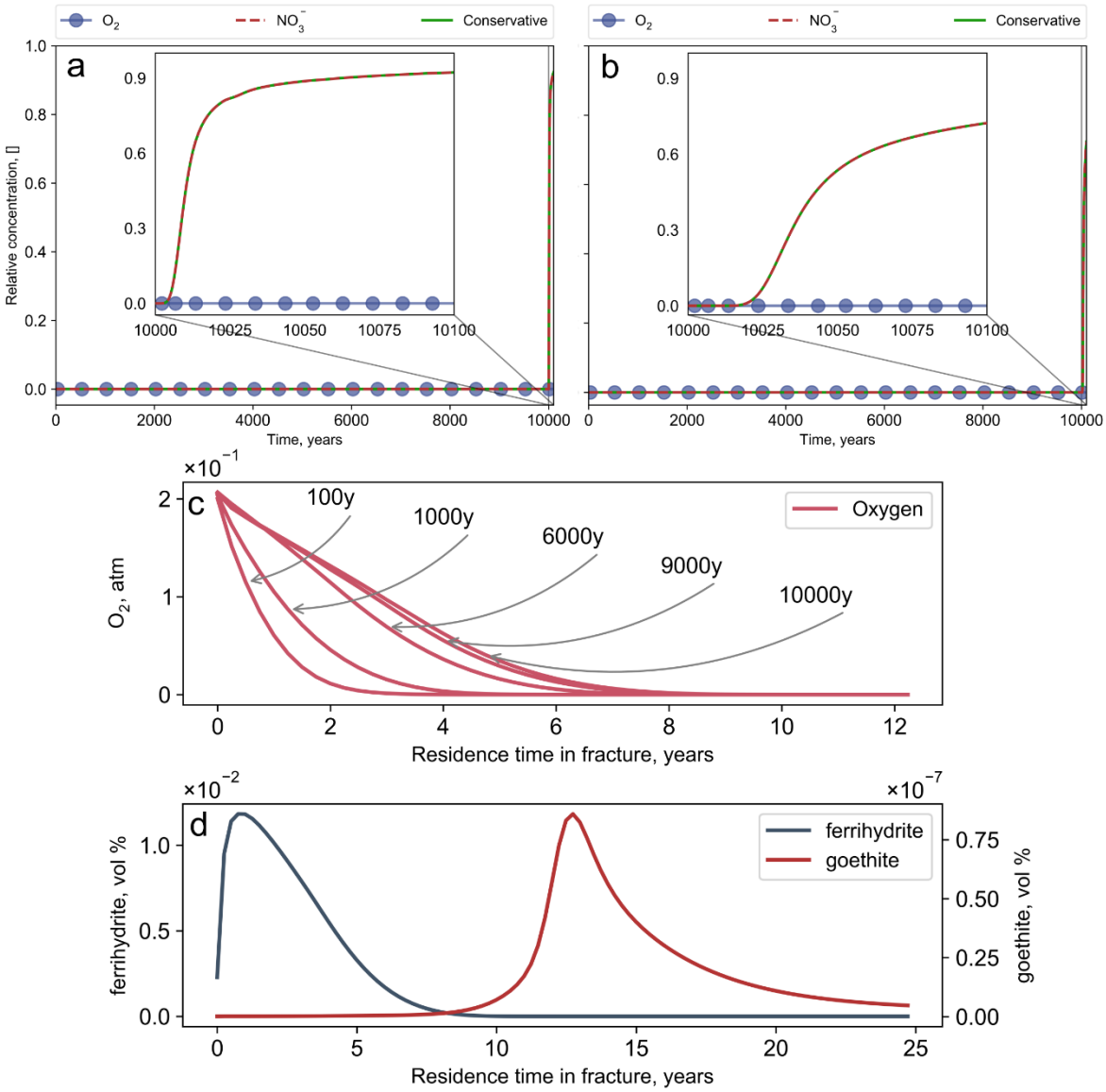

Fig. 6.9. a) O_2, NO_3^- and conservative tracer breakthrough curves at the fracture outlet for a residence time of water in the fracture of 10 years and b) 50 years (5 times longer travel distance), c) Evolution of the O_2 profile in the fracture. d) Iron hydroxides profiles in the fracture at a time 10100 years. The NO_3^- and conservative tracer breakthrough curves concur, oxygen propagation becomes quasi steady state approximately at 8000-9000 thousand years, the concentration of goethite (which indicates Fe^{2+} oxidation by nitrate) is neglectable compared to ferrihydrite

Scenarios 2.1 and 2.2 test the importance of pyrite oxidation reaction rates in scenario 2. Both, effective diffusion coefficients and pyrite oxidation reaction rates were tested. The effective diffusion coefficient in natural media is mostly a function of porosity ($D_e \approx D_{aq}\,\varepsilon^{2.2}$) and indeed conservative tracer and NO_3^- concentrations show a slight difference when the matrix porosity is increased to 0.3 because more iron is being produced (Fig. 6.10a and Fig. 6.10b). In this case, oxygen transport is also affected and propagates rapidly trough the rock matrix (Fig. 6.10c). Such high porosities, however, is not observed for micritic limestone. The

switch to instantaneous equilibrium pyrite oxidation reaction in opposite does not change the concentration patterns and do not affect the system significantly (not shown) proving reaction kinetics are diffusion controlled.

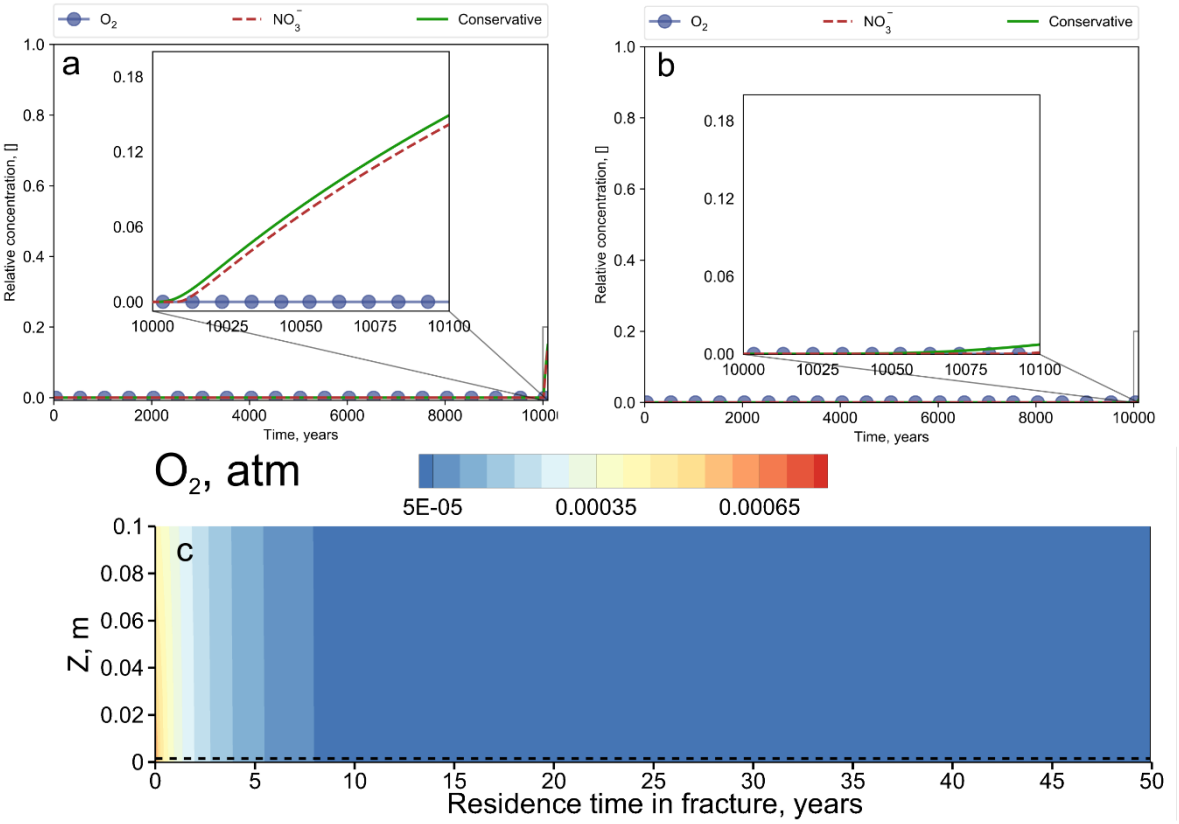

Fig.6.10. Selected results for scenario 2.1 (matrix porosity is increased): a) O_2, NO_3^- and conservative tracer breakthrough curves at 5 years and b) 15 years residence time in the fracture, c) O_2 distribution after at a time 10100 years. The concentration pattern of oxygen differs markedly from the base case; the difference between conservative tracer and nitrate breakthrough curves is due to different effective diffusion coefficients

6.5.3 SCENARIO 3

In this case, neither O_2 nor nitrate react with pyrite in the rock matrix while siderite is introduced and is the only source of electron donors. All reactions are assumed to solely happen by microbial processes in the fracture. O_2 propagates further in both fracture and matrix (Fig. 6.11a) although Fe^{2+} oxidation with ferrihydrite precipitation happens in the fracture (Fig. 6.11c). Oxygen penetrates the matrix completedly up to 1 m which is the maximum size of the block used in the model. Nitrate behaves like a conservative tracer since all iron released into the fracture gets consumed by oxygen (denitrification by Fe^{2+} is inhibited in oxic conditions) (Fig. 6.11b). In scenario 3.1 where reactions with Fe^{2+} in the matrix are allowed too, solutes form almost the same patterns because of low pH in the influx water gets buffered rapidly near the fracture inlet, and iron is released at a neglectable small concentration in the matrix.

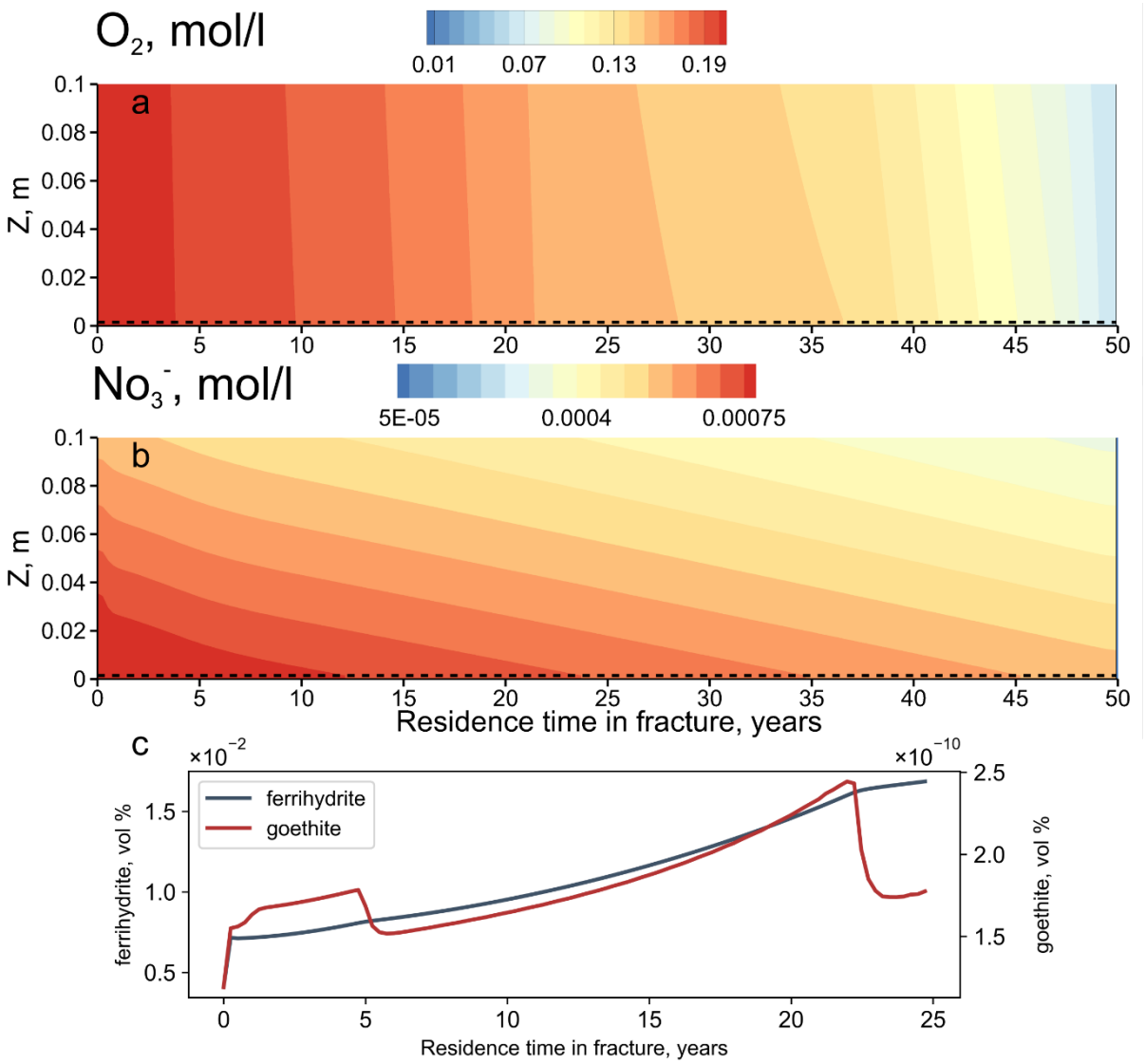

Fig. 6.11. Selected results for scenario 3 after 10100 (teste of the influence of siderite presence). a) O_2 distribution in the matrix and fracture, b) NO_3^- distribution at the time (after 100 years application) (behave as a the conservative tracer) and c) iron hydroxides profiles in the fracture. Presence of siderite in the matrix affects redox equilibria (oxygen), however, low solubility prevents enough iron release to affect nitrate transport.

6.5.4 SCENARIO 4

Siderite and pyrite are present both in the matrix. Dissolved oxygen behaves similar to scenario 1 and 2 with no significant difference (Fig. 6.12a). However, when nitrate is released, it behaves very differently (Fig. 6.12b). The pattern is different from both conservative tracer and O_2 (Fig. 6.12e and Fig. 6.12f). While denitrification still is allowed only in the fracture nitrate is compledly reduced after 15-17 years residence time. Concentrations of goethite in the fracture are now comparable to ferrihydrite, although goethite precipitates further downstream in the fracture. In the rock matrix, nitrate penentrates maximum 50 cm. The overall pH in the rock matrix is now lower than that in previous scenarios and reaches 7 (Fig. 6.12c) and thus more siderite dissolves and more Fe^{2+} gets

released (Fig. 6.12d) especially in the vicinity of the fracture. In scenario 2.1 with less siderite (0.005 vol%) even these low concentrations of siderite in the matrix affect nitrate transport compared to the pure pyrite scenarios. The denitrification profile along the fracture is still smooth, however, nitrate is still present after 25 years residence time (Fig. 6.13) since less dissolved iron occurs in the matrix and fracture.

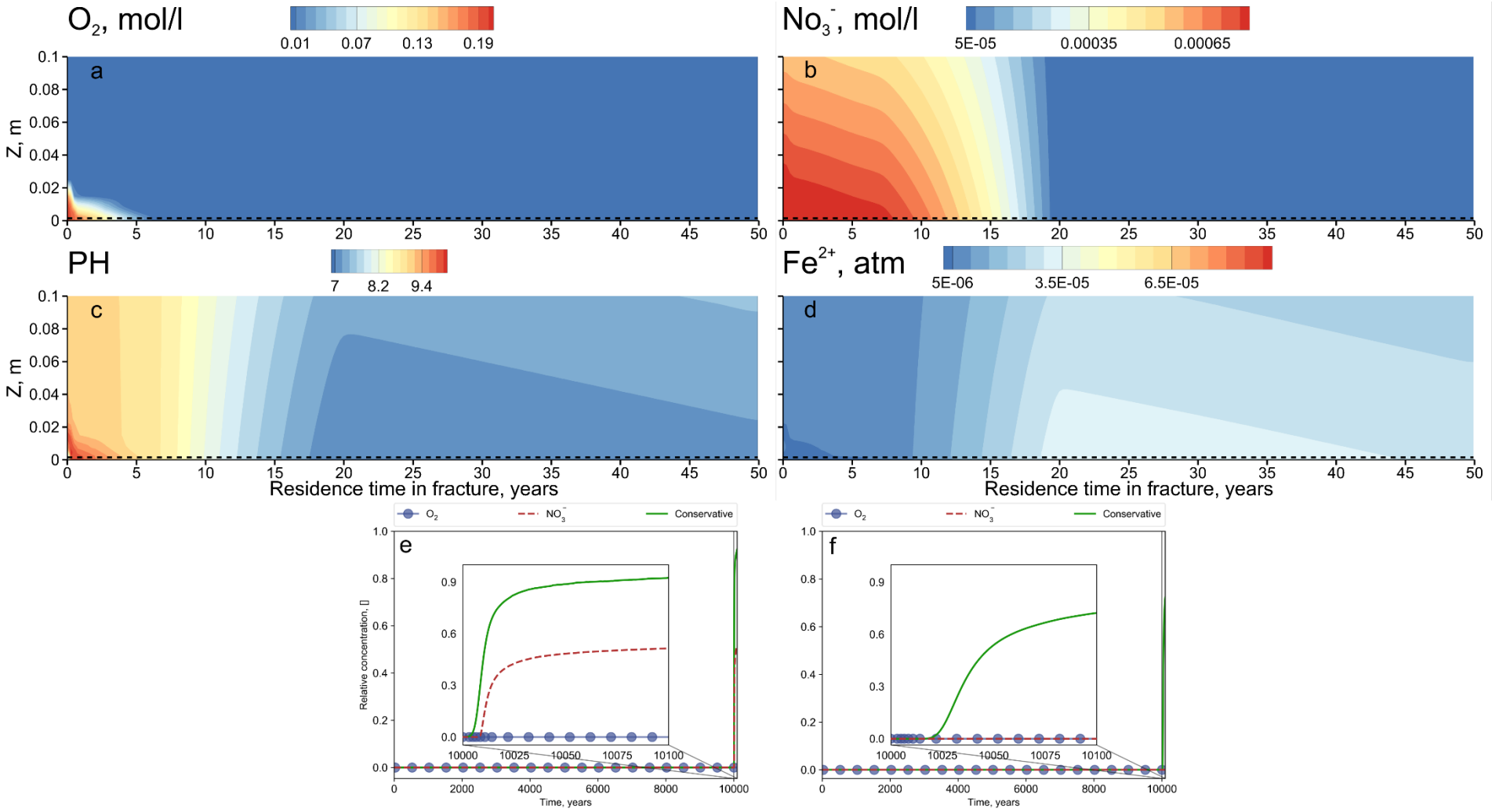

Fig. 6.12. Selected results for scenario 4 after 10100 years (O^2 consumption in matrix and fracture, NO_3^- consumption only in fracture, siderite and pyrite are present): a) O_2 distribution, b) NO_3^- distribution, c) pH distribution at time, d) Fe^{2+} distribution, e) O_2 (red), NO_3^- (blue dots) and conservative tracer (green) breakthrough curves at residence time of 10 years and f) 50 years. The pH drop produced by abiotic pyrite oxidation induces siderite dissolution, and thus Fe^{2+} is released into the fracture

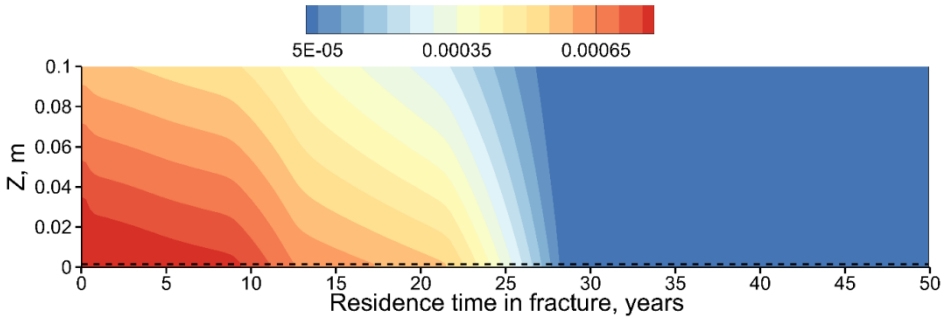

Fig. 6.13 NO_3^- distribution (mol/l) in the rock matrix at time 10100 years for scenario 4.1 (comprising less siderite). Even a siderite concentration in the matrix of only 0.001 vol% affects nitrate transport significantly.

6.5.5 SCENARIO 5

Here pyrite is present not only in the matrix but also present on a fracture surface, thus directly accessible to electron acceptors dissolved in the groundwater in the fracture. Dissolved oxygen behaves close to the scenario 1 and 2 (Fig. 6.14a). However, the difference in the nitrate propagation is significant. After 100 years application, it is only present in water which has a residence time in the fracture less than 10 years and penetrates only 10 cm into the matrix. (Fig. 6.14b). Scenario 5.1 (which has pyrite oxidation in the matrix turned off leaving only pyrite in the fracture) does not show any retardation for both O_2 and NO_3^- because all pyrite in the fracture got oxidated long before fertilization started. In scenario 5.2 (which has siderite presented in the matrix as well as pyrite in the matrix and the fracture) O_2 behaves similarly to scenario 3 (no oxidation in the matrix). Likewise, NO_3^- behaves as a conservative tracer because most of the pyrite in the fracture was already consumed before nitrate input starts (not shown).

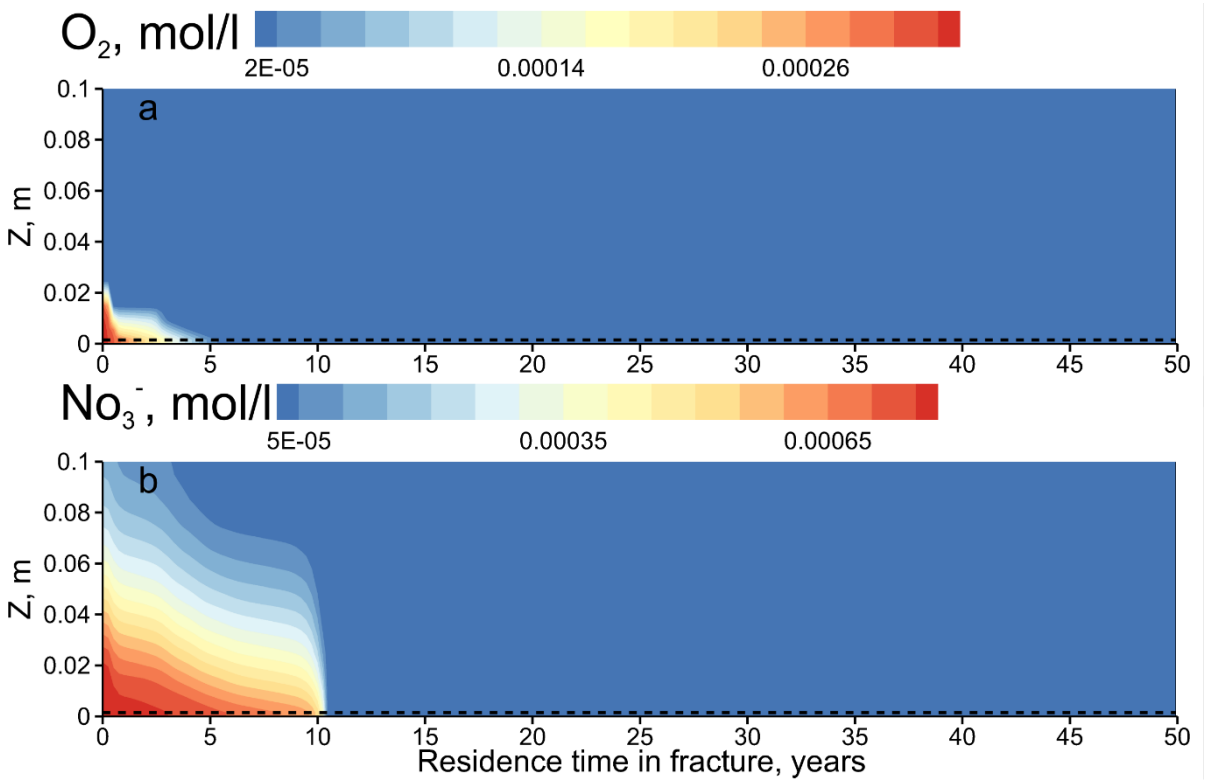

Fig. 6.14 Selected results for scenario 5 after 10100 years (pyrite resides on the surface of the fracture): a) O_2 distribution in the matrix and fracture, b) NO_3^- distribution in the matrix and fracture. The presence of the pyrite in the fracture affects redox reactions for both, oxygen and nitrate but only if pyrite is also allowed to react with oxygen in the matrix.

6.6 DISCUSSION

6.6.1 GENERAL OBSERVATIONS

Before going into more detailed discussion, several essential details are worth noting. In scenarios 1, 2 and 4 oxygen behaves in the same way since most of it gets reduced by pyrite oxidation in the rock matrix. The oxygen is being consumed during the first 5 years residence time. Thus, all fast flow paths in the fractured karst system with the residence time of less than 5 years would contain oxygen and thus provide a perfect transit zone for nitrate. However, along with the "longer" flow paths (non- or moderately karstified) environment the fracture water becomes reduced after 5 years residence time providing the potential for denitrification. The abundance of Fe^{2+} can decrease the distance of the oxygen transport but it is moderate. It is also interesting that the diffusion controlled nature of the studied system does not correspond with results of *Spiessl et al.* (2008), who found that oxidation rates of the electron donor minerals (namely biotite) to be the most crucial parameter collectively with fracture aperture and flow velocity. The velocity and fracture aperture importance correspond well to the results of the models performed in this section since aperture and flux velocity are related by the cubic law, and both affect travel time; thus travel time (residence time) controls

the chemistry of a given water parcel in our approach. The difference in the diffusion/kinetic control of the systems can be explained by the fact that pyrite oxidation is faster than biotite oxidation and because of effective diffusion coefficients in Muschelkalk limestones one order of magnitude lower than in the granites studied by Spiessl et al. (2008). This difference, even with close porosity values, in consequence, can be explained by the significantly different pore structure of igneous and sedimentary rocks.

6.6.2 IMPORTANCE OF BIOTA LOCATION

The location of biofilms (or bioactivity) is essential for oxygen and nitrate transport in the fractured groundwater system. In case that there are no size restrictions for microorganisms the typical redox sequence [*Appelo and Postma*, 2005] is formed in both fracture and matrix and nitrate does not migrate much further than dissolved oxygen which does not correspond to data observed in the aquifer [*Grathwohl et al.*, 2017], where relatively high NO_3^- concentrations are observed in anoxic zones. Moreover, iron hydroxide coatings are usually observed on fracture surfaces and in close vicinity of it. This indicates that no Fe^{2+} oxidation happens in the matrix. When only abiotic oxidation of pyrite is allowed (only by oxygen, not with nitrate), no Fe^{2+} oxidation happens in the matrix and the diffusive fluxes of dissolved iron into the fracture are insufficient to affect the nitrate concentrations (unless the effective diffusion coefficient was dramatically higher, e.g., in rocks with porosities higher than 20%, which is not realistic for limestone systems studied here). Sufficient denitrification in the fracture, however, can be provided by the presence if minerals on fracture walls, especially of their concentration is relatively high.

6.6.3 IMPORTANCE OF SIDERITE CONCENTRATION

To fit observed nitrate concentrations in the Muschelkalk aquifer, other electron donor minerals have been considered except of pyrite. Although the presence of siderite in such limestones is thermodynamically unlikely, it was observed in various sediments [*Ellwood et al.*, 1988]. This was approved by investigations of Triassic limestone samples collected in the studied area (**Appendix I**). The presence of siderite alone, however, does not provide sufficient denitrification due to its low solubility. Low pH values in water increase solubility of siderite, but in limestones pH gets buffered in the oxic zone already at the inlet of the fracture. Thus all additionally released iron is consumed by oxygen. However, due to abiotic oxidation of pyrite in the matrix (when it is allowed) hydrogen ions are being released, thus

decrease the pH and increase siderite dissolution and therefore more Fe^{2+} is released in the fracture. Once Fe^{2+} is oxidized forming hydroxides, pH decreases again forcing even more siderite to be dissolved. This cycle self-develops and the system increases its reduction potential with time. This process gets even more visible if pyrite presence on the fracture wall is considered.

6.6.4 IMPORTANCE OF ELECTRON DONORS ON A FRACTURE SURFACE

Presence of pyrite on fracture surfaces seems to be one of the most realistic sources of mineral electron donors accessible for bacteria. Indeed the nitrate concentration significantly differs from the conservative tracer pattern once pyrite on the fracture wall is considered. However, this effect is only relevant if oxygen is already attenuated around the inlet of the fracture. If the pyrite is allowed only in the fracture and no O_2 gets reduced in the matrix, all pyrite in the fracture is rapidly consumed in less than 1000 years, and the water becomes fully oxic allowing no denitrification of NO_3^-. Presence of pyrite on fracture surfaces was hypothesized to result in a drop pH which induces the siderite dissolution without pyrite oxidation in the matrix, therefore, providing a scenario where pyrite oxidation in the matrix is not needed for denitrification in the fracture. However significant denitrification seems to be impossible without pyrite oxidation by oxygen in the matrix, even thought this process does not reduce NO_3^- directly.

6.7 SUMMARY AND CONCLUSIONS

In this modeling study, reactive transport in a fractured limestone aquifer at catchment-scale was investigated. The flow was assumed to pass through a connected system of fractures and karstified features providing the continuous exposure of water parcel to the limestone surface. A “two plates” model was implemented which represents a flow path through such a system of fractures where the residence time of the groundwater in the fracture controls the water chemistry.

The aim was to better understand slow in-situ pollutant transformation processes in such aquifers and to evaluate different scenarios and pathways of pollutant turnover. A key question was to identify the role of microbial activity e.g. if microorganisms are excluded from the matrix due to small pore sizes. Such scenarios were developed and tested in comparison with a base case where bacteria are allowed in the matrix. Significant differences in fate and transport of oxygen and nitrate were observed for various scenarios. If all reactions

are allowed in both matrix and fracture, typical redox zonations form with steep redox gradients in both, matrix and fracture.

As observed in the field, all electron acceptors are consumed in the groundwater in the fractures after relatively short residence times, and their transport is significantly slowed down (retarded) in comparison to a conservative tracer.

However, pyrite oxidation by NO_3^- is assumed to be possible only with microbial activity. The amount of Fe^{2+} released due to oxidation of pyrite by O_2 in the matrix is not enough to affect nitrate concentrations. Reactions in this setup are controlled by diffusion in the rock matrix, and only increased effective diffusion coefficients may allow high Fe^{2+} fluxes into the fracture causing denitrification in scenario 2. Such large effective diffusion coefficients, however, would require high matrix porosities (e.g., 3 times higher than observed).

Since the field observation showed that water in fractures older than 20-25 years is free of nitrate, additional electron donors sources are proposed to fit the observations. Only two plausible explanations realistically explain the denitrification in the system if microbes in the matrix are absent (due to too small pore sizes):

1. Siderite is present in the limestone matrix and dissolves parallel to pyrite
2. Pyrite is exposed on fracture surfaces (in the anaerobic part of the fracture).

Both scenarios, however, require reduction of the oxygen in the rock matrix, which is easily possible by abiotic reaction with pyrite.. In the first case, an initial pH drop is needed in the fracture to increase solubility of siderite. In the second case, the oxygen concentration in the fracture has to be low, otherwise, it consumes all pyrite on the fracture wall and the fracture groundwater becomes aerobic long before nitrate is released. Abiotic reactions of oxygen and pyrite have been reported in the literature [e.g., *Appelo and Postma*, 2005, *Sidborn*, 2007], thus these scenarios are assumed to be realistic. The precipitation of iron hydroxides in the fracture decreases pH further and enhances dissolution of carbonates which, in the long term, would favour karstification. Moreover, if siderite is present, this pH decrease would increase the amount of Fe^{2+} released by the siderite dissolution.

The results demonstrate that effective diffusion coefficients and electron donor mineral contents of rock facies of the aquifer should be studied at various scales including geochemical heterogeneities. Reaction rates at the mineral scale can be neglected since they do not provide any control on O_2 and NO_3^- fluxes into the matrix at the time scales investigated. Transport limitations because of precipitation on the rock surfaces, changes of effective diffusion coefficients due to precipitations in pores were not considered in this

study. The geochemical heterogeneity should also be included and studied for more realistic representation and better understanding the redox evolution and redox-sensitive pollutant transport in such systems.

The results of this study are relevant for water management. After 6 years residence time the groundwater in the fracture becomes anaerobic and thus nitrate reduction may happen. Then two ways of nitrate fate are feasible. When enhanced siderite dissolution allows a high flux of ferrous iron from the matrix into the fracture, nitrate is reduced, and it would take tremendous amount of time until siderite is depleted from the matrix. If the only accessible electron donor for NO_3^- are pyrite crystals on the fracture wall, then the potential for denitrification is nearly exhausted and therefore the breakthrough is expected in the short term. To distinguish between these two scenarios, the comprehensive field campaign should be conducted.

1. The pyrite and siderite content should be determined in reduced facies of the aquifer.
1. The Fe^{2+} concentrations and pH should be measured for water of various water ages in the oxidised and reduced zones in the fracture.
2. SO_4^{2-} concentrations and isotope signature should be measured in the fracture
3. The biofilms on the fracture wall should be sampled for water of various water ages, to determine what denitrifying process predominates

7. OVERALL CONCLUSIONS AND OUTLOOK

Numerical flow and reactive transport modeling were employed for studying the long-term geochemical groundwater evolution and contaminant transport at the landscape scale. Nitrate reactive transport is the major concern. However, other important related species (O_2, Fe^{2+} species, etc.) were also included. The main findings of this study are:

The groundwater divide between two valleys in the typical SW Germany hilly landscape is likely to be shifted into one of the valleys (relative to topographical water divide) if river water levels in both valleys are noticeably different. Its exact position is controlled by the geometrical and geological settings of the system, water level differences in main regional drains, groundwater recharge rates, and bedrock hydraulic conductivity. With these few parameters, the position of groundwater divide can be constrained; the major uncertainty is the bedrock hydraulic conductivity which, however, stays in a narrow range to match field hydraulic conditions (water levels).

Water divide shifts may cause pollutants export and should be considered in water management. In the studied example, a significant share of the Neckar valley nitrate plume is likely to originate in the Ammer valley. Nitrate applied on the southern slopes of the Ammer valley is likely transported conservative through oxidized Triassic bedrocks towards the Neckar valley. There the nitrate plume penetrates the gravel aquifer from the bottom and is not attenuated since no significant electron donor source (i.e. organic carbon) is present in the Pleistocene sand and gravels. Therefore, shifts in the groundwater divide may significantly affect the vulnerability of aquifers.

Generally, in systems with similar climate, geology and topography, the size of the groundwater divide shift is induced by large water level difference between two rivers. The size of this difference is mainly a result of artificial rivers management and thus can be controlled. The exported plume depth can serve as a proxy for the plume source: the further the contaminate source from the topographical water divide – the deeper the plume would be observed.

In case when the high organic carbon rich layers are present in the floodplain, like in the Ammer floodplain case, potentially applied nitrate is reduced in such layers, for instance organic carbon rich clays or lacustrine silts and does not reach any drains. However, natural NH_4^+ may be released from these layers in the valley sediments and is transported to the river and drains. Subsequent oxidation of ammonia may lead to high concentration of nitrate in

these surface waters as observed. Sulfate also undergoes reduction along the flow paths but partly reaches the drains along with H_2S, which smell is observed along the drains. In addition, the model suggests calcite precipitation along the water flow paths and possible degassing of N_2. Developed model can be applied to test systems sensitivity for pore space clogging by calcite precipitation or degassing in the long term.

The Upper Muschelkalk limestone aquifer was conceptualized as a series of connected fractures and represented as one streamline. Transport was simulated using constant flow velocity which is controlled by hydraulic gradients and fractures aperture and thus controls the exposure time to the fracture walls of a water parcel.

The long-term redox evolution and pollutants fate of such system is controlled by electron donor minerals and their accessibility for electron acceptors, the porosity of the matrix, porous sizes and effective diffusion coefficient. The suppression of microbe development in the limestone matrix affects the redox-sensitive transport significantly. Several conditions have to be fulfilled to obtain high enough reduction potential to observe denitrification. First, the oxygen should be reduced in the rock matrix abiotically and oxic zone should be shorter than the flow path. In the presented case, oxygen reacts with pyrite in the rock matrix and concentration profile in the fracture becomes quasi steady state after 8000 years while all water in fracture older than 6 years is anaerobic. Second, the electron donor source accessible for the nitrate in the fracture should be present. For the case in question two possible electron sources are proposed:

1. Ferrous iron originated by dissolution of siderite presented in the rock matrix, which is enhanced by pyrite oxidation in the matrix by O_2, which decreases pH. The iron then diffuses in the fracture and is oxidised into the iron hydroxide, which decreases pH even more.

2. Sufficient amount of pyrite crystals exposed in the fracture wall, where they are accessible for both nitrate and bacteria.

The concentration of pyrite and siderite in the matrix significantly affects the reactive transport through the aquifer. Local mineral scale reaction kinetics proved to be neglectable in the long term due to the low effective diffusion coefficients of solutes in the limestone matrix.

The developed model can be used in future for testing systems sensitivity to various electron donor minerals concentrations, as well as to other possible species or processes which can affect redox system. Furthermore, it can be used for prediction of groundwater

quality based on water ages. The modelling approach can be improved by including chemical heterogeneity assessment. For that extensive field and lab research should be done do determine various facies (e.g. more pyrite or more siderite). In this case, the exposure times for flow paths becomes a source of uncertainty and can be dealt with in a probabilistic way.

Overall, this dissertation shows that the water and land use management and decision-making in catchment scale should be based on detailed and comprehensive investigation of the system in question, since the fate of pollutants in such scale depends on various complex processes, which furthermore are interlinked in a way that cannot be identified in the lab scale studies.

REFERENCES

Abdelghani, F. Ben, M. Aubertin, R. Simon, and R. Therrien (2015), Numerical simulations of water flow and contaminants transport near mining wastes disposed in a fractured rock mass, *Int. J. Min. Sci. Technol.*, *25*(1), 37–45, doi:10.1016/J.IJMST.2014.11.003.

Aigner, T., and G. H. Bachmann (1989), Dynamic stratigraphy of an evaporite-to-red bed sequence, Gipskeuper (Triassic), southwest German Basin, *Sediment. Geol.*, *62*(1), 5–25, doi:10.1016/0037-0738(89)90098-5.

Aigner, T., and G. H. Bachmann (1992), Sequence-stratigraphic framework of the German Triassic, *Sediment. Geol.*, *80*(1-2), 115–135, doi:10.1016/0037-0738(92)90035-P.

Aller, L., T. Bennett, J. H. Lehr, and R. J. Petty (1987), *DRASTIC: A Standardized System for Evaluating Ground Water Pollution Potential Using Hydrogeologic Settings*, NWWA/EPA series, Robert S. Kerr Environmental Research Laboratory, Office of Research and Development, U.S. Environmental Protection Agency.

Andersen, P. Ø., and S. Evje (2016), A model for reactive flow in fractured porous media, *Chem. Eng. Sci.*, *145*, 196–213, doi:10.1016/j.ces.2016.02.008.

Anderson, M. P., W. W. Woessner, and R. J. Hunt (2015), *Applied Groundwater Modeling: Simulation of Flow and Advective Transport*, Academic Press.

Antonellini, M., P. N. Mollema, and L. Del Sole (2017), Application of analytical diffusion models to outcrop observations: Implications for mass transport by fluid flow through fractures, *Water Resour. Res.*, *53*(7), 5545–5566, doi:10.1002/2016WR019864.

Appelo, C. A. J., and D. Postma (2005), *Geochemistry, Groundwater and Pollution, Second Edition*, Taylor & Francis, Layden.

Arnold, J. G., R. Srinivasan, R. S. Muttiah, and J. R. Williams (1998), Large area hydrologic modeling and assessment part I: model development, *J. Am. Water Resour. Assoc.*, *34*(1), 73–89, doi:10.1111/j.1752-1688.1998.tb05961.x.

Bakalowicz, M. (2005), Karst groundwater: a challenge for new resources, *Hydrogeol. J.*, *13*(1), 148–160, doi:10.1007/s10040-004-0402-9.

Bakshevskaia, V. A., and S. P. Pozdniakov (2016), Simulation of Hydraulic Heterogeneity and Upscaling Permeability and Dispersivity in Sandy-Clay Formations, *Math. Geosci.*, *48*(1), 45–64, doi:10.1007/s11004-015-9590-1.

Bao, Z., C. M. Haberer, U. Maier, R. T. Amos, D. W. Blowes, and P. Grathwohl (2017), Modeling controls on the chemical weathering of marine mudrocks from the Middle Jurassic in Southern Germany, *Chem. Geol.*, *459*, 1–12, doi:10.1016/J.CHEMGEO.2017.03.021.

Barenblatt, G. E., I. P. Zheltov, and I. N. Kochina (1960), Basic concepts in the theory of seepage of homogeneous liquids in fissured rocks, *J. Appl. Math. Mech.*, *24*(5), 1286–1303.

Barry, D. A., H. Prommer, C. T. Miller, P. Engesgaard, A. Brun, and C. Zheng (2002), Modelling the fate of oxidisable organic contaminants in groundwater, *Adv. Water Resour.*, *25*(8-12), 945–983, doi:10.1016/S0309-1708(02)00044-1.

Bear, J. (1972), *Dynamics of fluids in porous media.*, American Elsevier Pub. Co.

Best, A., E. Arnaud, B. Parker, R. Aravena, and K. Dunfield (2015), Effects of Glacial Sediment Type and Land Use on Nitrate Patterns in Groundwater, *Groundw. Monit. Remediat.*, *35*(1), 68–81, doi:10.1111/gwmr.12100.

Böhlke, J. K. (2002), Groundwater recharge and agricultural contamination, *Hydrogeol. J.*, *10*(1), 153–179, doi:10.1007/s10040-001-0183-3.

Böhlke, J. K., R. Wanty, M. Tuttle, G. Delin, and M. Landon (2002), Denitrification in the recharge area and discharge area of a transient agricultural nitrate plume in a glacial outwash sand aquifer, Minnesota, *Water Resour. Res.*, *38*(7), 10–1–10–26, doi:10.1029/2001WR000663.

Brun, A., and P. Engesgaard (2002), Modelling of transport and biogeochemical processes in pollution plumes: literature review and model development, *J. Hydrol.*, *256*(3-4), 211–227, doi:10.1016/S0022-1694(01)00547-9.

Chen, L., Q. Kang, Q. Tang, B. A. Robinson, Y. He, and W. Tao (n.d.), Pore-scale simulation of multicomponent multiphase reactive transport with dissolution and precipitation, , 1–50.

Chen, Z. et al. (2017), The World Karst Aquifer Mapping project: concept, mapping procedure and map of Europe, *Hydrogeol. J.*, *25*(3), 771–785, doi:10.1007/s10040-016-1519-3.

Cirpka, O. a., M. Rolle, G. Chiogna, F. P. J. De Barros, and W. Nowak (2012), Stochastic evaluation of mixing-controlled steady-state plume lengths in two-dimensional heterogeneous domains, *J. Contam. Hydrol.*, *138-139*, 22–39, doi:10.1016/j.jconhyd.2012.05.007.

D. H. Tang, E. a. Sudicky, and E. O. Frind (1981), Contaminant Transport in Fractured Porous Media: Analytical Solution for a Single Fracture, *Water Resour. Res.*, *20*(7), 1021, doi:10.1029/WR020i007p01021.

Dragon, K. (2012), Groundwater nitrate pollution in the recharge zone of a regional Quaternary flow system (Wielkopolska region, Poland), *Environ. Earth Sci.*, *68*(7), 2099–2109, doi:10.1007/s12665-012-1895-5.

Druhan, J. L., S. Vialle, K. Maher, and S. Benson (2014), A reactive transport model for geochemical mitigation of CO2 leaking into a confined aquifer, *Energy Procedia*, *63*, 4620–4629, doi:10.1016/J.EGYPRO.2014.11.495.

Eichhubl, P., N. C. Davatzes, and S. P. Becker (2009), Structural and diagenetic control of fluid migration and cementation along the Moab fault, Utah, *Am. Assoc. Pet. Geol. Bull.*, *93*(5), 653–681, doi:10.1306/02180908080.

Ellwood, B. B., T. H. Chrzanowski, F. Hrouda, G. J. Long, and M. L. Buhl (1988), Siderite formation in anoxic deep-sea sediments: A synergetic bacteria controlled process with improtant implications in paleomagnetism, *Geology*, *16*(11), 980, doi:10.1130/0091-7613(1988)016<0980:SFIADS>2.3.CO;2.

European Enviromental Agency (2017), *Landscapes in Transition. An account of 25 years of land cover change in Europe*.

Freeze, R. A., and J. A. Cherry (1979), *Groundwater*, Prentice-Hall.

Fuchs, M., M. Will, E. Kunert, S. Kreutzer, M. Fischer, and R. Reverman (2011), The temporal and spatial quantification of Holocene sediment dynamics in a meso-scale catchment in northern Bavaria, Germany, *The Holocene*, *21*(7), 1093–1104, doi:10.1177/0959683611400459.

Van Genuchten, M. T. (1980), A closed-form equation for predicting the hydraulic conductivity of unsaturated soils, *Soil Sci. Soc. Am. J.*, *44*(5), 892–898.

Gleeson, T., L. Marklund, L. Smith, and A. H. Manning (2011), Classifying the water table at regional to continental scales, *Geophys. Res. Lett.*, *38*(5), n/a–n/a, doi:10.1029/2010GL046427.

Goode, D. J. (1996), Direct Simulation of Groundwater Age, *Water Resour. Res.*, *32*(2), 289–296, doi:10.1029/95WR03401.

Grathwohl, P. (1998), *Diffusion in Natural Porous Media: Contaminant Transport, Sorption/Desorption and Dissolution Kinetics*, Topics in Environmental Fluid Mechanics, Springer US, Boston, MA.

Grathwohl, P. et al. (2017), Proposal for the Establishment and Funding of Collaborative Research Center 1253 Catchments as Reactors: Metabolism of Pollutants on the Landscape Scale (CAMPOS), , 398.

Grisak, G. E., and J. F. Pickens (1981), An analytical solution for solute transport through fractured media with matrix diffusion, *J. Hydrol.*, *52*(1-2), 47–57, doi:10.1016/0022-1694(81)90095-0.

Haese, R. R., K. Wallmann, A. Dahmke, U. Kretzmann, P. J. Müller, and H. D. Schulz (1997), Iron species determination to investigate early diagenetic reactivity in marine sediments, *Geochim. Cosmochim. Acta*, *61*(1), 63–72, doi:10.1016/S0016-7037(96)00312-2.

Haitjema, H. M., and S. Mitchell-Bruker (2005), Are Water Tables a Subdued Replica of the Topography?, *Ground Water*, *0*(0), 050824075421008, doi:10.1111/j.1745-6584.2005.00090.x.

Hansen, a. L., D. Gunderman, X. He, and J. C. Refsgaard (2014), Uncertainty assessment of spatially distributed nitrate reduction potential in groundwater using multiple geological realizations, *J. Hydrol.*, *519*, 225–237, doi:10.1016/j.jhydrol.2014.07.013.

Heidari, P., L. Li, L. Jin, J. Z. Williams, and S. L. Brantley (2017), A reactive transport model for Marcellus shale weathering, *Geochim. Cosmochim. Acta*, *217*, 421–440, doi:10.1016/J.GCA.2017.08.011.

Heppell, C., a. Louise Heathwaite, A. Binley, P. Byrne, S. Ullah, K. Lansdown, P. Keenan, M. Trimmer, and H. Zhang (2014), Interpreting spatial patterns in redox and coupled water-nitrogen fluxes in the streambed of a gaining river reach, *Biogeochemistry*, *117*(2-3), 491–509, doi:10.1007/s10533-013-9895-4.

Howden, N. J. K., T. P. Burt, S. A. Mathias, F. Worrall, and M. J. Whelan (2011), Modelling long-term diffuse nitrate pollution at the catchment-scale: Data, parameter and epistemic uncertainty, *J. Hydrol.*, *403*(3-4), 337–351, doi:10.1016/j.jhydrol.2011.04.012.

Huang, J., and M. N. Goltz (2015), Semianalytical solutions for transport in aquifer and fractured clay matrix system, *Water Resour. Res.*, *51*(9), 7218–7237, doi:10.1002/2014WR016073.

Jang, E., W. He, H. Savoy, P. Dietrich, O. Kolditz, Y. Rubin, C. Schüth, and T. Kalbacher (2017), Identifying the influential aquifer heterogeneity factor on nitrate reduction processes by numerical simulation, *Adv. Water Resour.*, *99*, 38–52, doi:10.1016/j.advwatres.2016.11.007.

Jurjovec, J., D. W. Blowes, C. J. Ptacek, and K. U. Mayer (2004), Multicomponent reactive transport modeling of acid neutralization reactions in mine tailings, *Water Resour. Res.*, *40*(11), doi:10.1029/2003WR002233.

Kostic, B., and T. Aigner (2007), Sedimentary architecture and 3D ground-penetrating radar analysis of gravelly meandering river deposits (Neckar Valley, SW Germany), *Sedimentology*, *54*(4), 789–808, doi:10.1111/j.1365-3091.2007.00860.x.

Lang, A., and S. Nolte (1999), The chronology of Holocene alluvial sediments from the Wetterau, Germany, provided by optical and 14 C dating, *The Holocene*, *9*(2), 207–214, doi:10.1191/095968399675119300.

Langman, J., M. Moore, C. Ptacek, L. Smith, D. Sego, and D. Blowes (2014), Diavik Waste Rock Project: Evolution of Mineral Weathering, Element Release, and Acid Generation and Neutralization during a Five-Year Humidity Cell Experiment, *Minerals*, *4*(2), 257–278, doi:10.3390/min4020257.

Lasagna, M., D. A. De Luca, and E. Franchino (2016), The role of physical and biological processes in aquifers and their importance on groundwater vulnerability to nitrate pollution, *Environ. Earth Sci.*, *75*(11), 961, doi:10.1007/s12665-016-5768-1.

Liao, L., C. T. Green, B. A. Bekins, and J. K. Böhlke (2012), Factors controlling nitrate fluxes in groundwater in agricultural areas, *Water Resour. Res.*, *48*, W00L09, doi:10.1029/2011WR011008.

Loschko, M., T. Wöhling, D. L. Rudolph, and O. A. Cirpka (2016), Cumulative relative reactivity: A concept for modeling aquifer-scale reactive transport, *Water Resour. Res.*, *52*(10), 8117–8137, doi:10.1002/2016WR019080.

LUBW (2011), Landesanstalt für Umwelt, Messungen und Naturschutz Baden-Württemberg, , 23. Available from: http://www4.lubw.baden-wuerttemberg.de/servlet/is/219325/grundwasserueberwachung_ergebnisse_2011.pdf?command=downloadContent&filename=grundwasserueberwachung_ergebnisse_2011.pdf (Accessed 15 April 2017)

MacQuarrie, K. T. B., and K. U. Mayer (2005), Reactive transport modeling in fractured rock: A state-of-the-science review, *Earth-Science Rev.*, *72*(3), 189–227, doi:10.1016/j.earscirev.2005.07.003.

MacQuarrie, K. T. B., K. U. Mayer, B. Jin, and S. M. Spiessl (2010), The importance of conceptual models in the reactive transport simulation of oxygen ingress in sparsely fractured crystalline rock, *J. Contam. Hydrol.*, *112*(1), 64–76, doi:10.1016/j.jconhyd.2009.10.007.

Mahmoudzadeh, B., L. Liu, L. Moreno, and I. Neretnieks (2013), Solute transport in fractured rocks with stagnant water zone and rock matrix composed of different geological layers-Model development and simulations, *Water Resour. Res.*, *49*(3), 1709–1727, doi:10.1002/wrcr.20132.

Mahmoudzadeh, B., L. Liu, L. Moreno, and I. Neretnieks (2016), Solute transport through fractured rock: Radial diffusion into the rock matrix with several geological layers for an arbitrary length decay chain, *J. Hydrol.*, *536*, 133–146, doi:10.1016/j.jhydrol.2016.02.046.

Maier, U., and C. M. Bürger (2013), An accurate method for transient particle tracking, *Water Resour. Res.*, *49*(5), 3059–3063, doi:10.1002/wrcr.20236.

Maier, U., H. Rügner, and P. Grathwohl (2007), Gradients controlling natural attenuation of ammonium, *Appl. Geochemistry*, *22*(12), 2606–2617, doi:10.1016/j.apgeochem.2007.06.009.

Maier, U., M. Flegr, H. Rügner, and P. Grathwohl (2013), Long-term solute transport and geochemical equilibria in seepage water and groundwater in a catchment cross section, *Environ. Earth Sci.*, *69*(2), 429–441, doi:10.1007/s12665-013-2393-0.

Maria, R. (2018), Comparative studies of groundwater vulnerability assessment, *IOP Conf. Ser. Earth Environ. Sci.*, *118*(1), 12018.

Mayer, K. U. (2002), Multicomponent reactive transport modeling in variably saturated porous media using a generalized formulation for kinetically controlled reactions, *Water Resour. Res.*, *38*(9), doi:10.1029/2001WR000862.

Michalzik, B., K. Kalbitz, J.-H. Park, S. Solinger, and E. Matzner (n.d.), Fluxes and concentrations of dissolved organic carbon and nitrogen – a synthesis for temperate forests, *Biogeochemistry*, *52*(2), 173–205, doi:10.1023/A:1006441620810.

Molson, J., M. Aubertin, and B. Bussière (2012), Reactive transport modelling of acid mine drainage within discretely fractured porous media: Plume evolution from a surface source zone, *Environ. Model. Softw.*, *38*, 259–270, doi:10.1016/J.ENVSOFT.2012.06.010.

Moore, T. R., D. Paré, and R. Boutin (2008), Production of Dissolved Organic Carbon in Canadian Forest Soils, *Ecosystems*, *11*(5), 740–751, doi:10.1007/s10021-008-9156-x.

Mualem, Y. (1976), A new model for predicting the hydraulic conductivity of unsaturated porous media, *Water Resour. Res.*, *12*(3), 513–522, doi:10.1029/WR012i003p00513.

Muniruzzaman, M., and M. Rolle (2016), Modeling multicomponent ionic transport in groundwater with IPhreeqc coupling: Electrostatic interactions and geochemical reactions in homogeneous and heterogeneous domains, *Adv. Water Resour.*, *98*, 1–15, doi:10.1016/J.ADVWATRES.2016.10.013.

Neretnieks, I. (1980), Diffusion in the rock matrix: An important factor in radionuclide retardation?, *J. Geophys. Res. Solid Earth*, *85*(B8), 4379–4397, doi:10.1029/JB085iB08p04379.

Neuman, S. P. (2005), Trends, prospects and challenges in quantifying flow and transport through fractured rocks, *Hydrogeol. J.*, *13*(1), 124–147, doi:10.1007/s10040-004-0397-2.

Oosterwoud, M. R., E. J. M. Temminghoff, and S. E. A. T. M. van der Zee (2010), Quantification of DOC concentrations in relation with soil properties of soils in tundra and taiga of Northern European Russia, *Biogeosciences Discuss.*, *7*(3), 3189–3226, doi:10.5194/bgd-7-3189-2010.

Opazo, T., R. Aravena, and B. Parker (2016), Nitrate distribution and potential attenuation mechanisms of a municipal water supply bedrock aquifer, *Appl. Geochemistry*, *73*, 157–168, doi:10.1016/j.apgeochem.2016.08.010.

Ortoleva, P., G. Auchmuty, J. Chadam, J. Hettmer, E. Merino, C. H. Moore, and E. Ripley (1986), Redox front propagation and banding modalities, *Phys. D Nonlinear Phenom.*, *19*(3), 334–354, doi:10.1016/0167-2789(86)90063-1.

Pauwels, H., V. Ayraud-Vergnaud, L. Aquilina, and J. Molénat (2010), The fate of nitrogen and sulfur in hard-rock aquifers as shown by sulfate-isotope tracing, *Appl. Geochemistry*, *25*(1), 105–115, doi:10.1016/J.APGEOCHEM.2009.11.001.

Pollock, D. W. (1988), Semianalytical Computation of Path Lines for Finite-Difference Models, *Ground Water*, *26*(6), 743–750, doi:10.1111/j.1745-6584.1988.tb00425.x.

Prommer, H., D. a. Barry, and G. B. Davis (2002), Modelling of physical and reactive processes during biodegradation of a hydrocarbon plume under transient groundwater flow conditions, *J. Contam. Hydrol.*, *59*(1-2), 113–131, doi:10.1016/S0169-7722(02)00078-5.

Prommer, H., D. A. Barry, and C. Zheng (2003), MODFLOW/MT3DMS-Based Reactive Multicomponent Transport Modeling, *Ground Water*, *41*(2), 247–257, doi:10.1111/j.1745-6584.2003.tb02588.x.

Puckett, L. J., A. J. Tesoriero, and N. M. Dubrovsky (2011), Nitrogen contamination of surficial aquifers--a growing legacy., *Environ. Sci. Technol.*, *45*(3), 839–44, doi:10.1021/es1038358.

Refsgaard, J. C. et al. (2014), Nitrate reduction in geologically heterogeneous catchments - A framework for assessing the scale of predictive capability of hydrological models, *Sci. Total Environ.*, *468-469*, 1278–1288, doi:10.1016/j.scitotenv.2013.07.042.

Richard T. Amos, *,†, † K. Ulrich Mayer, ‡ and David W. Blowes, and §. Carol J. Ptacek‡ (2004), Reactive Transport Modeling of Column Experiments for the Remediation of Acid Mine Drainage, , doi:10.1021/ES0349608.

Rivett, M. O., S. R. Buss, P. Morgan, J. W. N. Smith, and C. D. Bemment (2008), Nitrate attenuation in groundwater: A review of biogeochemical controlling processes, , doi:10.1016/j.watres.2008.07.020.

Robert A. Berner, R. A. (1981), A New Geochemical Classification of Sedimentary Environments, *SEPM J. Sediment. Res.*, *Vol. 51*(2), 359–365, doi:10.1306/212F7C7F-2B24-11D7-8648000102C1865D.

Rolle, M., G. Chiogna, D. L. Hochstetler, and P. K. Kitanidis (2013), On the importance of diffusion and compound-specific mixing for groundwater transport: An investigation from pore to field scale, *J. Contam. Hydrol.*, *153*, 51–68, doi:10.1016/j.jconhyd.2013.07.006.

Rügner, H., S. Kleineidam, and P. Grathwohl (1999), Long Term Sorption Kinetics of Phenanthrene in Aquifer Materials, , doi:10.1021/ES980664X.

Sanchez-León, E., C. Leven, C. P. Haslauer, and O. A. Cirpka (2016), Combining 3D Hydraulic Tomography with Tracer Tests for Improved Transport Characterization, *Groundwater*, *54*(4), 498–507, doi:10.1111/gwat.12381.

Schollenberger, U. (1998), *Beschaffenheit und Dynamik des Kiesgrundwassers im Neckartal bei T{ü}bingen*, C], Institut und Museum f{ü}r Geologie und Pal{ä}ontologie der Universit{ä}t T{ü}bingen.

Schwartz, F. W. (Franklin W. ., and H. Zhang (2003), *Fundamentals of ground water*, Wiley.

Selle, B., K. Rink, and O. Kolditz (2013), Recharge and discharge controls on groundwater travel times and flow paths to production wells for the Ammer catchment in southwestern Germany, *Environ. Earth Sci.*, *69*(2), 443–452, doi:10.1007/s12665-013-2333-z.

Shahkarami, P., L. Liu, L. Moreno, and I. Neretnieks (2015), Radionuclide migration through fractured rock for arbitrary-length decay chain: Analytical solution and global sensitivity analysis, *J. Hydrol.*, *520*, 448–460, doi:10.1016/j.jhydrol.2014.10.060.

Shestakov, V., A. Kuvaev, A. Lekhov, S. Pozdniakov, A. Rybalchenko, A. Zubkov, P. Davis, and E. Kalinina (2002), Flow and transport modeling of liquid radioactive waste injection using data from the Siberian Chemical Plant Injection Site, *Environ. Geol.*, *42*(2-3), 214–221, doi:10.1007/s00254-001-0491-x.

Sidborn, M. (2007), *Modelling long-term redox processes and oxygen scavenging in fractured crystalline rocks*, Kemiteknik, Kungliga Tekniska högskolan.

Sidborn, M., and I. Neretnieks (2007), Long term redox evolution in granitic rocks: Modelling the redox front propagation in the rock matrix, *Appl. Geochemistry*, *22*(11), 2381–2396, doi:10.1016/j.apgeochem.2007.05.007.

Sidborn, M., and I. Neretnieks (2008), Long-term oxygen depletion from infiltrating groundwaters: Model development and application to intra-glaciation and glaciation conditions, *J. Contam. Hydrol.*, *100*(1-2), 72–89, doi:10.1016/j.jconhyd.2008.05.010.

Singhal, B. B. S., and R. P. Gupta (2010), *Applied Hydrogeology of Fractured Rocks*, 2nd ed., Springer Netherlands, Dordrecht.

Spiessl, S. M., K. T. B. MacQuarrie, and K. U. Mayer (2008), Identification of key parameters controlling dissolved oxygen migration and attenuation in fractured crystalline rocks, *J. Contam. Hydrol.*, *95*(3), 141–153, doi:10.1016/j.jconhyd.2007.09.002.

Steefel, C. I., and A. C. Lasaga (1994), A coupled model for transport of multiple chemical species and kinetic precipitation/dissolution reactions with application to reactive flow in single phase hydrothermal systems, *Am. J. Sci.*, *294*(5), 529–592, doi:10.2475/ajs.294.5.529.

Steefel, C. I., and K. T. B. MacQuarrie (1996), Approaches to modeling of reactive transport in porous media, *Rev. Mineral. Geochemistry*, *34*(1), 85–129.

Steefel, C. I., D. J. DePaolo, and P. C. Lichtner (2005), Reactive transport modeling: An essential tool and a new research approach for the Earth sciences, *Earth Planet. Sci. Lett.*, *240*(3-4), 539–558, doi:10.1016/J.EPSL.2005.09.017.

Steefel, C. I. et al. (2015), Reactive transport codes for subsurface environmental simulation, *Comput. Geosci.*, *19*(3), 445–478, doi:10.1007/s10596-014-9443-x.

Stumm, W., and J. J. Morgan (1996), *Aquatic chemistry : chemical equilibria and rates in natural waters*, Wiley.

Sudicky, E. A., and E. O. Frind (1982), Contaminant transport in fractured porous media: Analytical solutions for a system of parallel fractures, *Water Resour. Res.*, *18*(6), 1634–1642, doi:10.1029/WR018i006p01634.

Sudicky, E. A., and E. O. Frind (1984), Contaminant Transport in Fractured Porous Media: Analytical Solution for a Two-Member Decay Chain in a Single Fracture, *Water Resour. Res.*, *20*(7), 1021–1029, doi:10.1029/WR020i007p01021.

Tang, D. H., E. O. Frind, and E. A. Sudicky (1981), Contaminant transport in fractured porous media: Analytical solution for a single fracture, *Water Resour. Res.*, *17*(3), 555–564, doi:10.1029/WR017i003p00555.

Tesoriero, A. J., and L. J. Puckett (2011a), O 2 reduction and denitrification rates in shallow aquifers, *Water Resour. Res.*, *47*(12), 1–17, doi:10.1029/2011WR010471.

Tesoriero, A. J., and L. J. Puckett (2011b), O 2 reduction and denitrification rates in shallow aquifers, *Water Resour. Res.*, *47*(12), n/a–n/a, doi:10.1029/2011WR010471.

Trinchero, P., I. Puigdomenech, J. Molinero, H. Ebrahimi, B. Gylling, U. Svensson, D. Bosbach, and G. Deissmann (2017), Continuum-based DFN-consistent numerical framework for the simulation of oxygen infiltration into fractured crystalline rocks, *J. Contam. Hydrol.*, *200*, 60–69, doi:10.1016/J.JCONHYD.2017.04.001.

US EPA, O. (n.d.), Contaminant Transport in Fractured Media: Models for Decision Makers,

Venterink, H. O., E. Hummelink, and M. W. Van Den Hoorn (2003), Denitrification potential of a river floodplain during flooding with nitrate-rich water: grasslands versus reedbeds, *Biogeochemistry*, *65*(2), 233–244, doi:10.1023/A:1026098007360.

Vías, J. M., B. Andreo, M. J. Perles, F. Carrasco, I. Vadillo, and P. Jiménez (2006), Proposed method for groundwater vulnerability mapping in carbonate (karstic) aquifers: the COP method, *Hydrogeol. J.*, *14*(6), 912–925, doi:10.1007/s10040-006-0023-6.

Vidal-Gavilan, G., A. Folch, N. Otero, A. M. Solanas, and A. Soler (2013), Isotope characterization of an in situ biodenitrification pilot-test in a fractured aquifer, *Appl. Geochemistry*, *32*, 153–163, doi:10.1016/J.APGEOCHEM.2012.10.033.

Villinger, E. (1982), Grundwasserbilanzen im Karstaquifer des Oberen Muschelkalks im Oberen Gau (Baden Wu¨rtemberg), *Geol. Jahrb., C 32*, 43–61.

Welch, H. L., C. T. Green, and R. H. Coupe (2011), The fate and transport of nitrate in shallow groundwater in northwestern Mississippi, USA, *Hydrogeol. J.*, *19*(6), 1239–1252, doi:10.1007/s10040-011-0748-8.

West, M. R., B. H. Kueper, and K. S. Novakowski (2004), Semi-analytical solutions for solute transport in fractured porous media using a strip source of finite width, *Adv. Water Resour.*, *27*(11), 1045–1059, doi:10.1016/J.ADVWATRES.2004.08.011.

Williamson, M. A., and J. D. Rimstidt (1994), The kinetics and electrochemical rate-determining step of aqueous pyrite oxidation, *Geochim. Cosmochim. Acta*, *58*(24), 5443–5454, doi:10.1016/0016-7037(94)90241-0.

WJ.W. Ball, and D. Kirk Nordstrom (1991), *User's manual for WATEQ4F, with revised thermodynamic data base and text cases for calculating speciation of major, trace, and redox elements in natural waters*, Washington DC.

Wösten, J. H. M., and M. T. van Genuchten (1988), Using Texture and Other Soil Properties to Predict the Unsaturated Soil Hydraulic Functions, *Soil Sci. Soc. Am. J.*, *52*(6), 1762, doi:10.2136/sssaj1988.03615995005200060045x.

Wunderly, M. D., D. W. Blowes, E. O. Frind, and C. J. Ptacek (1996), Sulfide mineral oxidation and subsequent reactive transport of oxidation products in mine tailings impoundments: A numerical model, *Water Resour. Res.*, *32*(10), 3173–3187, doi:10.1029/96WR02105.

Zhang, F. et al. (2012), *Ground Water Reactive Transport Model.*, Bentham Science Publishers.

Zhang, Y. C., H. Prommer, H. P. Broers, C. P. Slomp, J. Greskowiak, B. Van Der Grift, and P. Van Cappellen (2013), Model-based integration and analysis of biogeochemical and isotopic dynamics in a nitrate-polluted pyritic aquifer, *Environ. Sci. Technol.*, *47*(18), 10415–10422, doi:10.1021/es4023909.

Zhu, Y., H. Zhan, and M. Jin (2016), Analytical solutions of solute transport in a fracture–matrix system with different reaction rates for fracture and matrix, *J. Hydrol.*, *539*, 447–456, doi:10.1016/j.jhydrol.2016.05.056.

APPENDIX I. SEM IMAGES OF UPPER MUSCHELKALK LIMESTONE MATRIX AND X-RAY SPECTROSCOPY OF SELECTED MINERALS

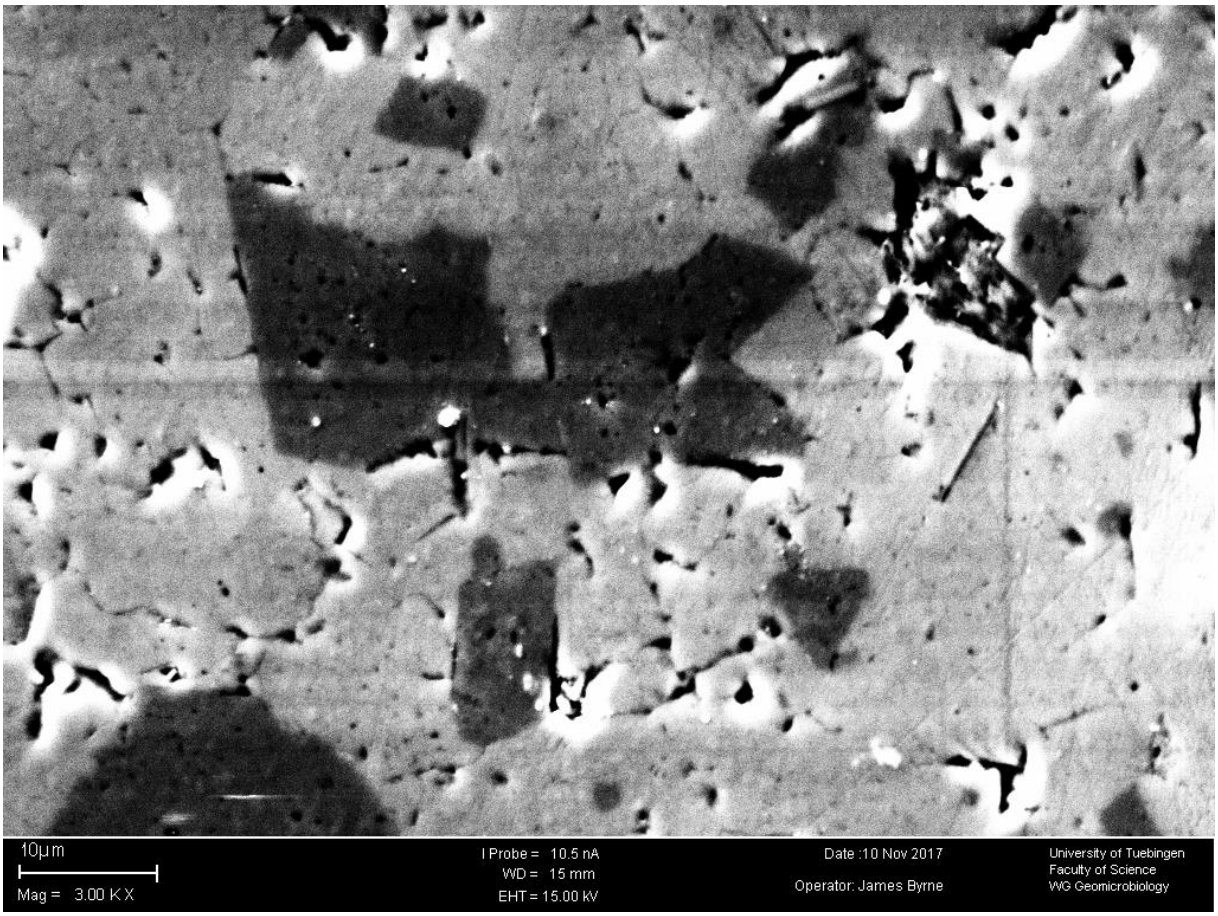

Fig. A2.1. SEM image of the Upper Muschelkalk limestone, sample 1.

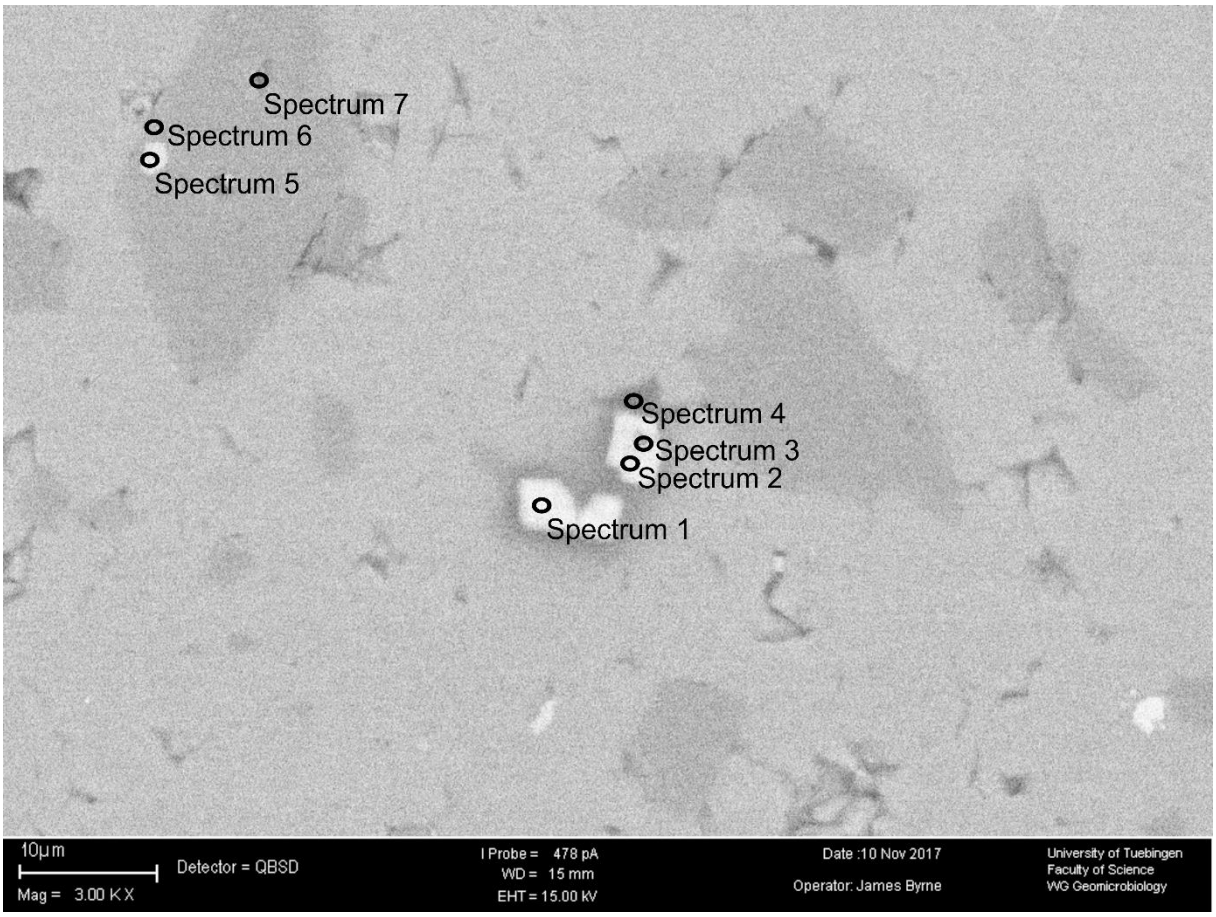
Spectrum 7
Spectrum 6
Spectrum 5
Spectrum 4
Spectrum 3
Spectrum 2
Spectrum 1
10µm
Mag = 3.00 K X
Detector = QBSD
I Probe = 478 pA
WD = 15 mm
EHT = 15.00 kV
Date :10 Nov 2017
Operator: James Byrne
University of Tuebingen
Faculty of Science
WG Geomicrobiology

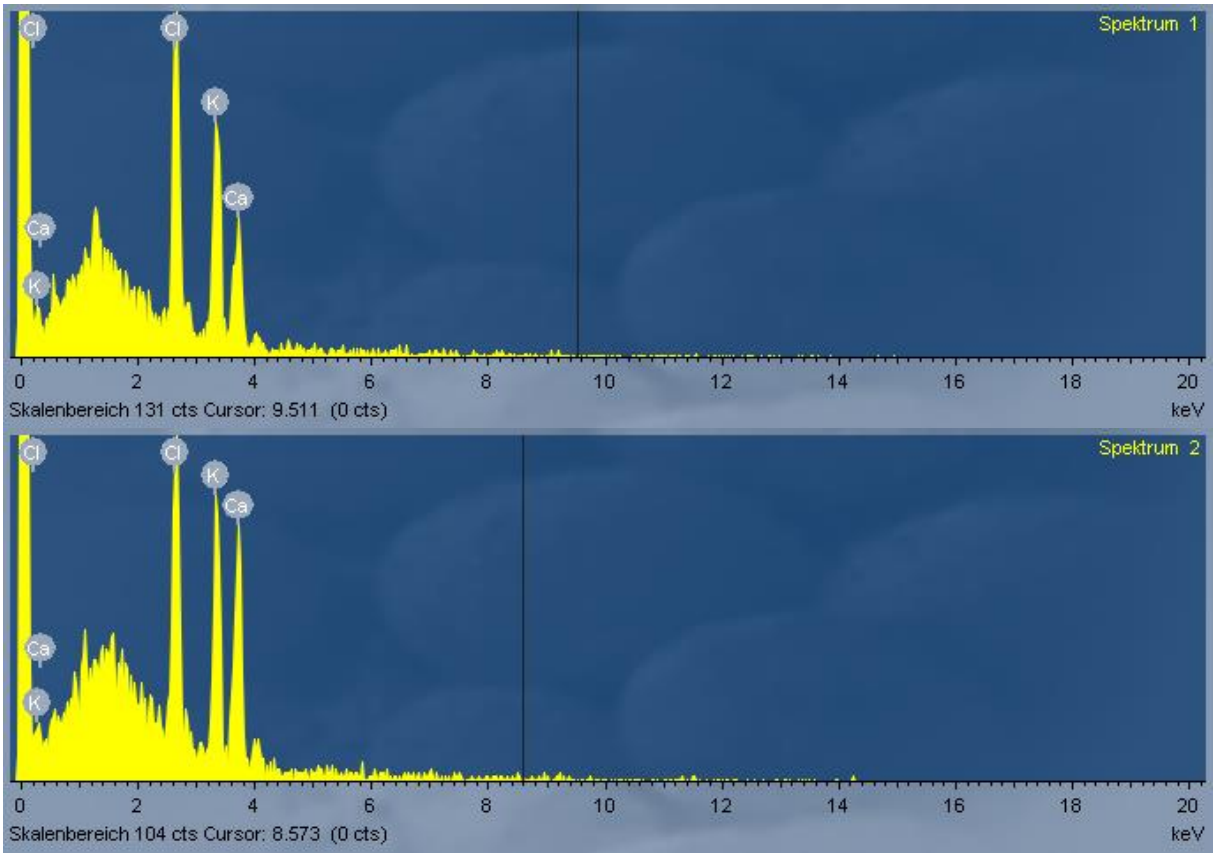
Spektrum 1
Cl
Cl
K
Ca
Ca
K
0 2 4 6 8 10 12 14 16 18 20
Skalenbereich 131 cts Cursor: 9.511 (0 cts)
keV
Spektrum 2
Cl
Cl
K
Ca
Ca
K
0 2 4 6 8 10 12 14 16 18 20
Skalenbereich 104 cts Cursor: 8.573 (0 cts)
keV

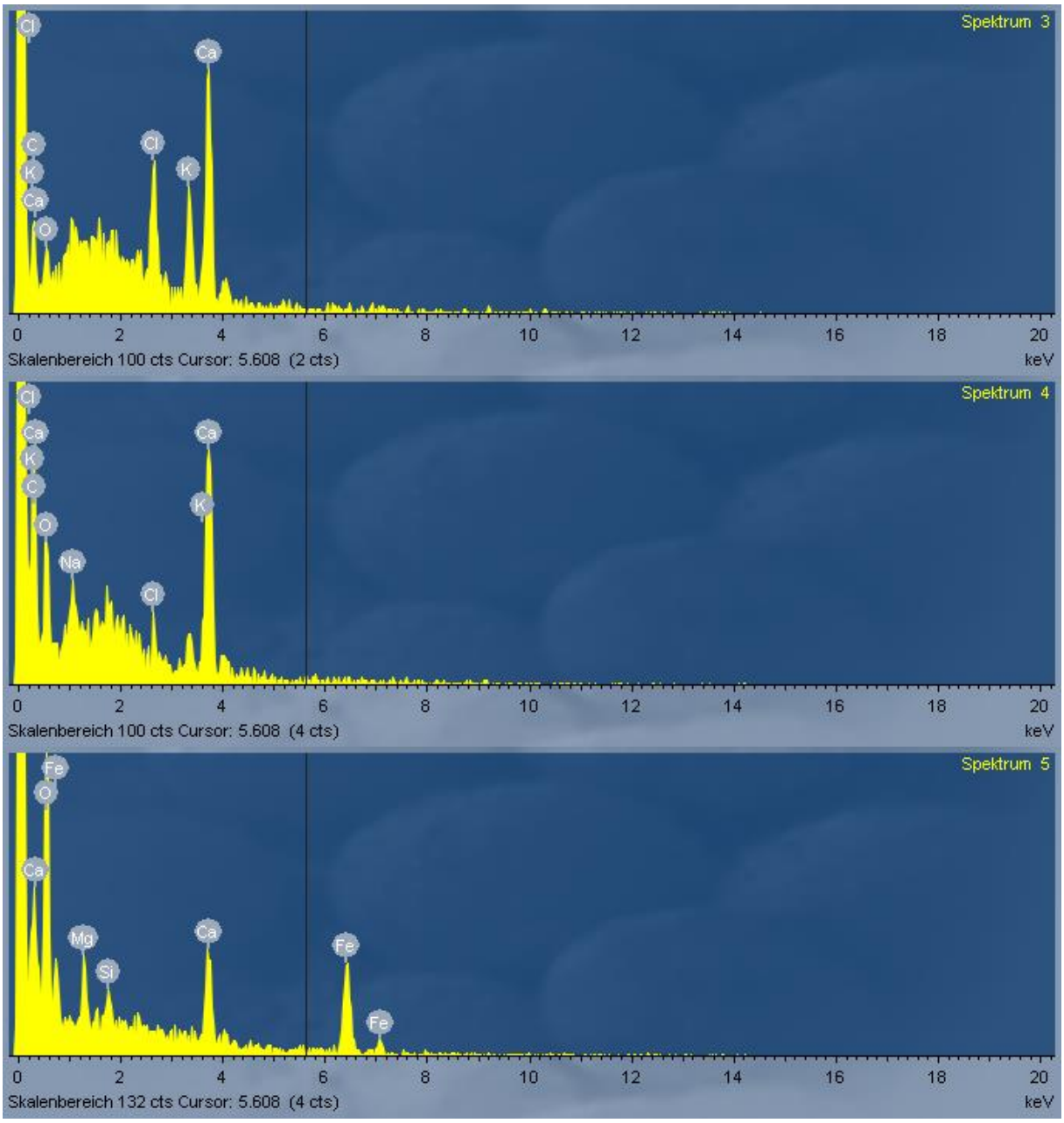
Spektrum 3
Cl
Ca
C
Cl
K
K
Ca
O
0 2 4 6 8 10 12 14 16 18 20
Skalenbereich 100 cts Cursor: 5.608 (2 cts)
keV
Spektrum 4
Cl
Ca
Ca
K
C
K
O
Na
Cl
0 2 4 6 8 10 12 14 16 18 20
Skalenbereich 100 cts Cursor: 5.608 (4 cts)
keV
Spektrum 5
Fe
O
Ca
Mg
Ca
Fe
Si
Fe
0 2 4 6 8 10 12 14 16 18 20
Skalenbereich 132 cts Cursor: 5.608 (4 cts)
keV

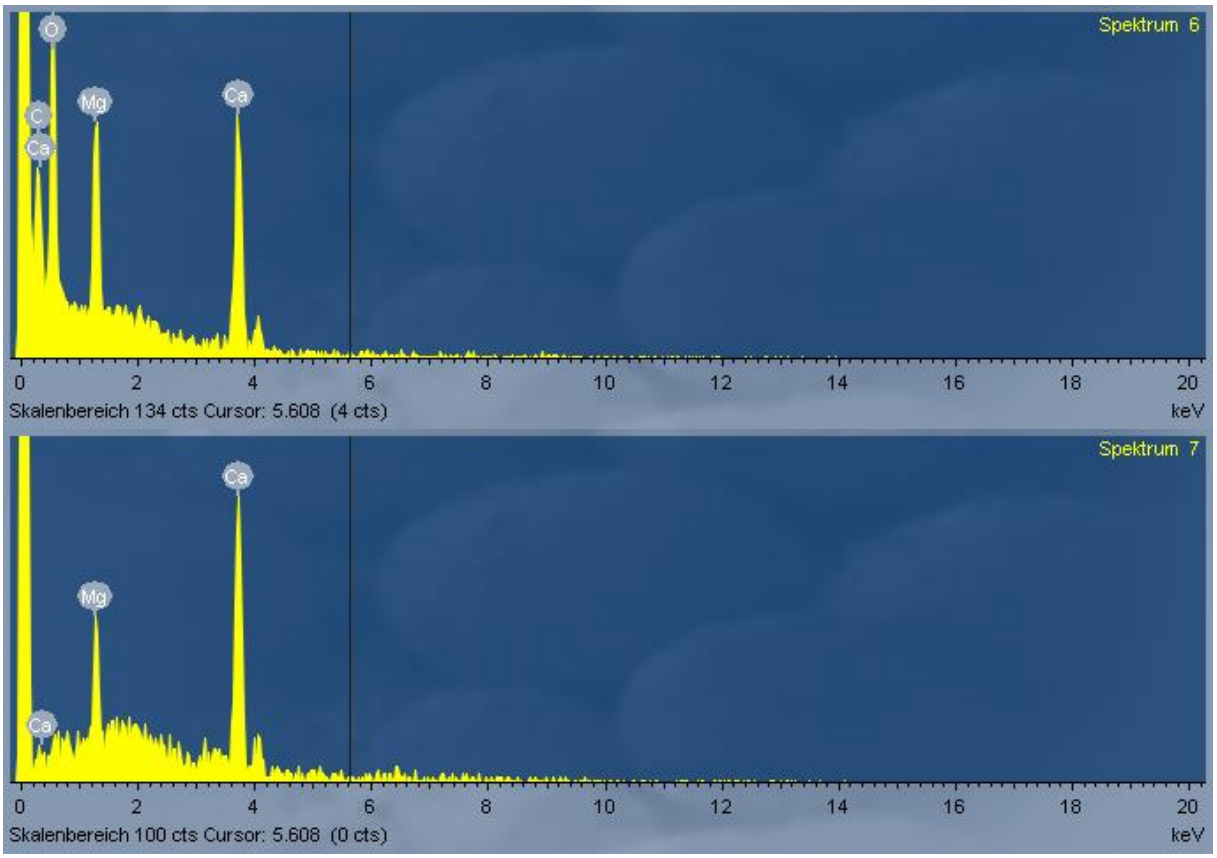

Fig. A2.2. SEM image of the Upper Muschelkalk limestone(top) and X-RAY spectrums(bottom), sample 2.

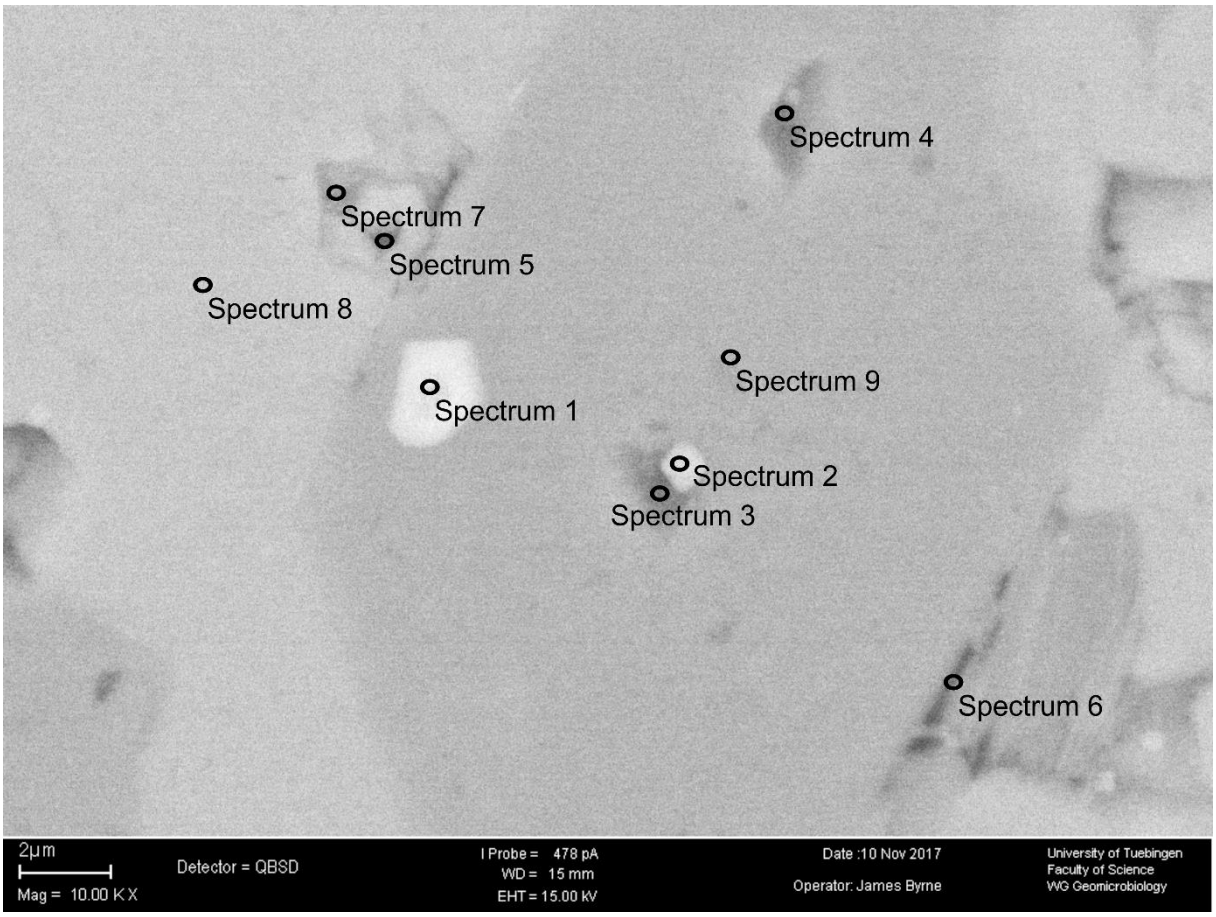
Spectrum 4
Spectrum 7
Spectrum 5
Spectrum 8
Spectrum 9
Spectrum 1
Spectrum 2
Spectrum 3
Spectrum 6
2µm
Mag = 10.00 K X
Detector = QBSD
I Probe = 478 pA
WD = 15 mm
EHT = 15.00 kV
Date :10 Nov 2017
Operator: James Byrne
University of Tuebingen
Faculty of Science
WG Geomicrobiology

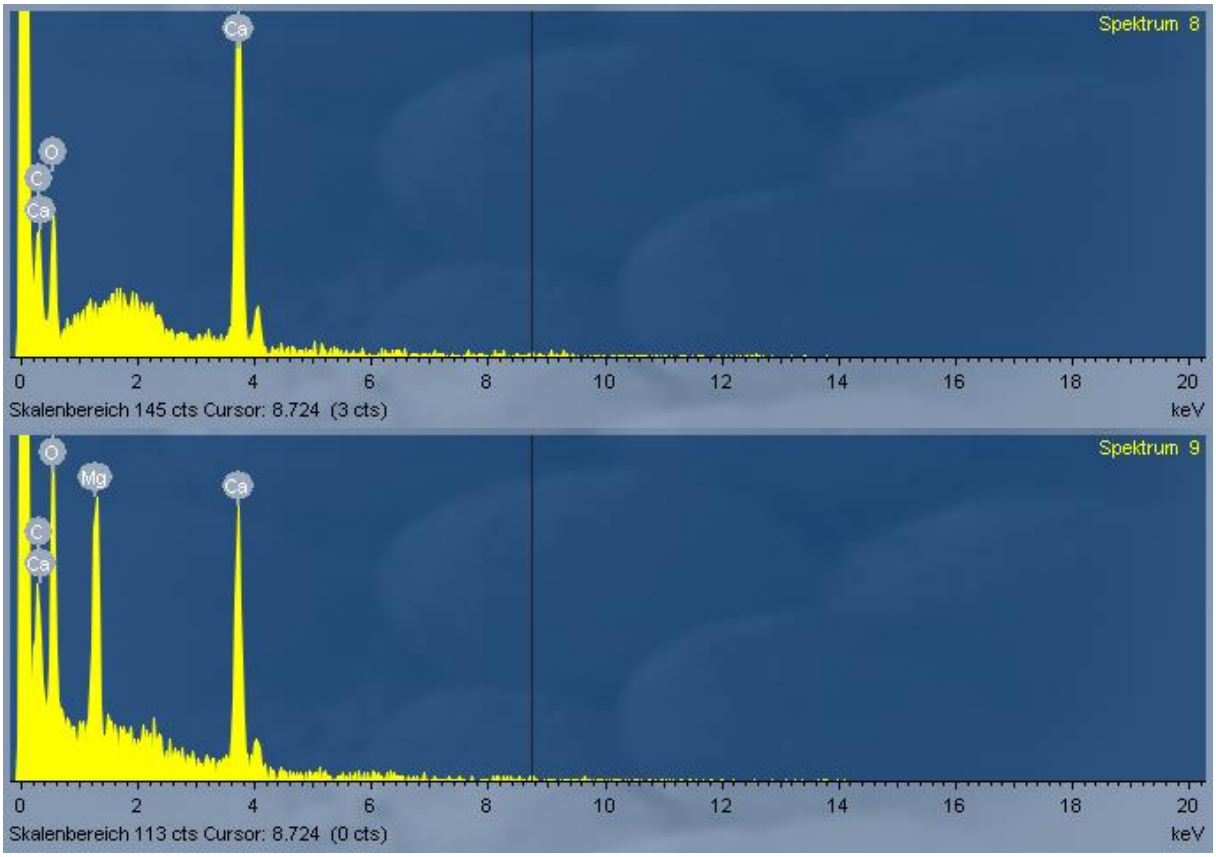
Spektrum 8
O
C
Ca
Ca
0 2 4 6 8 10 12 14 16 18 20
Skalenbereich 145 cts Cursor: 8.724 (3 cts)
keV
Spektrum 9
O
Mg
Ca
C
Ca
0 2 4 6 8 10 12 14 16 18 20
Skalenbereich 113 cts Cursor: 8.724 (0 cts)
keV

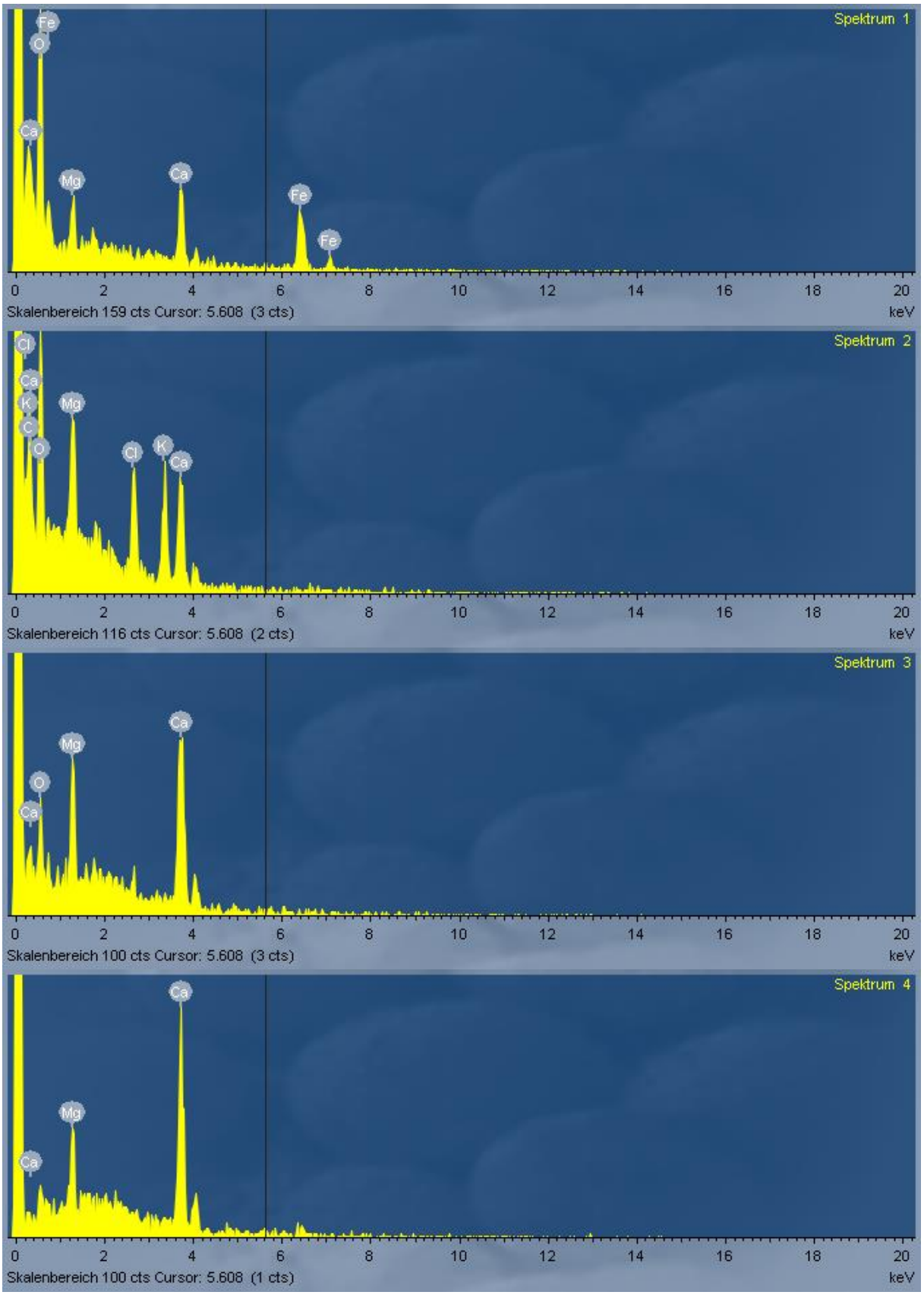
Spektrum 1
Fe
O
Ca
Mg
Ca
Fe
Fe
0 2 4 6 8 10 12 14 16 18 20
Skalenbereich 159 cts Cursor: 5.608 (3 cts)
keV
Spektrum 2
Cl
Ca
K
Mg
C
O
Cl
K
Ca
0 2 4 6 8 10 12 14 16 18 20
Skalenbereich 116 cts Cursor: 5.608 (2 cts)
keV
Spektrum 3
Ca
Mg
O
Ca
0 2 4 6 8 10 12 14 16 18 20
Skalenbereich 100 cts Cursor: 5.608 (3 cts)
keV
Spektrum 4
Ca
Mg
Ca
0 2 4 6 8 10 12 14 16 18 20
Skalenbereich 100 cts Cursor: 5.608 (1 cts)
keV

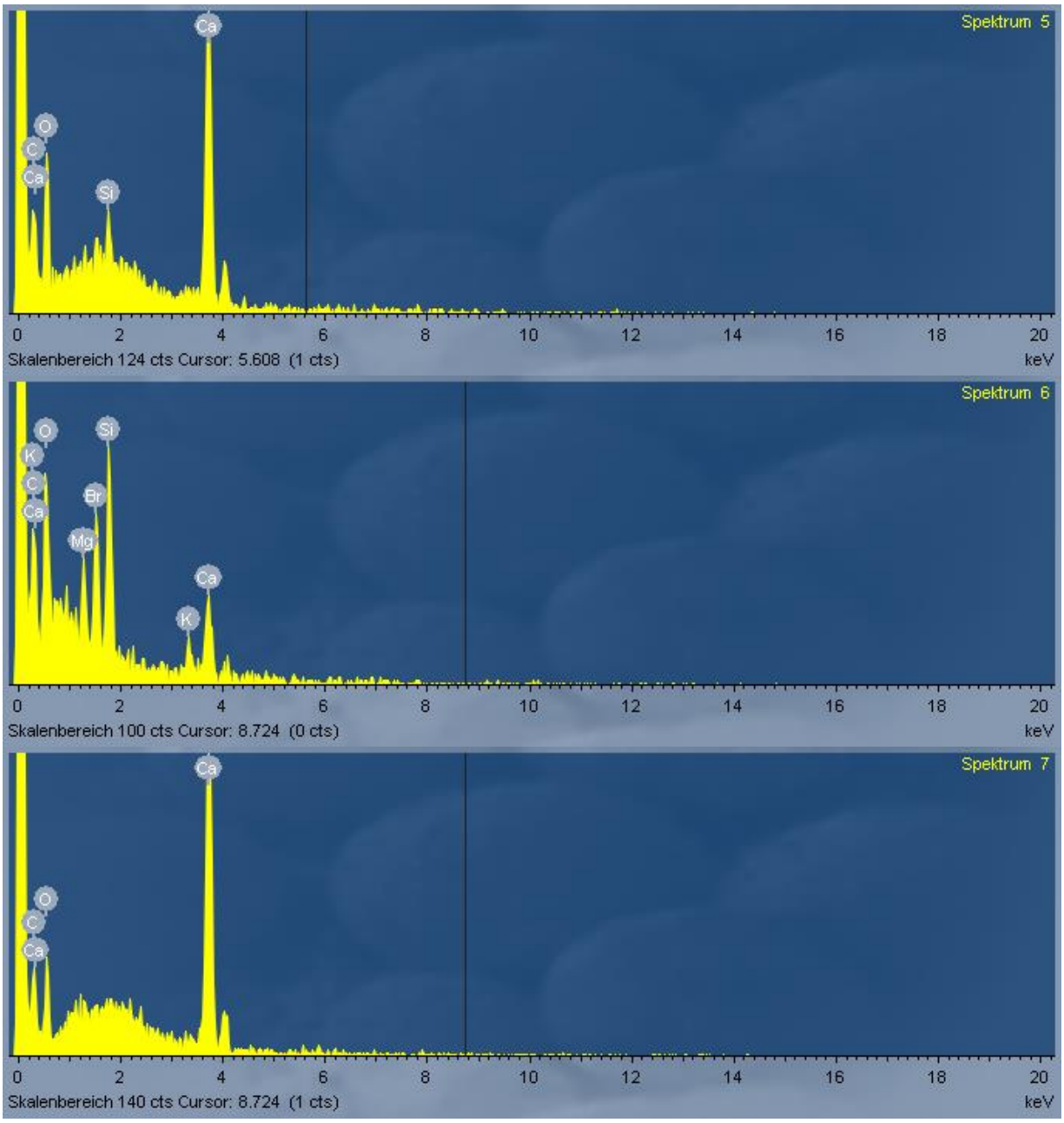

Fig. A2.3. SEM image of the Upper Muschelkalk limestone(top) and X-RAY spectrums(bottom), sample 3.

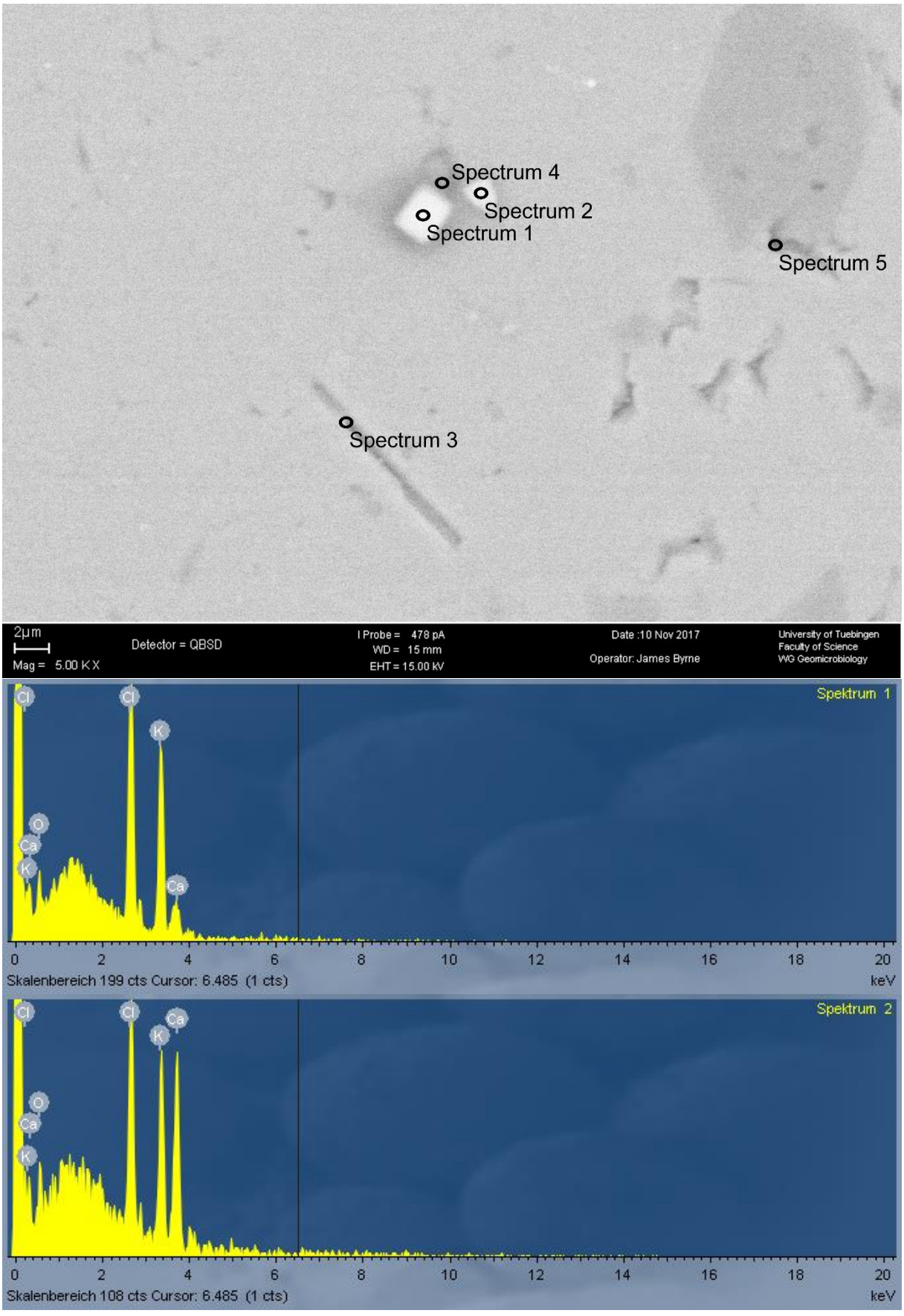
Spectrum 4
Spectrum 2
Spectrum 1
Spectrum 5
Spectrum 3
2µm
Mag = 5.00 K X
Detector = QBSD
I Probe = 478 pA
WD = 15 mm
EHT = 15.00 kV
Date :10 Nov 2017
Operator: James Byrne
University of Tuebingen
Faculty of Science
WG Geomicrobiology
Spektrum 1
Cl
Cl
K
O
Ca
K
Ca
0 2 4 6 8 10 12 14 16 18 20
Skalenbereich 199 cts Cursor: 6.485 (1 cts)
keV
Spektrum 2
Cl
Cl
Ca
K
O
Ca
K
0 2 4 6 8 10 12 14 16 18 20
Skalenbereich 108 cts Cursor: 6.485 (1 cts)
keV

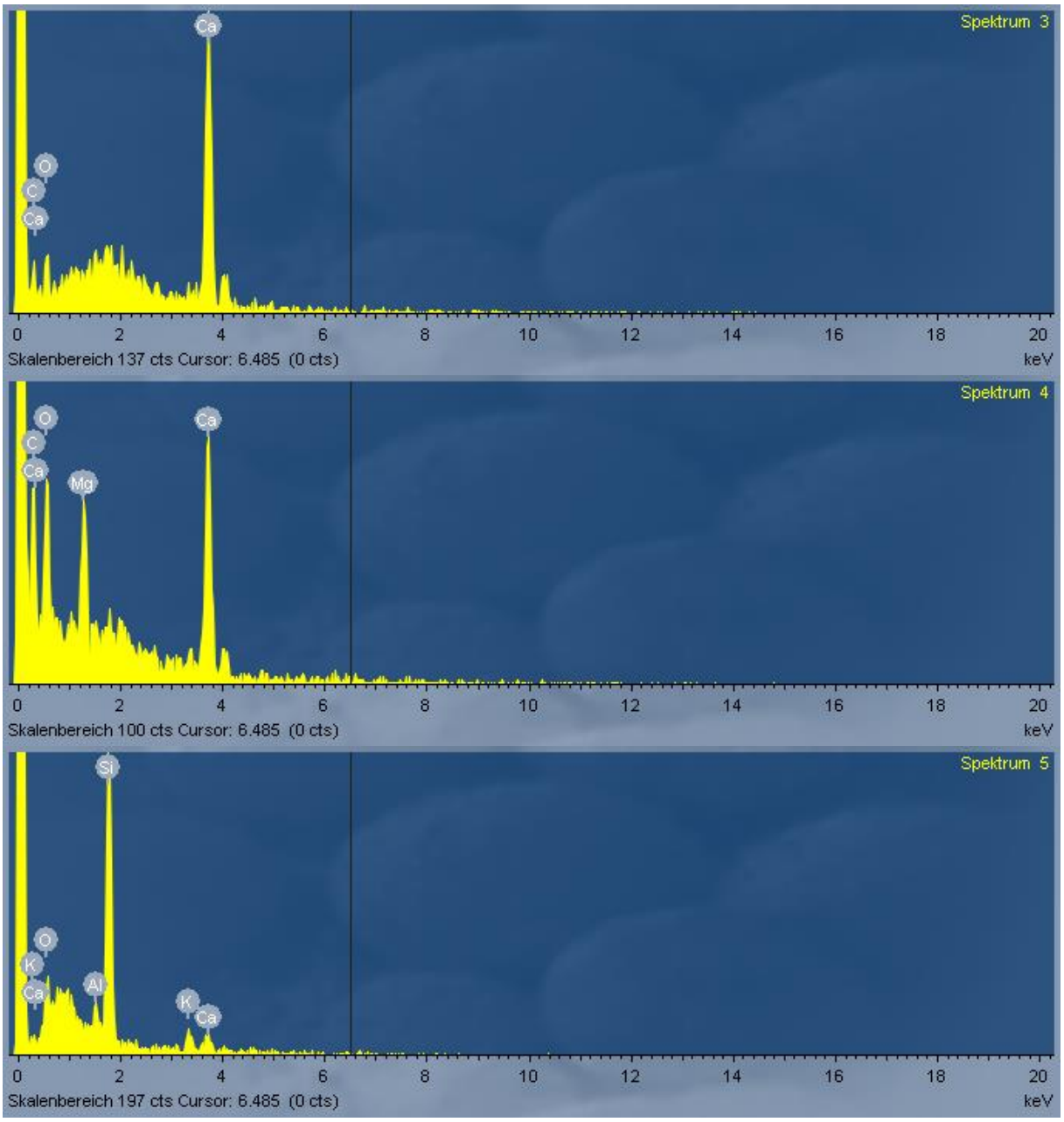

Fig. A2.4. SEM image of the Upper Muschelkalk limestone(top) and X-RAY spectrums(bottom), sample 4

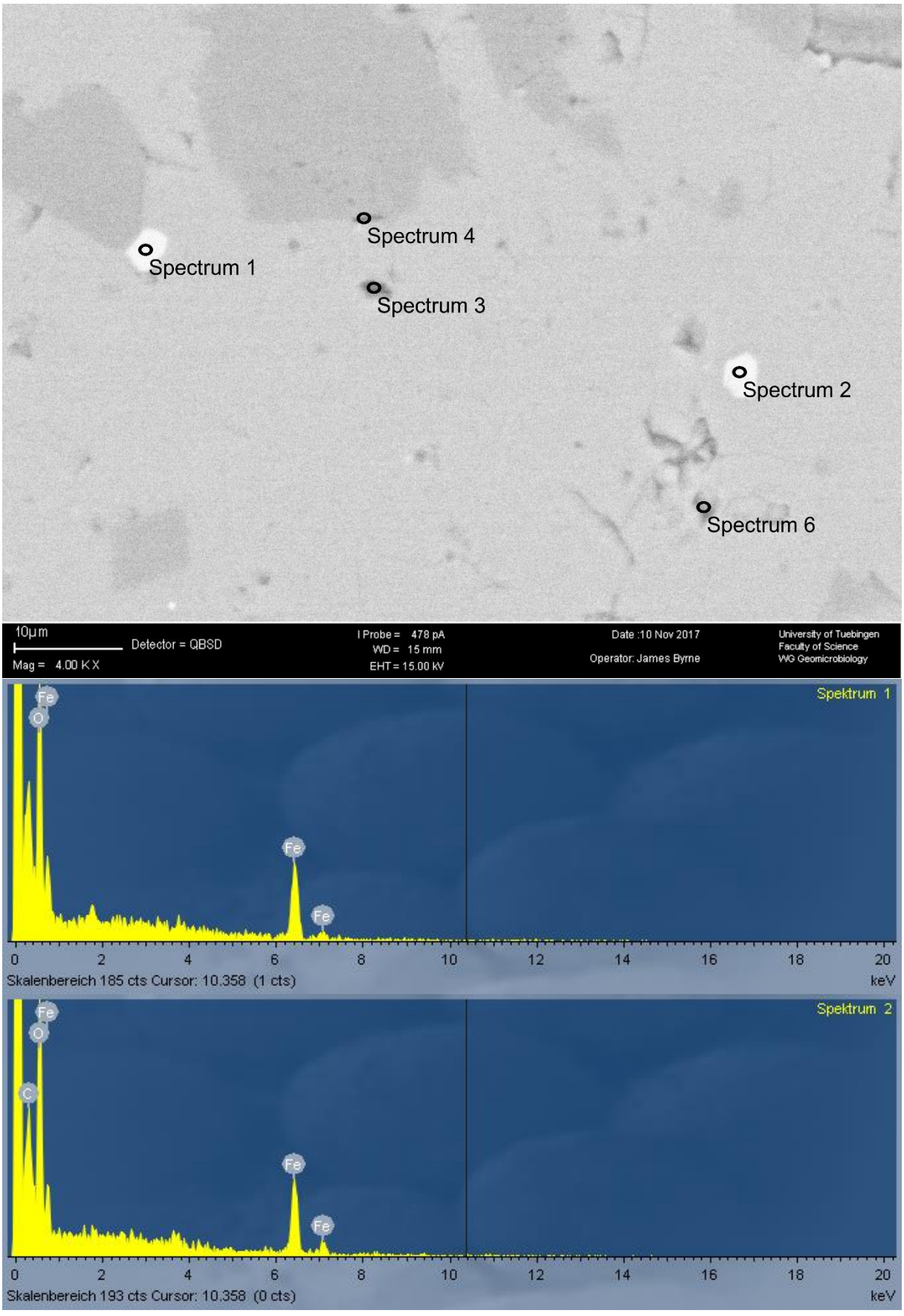
Spectrum 1
Spectrum 4
Spectrum 3
Spectrum 2
Spectrum 6
10µm
Detector = QBSD
Mag = 4.00 K X
I Probe = 478 pA
WD = 15 mm
EHT = 15.00 kV
Date :10 Nov 2017
Operator: James Byrne
University of Tuebingen
Faculty of Science
WG Geomicrobiology
Spektrum 1
Fe
O
Fe
Fe
0 2 4 6 8 10 12 14 16 18 20
Skalenbereich 185 cts Cursor: 10.358 (1 cts)
keV
Spektrum 2
Fe
O
C
Fe
Fe
0 2 4 6 8 10 12 14 16 18 20
Skalenbereich 193 cts Cursor: 10.358 (0 cts)
keV

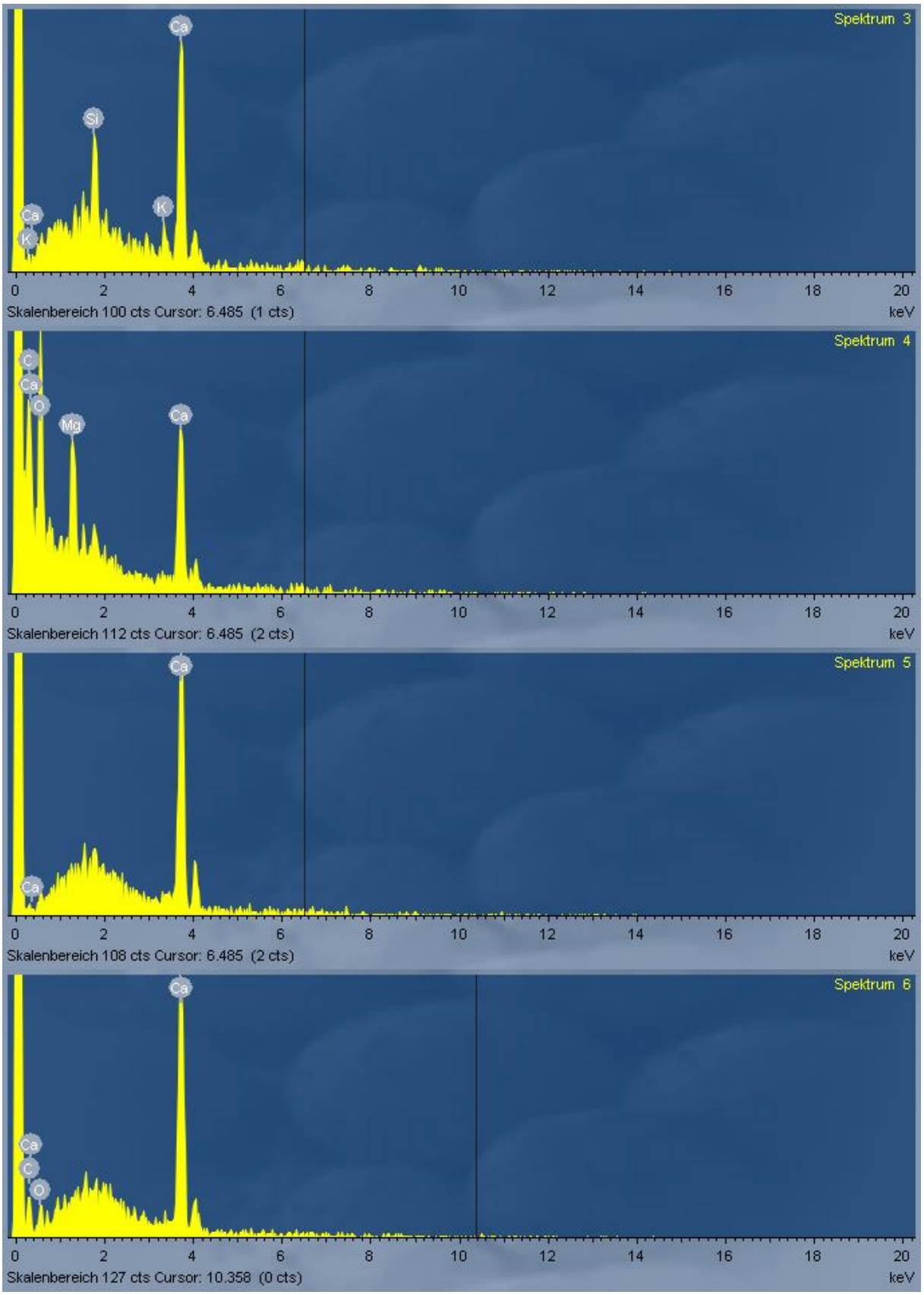

Fig. A2.5. SEM image of the Upper Muschelkalk limestone(top) and X-RAY spectrums(bottom), sample 5.

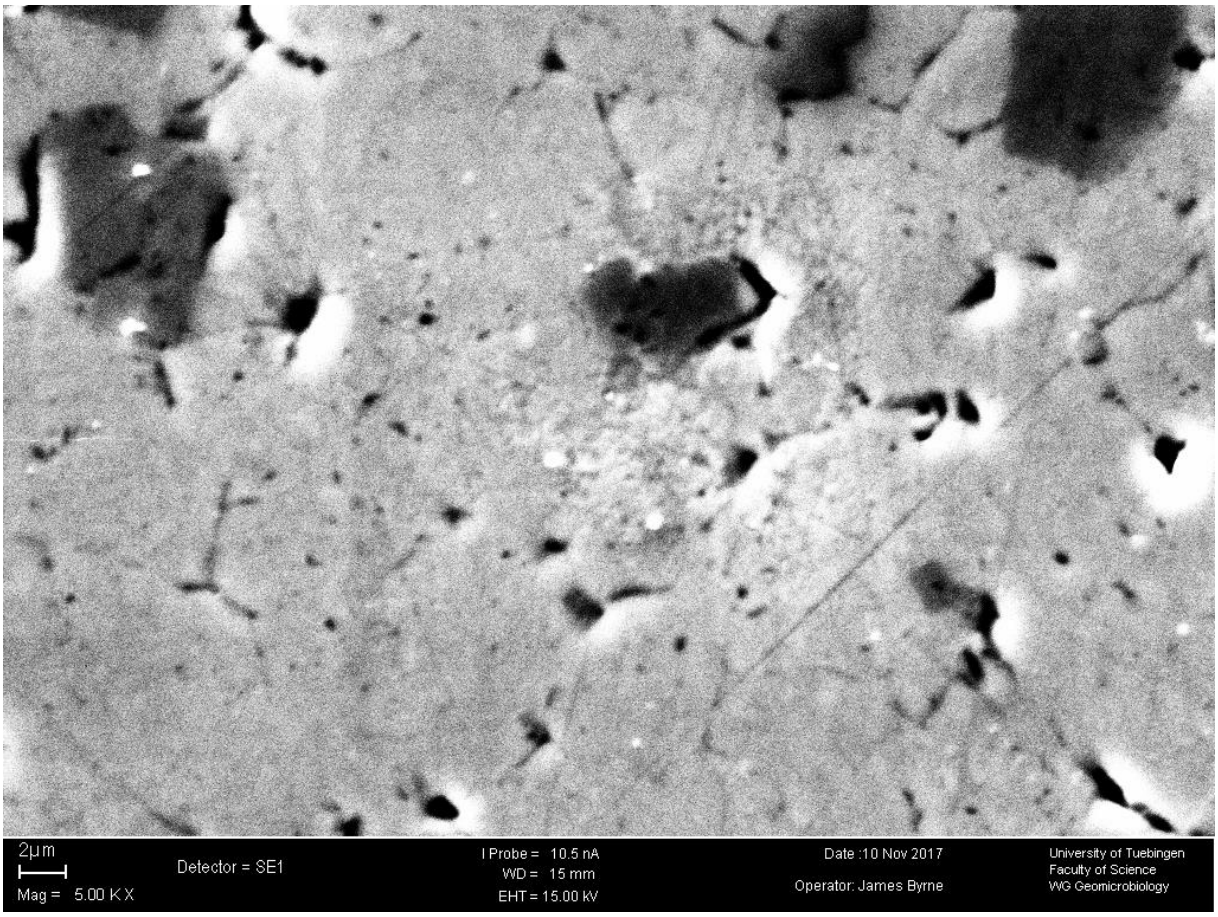

Fig. A2.6. SEM image of the Upper Muschelkalk limestone, sample 6.